POLITECNICO DI MILANO
Corso di Laurea Magistrale in Ingegneria Nucleare
Scuola di Ingegneria Industriale e dell'Informazione

Compact photon sources in multi-PetaWatt facilities: a kinetic numerical investigation

Supervisor: Prof. Matteo Passoni
Tutor: PhD Mickael Grech
Advisor: Eng. Arianna Formenti

Dissertation of:
Rafael Caprani
Student ID 897348

Academic Year 2019-2020

"Life's like a river that you can't see too far ahead,
you don't know where it will bend and turn.
There is only one thing you can know and control: yourself.
Once you know yourself, then wherever the river takes you,
you'll be right where you were always meant to be."

Abstract

The first PetaWatt laser facilities are becoming operational, and are expected to deliver *on-target* intensities exceeding $10^{22}\mathrm{Wcm}^{-2}$, making new regimes of laser-matter interaction experimentally available for the first time. Ultra-intense laser-plasma interaction can lead to a broad spectrum of physical effects among which synchrotron-like photon emission. This work aims to reach a better understanding of the physics and properties of the radiation emission in ultra-intense laser-plasma interaction. The goal of this thesis is to gain insights on the system behaviour, helping designing experiments never possible before.

An extensive, kinetic, multidimensional Particle-In-Cell simulation campaign has been employed. A laser pulse with specifics realistic of the forthcoming Apollon facility in Paris-Saclay, is used to impact on a multilayered target made of a low-density layer, and a solid density substrate. Special attention is given to the modelling, where a balance between physically realistic and computationally affordable configuration has been used.

Carefully designing the simulation set-up we managed to observe copious high energy photon production, with energy conversion efficiency from laser to synchrotron radiation of the order of 10^{-1}.

Sommario

Le prime installazioni di laser multi-PetaWatt stanno venendo ultimate. L'aspettativa è di poter irraggiare target con intensità superiori a $10^{22}\mathrm{Wcm}^{-2}$, riuscendo così a rendere accessibili per la prima volta i regimi ultra-intensi dell'interazione laser-plasma. Quest'ultima può portare ad una vasta varietà di fenomeni fisici, tra cui l'emissione di radiazione di sincrotrone.

L'obiettivo di questa tesi è quello di raggiungere una migliore comprensione della fisica e delle proprietà dell'emissione di radiazione nell'interazione laser-plasma ultra-intensa, fornendo così strumenti utili alla progettazione di esperimenti mai stati possibili fino ad ora. A questo scopo è stato effettuato un vasto studio di simulazioni numeriche multidimensionali con il codice Particle-In-Cell Smilei.

Un impulso laser, le cui specifiche sono state basate sulle reali condizioni nominali del laser Apollon (presto ultimato nel sito di Parigi-Saclay), è stato irraggiato su di un target multistrato composto da uno strato a bassa densità e uno a densità solida. Dando particolare attenzione alla modellazione numerica, è stata raggiunta una configurazione risultante dal compromesso tra l'aderenza alla realtà sperimentale e l'economia delle risorse computazionali.

Progettando opportunamente i set-up delle simulazioni, è stato possibile osservare una copiosa produzione di fotoni ad alte energie, con efficienza complessiva di conversione energetica da laser a radiazione dell'ordine di 10^{-1}.

Estratto

L'invenzione della tecnologia laser ha rivoluzionato il mondo scientifico, rendendo possibile lo sviluppo di numerose applicazioni sia in ambito di ricerca, sia in ambito industriale.

Grazie allo sviluppo della tecnica chiamata *Chirped Pulse Amplification* (CPA) avvenuta nel 1985, è stato possibile incrementare continuamente l'intensità degli impulsi laser. Le istallazione stato-dell'arte che verranno ultimate nei prossimi anni promettono di riuscire a irraggiare un bersaglio con decine di Joule in poche decine di femtosecondi su di una superficie di pochi micrometri quadrati. Questi sistemi raggiungerebbero così intensità superiori ai 10^{21}Wcm^{-2} con corrispondenti potenze dell'ordine del PetaWatt, prendendo il nome di *Ultra-High-Intensity Lasers* (UHI). L'attività di ricerca sull'interazione in questi regimi ha portato risultati molto promettenti nell'individuazione di schemi di vasto interesse applicativo. Questo lavoro si inserisce nella linea di ricerca dedicata all'utilizzo di tali schemi per la produzione di fotoni ad alta energia (chiamati anche fotoni-γ in seguito) tramite l'emissione di sincrotrone. La tesi qui presentata è frutto della collaborazione tra il Politecnico di Milano e l'École Polytechnique di Parigi, quest'ultimo, luogo in cui è stato svolto l'intero lavoro qui presentato.

Per ottenere radiazione di sincrotrone, è necessario ottenere elettroni ad alte energie (>MeV) immersi in potenti campi elettromagnetici. Tradizionalmente per produrre elettroni energetici (o "caldi"), un target solido viene irraggiato con un laser ad alta intensità, il quale trasferisce parte della sua energia agli elettroni i quali danno vita ad una vasta gamma di fenomeni, tra cui l'emissione di sincrotrone. Un bersaglio solido tradizionale è caratterizzato da una densità dell'ordine di centinaia o migliaia di volte la densità critica (n_c) di un tipico impulso laser ultra-intenso (i.e. basato su un sistema Titanio:Zaffiro). Questo fa si che l'impulso laser impattante venga principalmente riflesso dal bersaglio, e non assorbito, portando ad efficienze di assorbimento molto basse. Diverse strategie sono state pensate per aumentare la frazione di energia del laser assorbita dagli elettroni, ed aumentare quindi la loro energia cinetica, aumentando così l'energia irradiata. Ingegnerizzando opportunamente i materiali del bersaglio si possono progettare configurazioni avanzate di particolare interesse per questo lavoro. Tra questi i materiali nanostrutturati hanno suscitato particolare attenzione grazie alla loro bassissima densità media, di soli alcuni mg/cm^3, stesso ordine di grandezza della densità critica dell'impulso laser (spesso chiamati materiali "*near-critical*"). È stato dimostrato sia teoricamente sia sperimentalmente come l'interazione tra un bersaglio a densità dell'ordine di n_c e un laser superintenso sia caratterizzata da un migliore assorbimento elettronico dell'energia contenuta nell'impulso laser.

Tra tutti i possibili materiali nanostrutturati, alcuni (nanotubi di carbonio) sono stati studiati nell'ambito dell'ottimizzazione dell'emissione di sincrotrone, fornendo risultati promettenti. Questo lavoro si concentra sull'utilizzo di materiali detti *foams*

(in italiano *schiume*) che prima d'ora sono stati adoperati solo per schemi rivolti all'ottimizzazione dell'accelerazione di ioni. Questa tipologia di materiali è caratterizzata da una morfologia porosa e microscopicamnete irregolare. È importante sottolineare come i valori molto bassi di densità di questi materiali (dell'ordine della densità dell'aria) rendono molto complessa la loro fabbricazione, e numerosi sforzi sono stati volti negli ultimi anni alla produzione e caratterizzazione di *foam* con queste proprietà. Le tecniche di produzioni disponibili non sono molte ma comprendono metodi sia fisici che chimici, nell'ambito di questo lavoro faremo riferimento alle *foam* prodotte tramite *Pulsed Laser Deposition* (PLD). Questa tecnica accresce lo spessore del materiale depositando su di un substrato solido quantità sempre crescenti di nanoparticelle di dimensione caratteristica di decine di nm, le quali si auto-assemblano in strutture di scala maggiore ($\sim \mu$m). Questa tecnica da così origine a un bersaglio costituito da due strati, uno nanostrutturato e uno solido, in serie tra loro. Questa configurazione di target avanzati prende il nome di *target multistrato* o MLT (dall'inglese *Multi-Layered-Targets*).

Data l'elevata intensità della radiazione laser, i lavori teorico-numerici in letteratura fanno uso di due ipotesi semplificative del sistema. La prima è quella di assumere che la materia venga ionizzata "istantaneamente" dall'impulso laser, per cui di fatto il sistema può essere modellizato come un impulso laser interagente con bersaglio completamente ionizzato (plasma). La seconda è la considerazione che in tali regimi le interazioni a lungo raggio sia preponderanti rispetto a quelle a corto raggio, considerando quindi solo i fenomeni collettivi, trascurando così processi come quelli collisionali.
Gli studi teorico-numerici nella linea di ricerca in cui si colloca questo lavoro si basano generalmente sulla teoria cinetica dei plasmi. La risoluzione analitica dei sistemi che la caratterizzano è possibile solo per sistemi molto semplici e lontani dalla realtà sperimentale. Pertanto è fondamentale ricorrere a strumenti numerici, in particolare i codici *Particle-In-Cell* (PIC) si sono rivelati essere i più adatti, nonchè i più utilizzati in letteratura per la simulazione di plasmi cinetici.

L'obiettivo di questo lavoro consiste in un'indagine numerica sulla produzione di fotoni ad alte energie mediante l'emissione di sincrotrone nell'interazione tra un bersaglio a bassa densità (*near-critical*) e un impulso laser ultraintenso (UHI). Lo scopo ultimo è quello di fornire indicazioni sul design di esperimenti possibili per la prima volta nel prossimo futuro. Abbiamo svolto una vasta indagine parametrica usando lo strumento delle simulazioni numeriche PIC 2D per lo studio di fenomeni caratteristici dei sistemi di interesse. Per favorire una maggiore adesione alla realtà sperimentale e per meglio comprendere gli effetti dovuti esclusivamente alla nanostruttura, particolare attenzione è stata data alla modellizzazione del materiale bersaglio. Prima di tutto abbiamo cercato di ricreare risultati già ottenuti da altri gruppi di ricerca, validando così sia la modellizzazione del sistema, sia i diversi codici utilizzati (*Smilei* e *piccante*). Una *foam* reale, e quindi intrinsecamente tridimensionale, si struttura seguendo complessi processi di aggregazione che le conferiscono caratteristiche specifiche, impossibili da imitare per intero in un sistema bidimensionale. L'unica modellizzazione 2D in grado di avvicinarsi alle proprietà di una *foam* tridimensionale è una collezione di "nanosfere" bidimensionali disposte casualmente nel volume del bersaglio. Questa configurazione è stata recentemente testata in letteratura portando a risultati soddisfacenti, nei limiti della dimensionalità del sistema.

Successivamente abbiamo indagato alcuni effetti della propagazione nel materiale bersaglio sull'impulso laser, con particolare interesse verso il fenomeno del *self-focusing* e della riflessione causata dall'interazione con il substrato solido. Grazie alla combinazione di questi due effetti, che insieme contribuiscono a concentrare l'energia trasportata dal laser, abbiamo osservato un incremento dell'intensità di picco dell'impulso anche di un ordine di grandezza rispetto all'intensità di incidenza. Infine abbiamo caratterizzato la copiosa emissione di fotoni di questi sistemi di interesse, analizzato le proprietà macroscopiche e microscopiche della radiazione emessa. Dai risultati emerge chiaramente la complessità del sistema, per esempio l'andamento dell'efficienza di conversione in radiazione (frazione di energia del laser convertita in fotoni-γ) ha dimostrato un andamento tutt'altro che banale. Anche l'analisi dello spettro energetico e della distribuzione angolare dei fotoni emessi ha dato risultati dall'interpretazione complessa. In particolare è stato evidenziato come le configurazioni che garantivano valori più alti per l'efficienza di conversione in radiazione non necessariamente corrispondevano a configurazioni in grado di massimizzare l'energia degli stessi fotoni emessi. Sono stati comunque forniti strumenti per comparare le diverse configurazioni le une con le altre ed è stato sottolineato come la "miglior configurazione" dipenda dalla grandezza che più si vuole massimizzare. Per evidenziare l'effetto dovuto esclusivamente alla struttura, ogni bersaglio nanostrutturato è stato confrontato con un sistema omogeneo caratterizzato dalla stessa densità media n_0. In generale i bersagli omogenei hanno performato meglio di quelli nanostrutturati, evidenziando come nei regimi di interesse le disomogeneità, anche se in scale spaziali inferiori alla lunghezza d'onda del laser, portano fattori di inefficienza nell'ambito dell'emissione di radiazione di sincrotrone.

I risultati ottenuti sono ritenuti molto interessanti soprattutto in considerazione al fatto che i regimi esplorati saranno sperimentalmente disponibili nel prossimo futuro.

Le simulazioni sono state svolte utilizzando il codice PIC *open-source* Smilei. A causa del loro elevato costo computazionale, ogni simulazione presentata in questo lavoro è stata effettuata presso il cluster *Irene Joliot Curie* presente al centro di calcolo *Très Grand Centre de Calcul* (TGCC) a Bruyéres-le-Châtel, Francia.

Contents

Introduction

The term *Radiation Sources* indicates any technology able to produce any sort of radiation(α, β, γ, X or ions). Radiations are used in a broad spectrum of fields among which medicine, material science and laboratory astrophysics. This work focuses on exploring the possibility to build a compact, tunable and reliable γ-photon source using a state of the art multi-PW laser *Apollon*.

With the name γ-rays we refer to the most energetic part of the electromagnetic spectrum. This kind of high energy radiation has lots of applications among which [1] :

- **Medical**:

  - Radiotherapy
  - Sterilization of surgical items (i.e. killing micro-organisms from surgical tools) and food (i.e. elimination of Salmonella from seafood)
  - Radiodiagnostic (i.e. bone density)

- **Industrial**:

  - Material non-destructive-testing (NDT) (i.e. material radiography, composite structure analysis)
  - Material testing in high dose fields (i.e. space oriented materials)
  - Art irradiation (i.e. reduces paintings decay)

- **Laboratory Astrophysics**:

  - Study of extreme astrophysical environments (i.e. supernovae)
  - electron-position pair production via inverse Compton scattering

$$\gamma + \hbar\omega \rightarrow e^- + e^+$$

Traditional γ sources are mainly of two kinds: isotope-based, or accelerator-based. In the first a radioactive isotope is used to directly irradiate the object of interest and measures of transmission or scattering can be done. This is also historically the first employment of radioactivity. Radionuclides can also be incorporated into compounds and used as an imaging tool inside a patient in medical facilities. Radioisotopes are constantly active and this can raise radioprection issues. Furthermore one cannot control the intensity of the source, decreasing exponentially in time. The second kind are based instead on the use of a particle accelerator, often a synchrotron. These machines produce high energy electron beams which can be bent using strong magnetic fields, emitting radiation. Synchrotrones can be switched on and off at will and therefore carry reduced radioprotection issues and their brilliance is relatively tuneable. On the other hand the cost and size of these machines is huge,

usually several hundreds of M€.

The possibility to employ a Laser-driven mechanism as a γ source results interesting in order to reduce costs while overcoming some limitations of traditional γ sources. This innovative approach is often referred to as *Compact radiation sources* or *Laser driven radiation sources*.

Using a laser to produce the necessary radiation would reduce of roughly one order of magnitude the cost of building and of few times the physical size with respect to a traditional synchrotron. This idea opened the path to the study of *Compact Radiation Sources* which is one of the most active topics in the plasma physics community. Such a device would be able to overcome some of the limitations of the traditional sources. The laser can be turned on and off at will just like synchrotrones, the emitted radiation would have tuneable properties (i.e. brilliance, cut-off energy, ...), all in an efficient and affordable technology. Only the most powerfull lasers can be usefull in this line of research, in particular for photon sources the intensity (power divided by surface area on which is delivered) required is thought to be $> 10^{22} \mathrm{Wcm}^{-2}$. These kind of facilities are callad *Multi-PetaWatt Lasers* and we will talk about them more at the very beginning of chapter 2.

In the forthcoming years will start the first experimental investigation of this topic and great is the need for numerical support. Complex systems behaviour is often difficult to predict analytically and thus, designing experiments exploiting new and unexplored regimes is no simple task. Being able to simulate numerically even complex systems is therefore a fundamental tool in order to gain insights on the processes at play, and to help scientists designing efficient and effective experiments. This thesis aims at being a preliminary numerical study giving insights on the properties of compact γ sources, serving as a cornerstone during the experimental design. This project is a collaboration between the ENSURE NANOLAB [2] at Politecnico di Milano, and the *Laboratoire d'Utilisation des Lasers Intenses* (LULI) at École Polytechnique in Paris. We used the kinetic, relativistic, and quantum *Particle-In-Cell* (PIC) code *Smilei* [3] in about 200 simulations for a total of about 1.5MCPUhours of computing time. The results of this work are very promising and further investigation is being scheduled starting from the collected data.

Part I

Theory and methods

Chapter 1

Photon emission and back reaction on the electron dynamics

The goal of this thesis is to explore the possiblity to enhance γ-photons emission using the Petawatt laser facility Apollon. This being said the total energy converted from laser (infrared) to photons is not the only relevant result, but also the energy of the resulting photons is crucial. For various applications (i.e. laboratory astrophysics) the higher the photon energy, the better. In the frame of this work we will use interchangeably the word "photons" or γs, eventhough a photon is more in general descriptive of a quantum of electromagnetic energy, while there is not an exact and universal definition of γ-rays. Many distinguish X-rays from γ-rays using the quality of the photon source: if the photon is produced by electrons is called "X", if is produced by nuclear transition is called "γ". We will not employ this definition here, although all photons created in this work come from electrons, because we are more interested in highlighting the high energy of the photons produced more than we are in their origin. We will use a energy-based definition of γ-rays instead. There is no universal threshold for photons to be considered γ-rays but a good rule of thumb is that the energy of the photon should be bigger than one tenth of the rest mass of the electron ($m_e/10 \approx 0.0511$ MeV),or over about 50 KeV. In this work we will try to obtain high energy conversion from laser to photons, but we will favour the systems for which the photons are more energetic. It is becoming pretty clear that the emission spectrum of the electrons should be taken into account, and is important to give an overview of the basic physics behind it.

In the frame of this work we will always talk about *synchrotron-like* radiation, neglecting all other effects (i.e. *Bremsstrahlung*) which are considered of minimal importance in the regimes explored here [4].

We therefore start by describing the physics behind the photon emission phenomenon. The basic ingredients, as we will see in more details, are energetic electrons and large electromagnetic (EM) fields. In this chapter we will discuss how the process of radiation is described once we already obtained a system with these two ingredients, regardless of how we reached them. The source of the high amplitude EM fields is the laser pulse, while the production of high energy electrons will be the topic of chapter 2.

One should also note that the aim of the following chapter is not to give an extensive and rigorous treaty of classical and quantum electrodynamics, which is beyond the purpouse of this thesis, but only to summarize the derivation of the main quantities of interest for this work. We will start by looking at the most intuitive physical picture, and then move to a classical description of the phenomena. Finally we will

summarize what a more quantum approach would tell us about the main quantities we are interested in. We will start by approaching the problem from a single particle perspective in sections 1.1 and 1.2, while in section 1.3 we will address the specific properties of the radiation emission of a many-particles system.

1.1 Classical radiation emission and back reaction

Before discussing the features of classical radiation emission, we need to formally define the Lorentz factor γ to which we will refer to several times during this work. Recalling Einstein famous equation for massive particles:

$$\epsilon_{tot} = mc^2 = \gamma m_0 c^2 = \epsilon_{rest} + \epsilon_{kin}, \tag{1.1}$$

with m_0 being the particle rest mass and γ:

$$\gamma = \sqrt{\frac{1}{1 - \frac{v^2}{c^2}}}, \tag{1.2}$$

where v denotes the particle velocity. We can then rearrange the equations to obtain a usefull expression for the kinetic energy:

$$\epsilon_{kin} = m_0 c^2 (\gamma - 1). \tag{1.3}$$

There goes also the fact that in ultra-relativistic regime ($\gamma \gg 1$) $\epsilon_{kin} \approx m_0 c^2 \gamma$. This will be useful to keep in mind since in literature and in the frame of this work, the energy parameter for ultra-relativistic electrons is usually γ_e and not directly their kinetic energy ϵ_{kin}^{eon}.

The energy of a photon can be expressed by the product of the reduced Planck constant and its wave angular frequency ω. We can define also a Lorentz factor for photons which is no more than the photon energy normalized by a reference energy. We take this reference energy to be the energy associated to the electron rest mass ($m_e c^2 \approx 0.511 \text{MeV}$). The photon Lorentz factor reads:

$$\gamma_\gamma = \frac{\epsilon^{photon}}{m_e c^2} = \frac{\hbar \omega}{m_e c^2} \tag{1.4}$$

1.1.1 Simple model for radiation by moving charged particles

Let's start by addressing the fact that because of the equivalence of inertial frames, any charged particle uniformly moving does not radiate, so only accelerated particles emit energy in the form of electomagnetic waves. We will now show a simple example of how this concept can be grasped then we will show only the result of a more rigouros derivation, while for the derivation itself we will refer to more appropriate texts such as [5][6][7].

Let's imagine a system (figures 1.1) with a positive charged particle in point A which is stationary at $t = 0$. This charged particle produces an electrostatic field which is visualized by the dashed lines. Let's now assume that the particle accelerates uniformly to $v = \Delta v$ in a short time Δt until it arrives in B and then moves uniformly,

the electrostatic field of the particle in B is represented with solid lines.

After an arbitrary time t after the particle has arrived in B, the information about the particle accelerating and arriving in B has travelled at the speed of light c reaching a radius $R = ct$. Now, for any point in space at a distance $r < R$ from B the particle is already in B and there is therefore a Coulomb field with lines centered in B. For any point in space at a distance $r > R + c\Delta t$ the particle is still in A and so the field is a Coulomb field with lines centered in A. Because of the continuity of the electromagnetic field, it is required that a transverse field is propagating at velocity c. This would mean that an accelerating particle has produced an electromagnetic wave propagating away from it, and since EM waves transport energy, we can conclude that the particle has radiated energy away in the form of an EM wave. Looking at figure 1.1 it is possibile to compute the ratio of the components of the field in the shaded region:

$$\frac{E_\perp}{E_\parallel} = \frac{t\Delta v \sin\theta}{c\Delta t} = \frac{ta \sin\theta}{c}. \tag{1.5}$$

In which we defined a to satisfy $\Delta v = a\Delta t$. The parallel component is just the electrostatic Coulomb field given by $E_\parallel = q/(4\pi\epsilon_0 R^2)$. We can then compute the perpendicular component as:

$$E_\perp = \frac{qa \sin\theta}{4\pi\epsilon_0 c^2 R}. \tag{1.6}$$

And, remebering the definition of the Poynting vector and the relation between electric and magnetic field in an electromagnetic wave:

$$\boldsymbol{S} = \frac{\boldsymbol{E} \times \boldsymbol{B}}{\mu_0}, \tag{1.7}$$

$$S = \frac{q^2 a^2 \sin^2\theta}{16\pi\epsilon_0 c^3 R^2}. \tag{1.8}$$

Once we have the poynting vector we can compute its flux through the spherical surface of radius R in order to get the total radiated power P_{cl} (as in "classical"):

$$P_{cl} = \frac{q^2 a^2}{6\pi\epsilon_0 c^3}. \tag{1.9}$$

1.1.2 Synchrotron emission

Considering now the ultra-relativistic limit ($\gamma \gg 1$), we can assume that all the radiation is emitted in the direction of motion of the particle and can be treated like *synchrotron* radiation [4] [6].

It should be remarked that eq.(1.9) is the Larmor Power in the non-relativistic limit. It can be generalized to an arbitrary velocity and applied in particular to the case of a particle accelerated in an electromagnetic field [7][8]:

$$P_{cl} = P_0 \eta^2 \text{ with } P_0 = \frac{2mc^2}{3\tau_e}. \tag{1.10}$$

The quantity $\tau_e = r_e/c$ is the time needed for the light to travel the classical electron radius $r_e = q^2/(4\pi\epsilon_0 mc^2) \approx 2.82 \times 10^{-15}$m .

The parameter η can be thought as the amplitude of the field in the particle proper
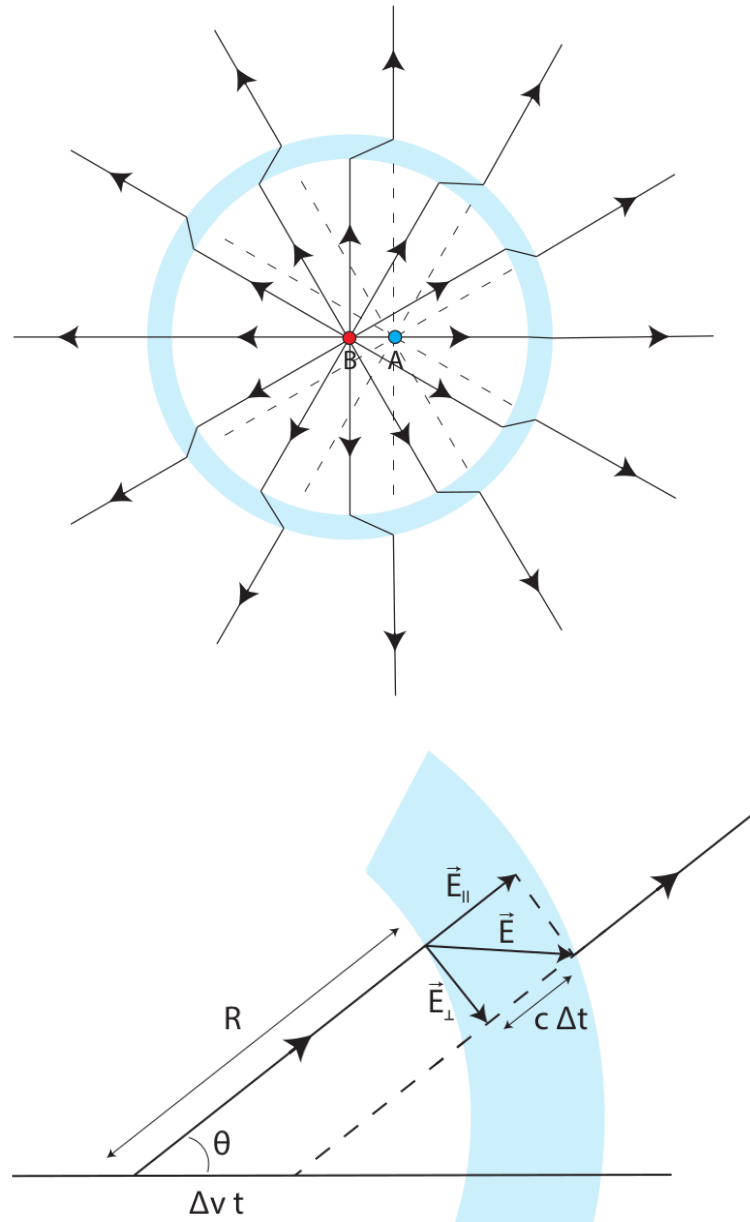
Figure 1.1: Drawing of a particle in point A at $t = 0$ with $v = 0$, the same particle in B at $t = \Delta t$ with $v = \Delta v$, and the generated fields (top). Close-up of the blue region and decomposition of the electric field in its parallel and perpendicular components (bottom). From [7]

frame nomralized to a specific reference field. For the purpose of this section η in the particle proper frame is defined as:

$$\eta \equiv \left| \frac{F^{\mu\nu} p_\nu}{E_s m_e} \right|, \tag{1.11}$$

in which $F^{\mu\nu}$ is the elctromagnetic tensor defined as:

$$F^{\mu\nu} = \begin{bmatrix} 0 & -E_x/c & -E_y/c & -E_z/c \\ E_x/c & 0 & B_z & -B_y \\ E_y/c & -B_z & 0 & B_x \\ E_z/c & B_y & -B_x & 0 \end{bmatrix}, \tag{1.12}$$

with the four-momentum:

$$p = \begin{bmatrix} \gamma mc, & p_x, & p_y, & p_z \end{bmatrix}, \tag{1.13}$$

and E_{cr}:

$$E_{cr} \equiv \frac{4\pi\epsilon_0 m^2 c^4}{e^3}. \tag{1.14}$$

E_{cr} is called "critical field of classical electrodynamics" and its value is about $\approx 1.8 \times 10^{20} \text{V/m}$. The parameter η is also related to the "quantum parameter" χ that we will discuss in section 1.2.1.
We can rewrite η more simply in the following form:

$$\eta = \frac{\gamma}{E_{cr}} \left| -(\boldsymbol{\beta} \cdot \boldsymbol{E})^2 + (\boldsymbol{E} + \boldsymbol{v} \times \boldsymbol{B})^2 \right|^{1/2} \tag{1.15}$$

I would like to point the attention of the reader towards the fact that if all the quantities are expanded properly $P_{cl} \propto mass^{-3}$ meaning that a proton which has $m_p \approx 1836 m_e$ seeing the same field from its proper frame would emit a radiated classical power $\approx (1836)^3$ smaller than an electron. This fact leads us to consider only electrons (or positrons) when talking about radiation emitted by moving charged particles[1]. Whenever we use the subscript "e" we specifically refer to an electronic quantity (i.e. m_e is the rest mass of the electron), while if no subscript is used we are referring to a general particle. Beware that since we will always find only electrons radiating, the two notations are often interchangeable.
The classical instantaneous power emission spectrum, often called *Synchrotron spectrum*, can be computed as shown in chapter 14 of [6] and reads:

$$\frac{dP_{inst}}{d\gamma_\gamma} = \frac{9\sqrt{3}}{8\pi} P_{cl} \frac{\gamma_\gamma}{\gamma_c} \int_{\gamma_\gamma/\gamma_c}^{+\infty} K_{5/3}(y) dy, \tag{1.16}$$

with $\gamma_c \equiv (3/2)\gamma_e \eta/\alpha$ is called "critical energy" and corresponds to the energy value for which the function is maximized, and $\alpha = e^2/(4\pi\epsilon_0 \hbar c) = 1/137$ called *fine structure constant*. The typical shape of eq.(1.16) can be visualized in figure 1.2, defining $F(y) = (1/P_{cl})(dP_{inst}/d\gamma_\gamma)$ and $y = \gamma_\gamma/\gamma_c$ as is done in [6].

1.1.3   Classical radiation reaction

Photon emission is a very general term used to group all phenomenons for which energetic charged particles can radiate away part of their energy. The emission of a photon causes a feedback on the particle energy and momentum according to their conservation laws, we call these feedback *Radiation Reaction* (RR).

---

[1]It is true however that in astrophysics and in large particle accelerators we find systems in which also heavier particles radiate (i.e. accretion disks or in the *Large Hadron Collider*) but those system are not in the interest of this thesis and so whenever we will talk about a radiating particle we will always refer to electrons.
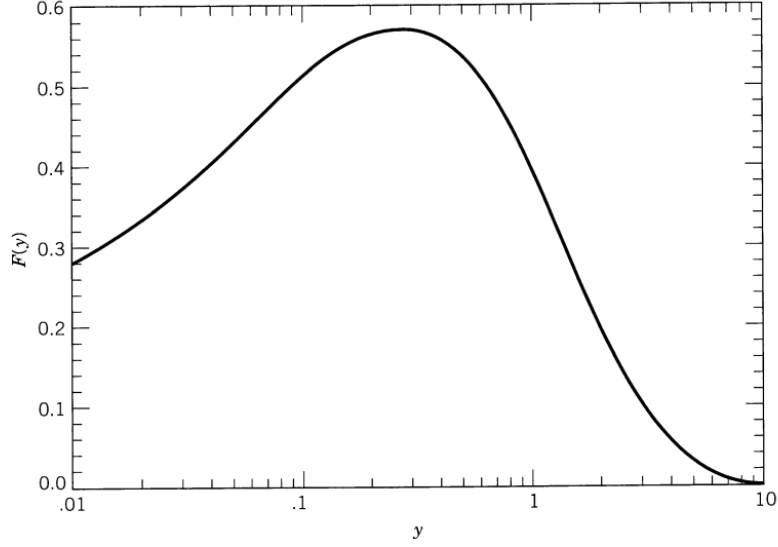
Figure 1.2: Plot of $F(y) = (1/P_{cl})(dP_{inst}/d\gamma_\gamma)$ vs $y = \gamma_\gamma/\gamma_c$ with logarithimic scale abscissa.[6]

Classically the motion of a charged particle in an electromagnetic field can be solved by writing Newton equations and consider Lorentz force as an external force acting on the particle. In the four-vector notation this would read:

$$m\frac{du^\mu}{d\tau} = qF^{\mu\nu}u_\nu, \qquad (1.17)$$

where $F^{\mu\nu}$ is the elctromagnetic tensor defined as in eq.(1.12) and $u_\nu = p_\nu/(\gamma mc)$ is the normalized relativistic linear momentum of the particle.

The most intuitive way of thinking of radiation reaction would be to add an extra term to express the field of the emitted radiation acting as a feedback on the external fields. The system to be solved now looks like [7]:

$$m\frac{du^\mu}{d\tau} = q\left(F_{ext}^{\mu\nu} + F_{rad}^{\mu\nu}\right)u_\nu, \qquad (1.18)$$

$$\partial_\mu F_{rad}^{\mu\nu} = q\int u^\mu(\tau)\delta(x - r(\tau))d\tau, \qquad (1.19)$$

where $F_{rad}^{\mu\nu}$ is the feedback term and $F_{ext}^{\mu\nu}$ represents the external fields.

The solution of this system is not trivial and goes beyond the purpose of this work so we will just say that a first approach has been used by Lorentz, Abraham and Dirac to derive the homonimous eqaution published in 1938 (Lorentz-Abraham-Dirac equation or LAD equation). Later in 1947 another famous equation was published: the Landau-Lifshitz (LL) equation. The real and physical solution to this equation is shown to be [9]:

$$mc^2\frac{d\gamma_e}{dt} = -e\boldsymbol{v}\cdot\boldsymbol{E} - ec\gamma_e\tau_0\boldsymbol{v}\cdot\frac{d\boldsymbol{E}}{dt} + \tau_0 c\boldsymbol{E}\cdot(\boldsymbol{E} + \boldsymbol{\beta}\times\boldsymbol{B})$$

$$+ \frac{\tau_0 e^2}{m_e}\boldsymbol{E}\cdot(\boldsymbol{E} + \boldsymbol{v}\times\boldsymbol{B}) - \frac{\tau_e^2}{m_e}\gamma_e^2\left[(\boldsymbol{E} + \boldsymbol{\beta}\times\boldsymbol{B})^2 - (\boldsymbol{\beta}\cdot\boldsymbol{E})^2\right], \quad (1.20)$$

$$\frac{d\boldsymbol{p}}{dt} = -e\left(\boldsymbol{E} + \boldsymbol{v} \times \boldsymbol{B}\right) - e\gamma_e\tau_0\left(\frac{d\boldsymbol{E}}{dt} + \boldsymbol{\beta} \times \frac{d\boldsymbol{E}}{dt}\right)$$

$$+ \frac{e^2\tau_0}{m_e c}\gamma_e^2\left[(\boldsymbol{\beta} \cdot \boldsymbol{E})\boldsymbol{E} - c\boldsymbol{B} \times (\boldsymbol{E} + \boldsymbol{v} \times \boldsymbol{B})\right] - \frac{e^2\tau_0}{m_e c}\gamma_e^2\left[(\boldsymbol{E} + c\boldsymbol{\beta} \times \boldsymbol{B})^2 - (\boldsymbol{\beta} \cdot \boldsymbol{E})^2\right]\boldsymbol{\beta},$$

$$(1.21)$$

for which we defined $\tau_0 = (2/3)\tau_e$, and $\boldsymbol{\beta} = \boldsymbol{v}/c$. Remembering how we defined the quantity P_{cl} in eq. (1.10) and assuming to be in ultra-relativistic regime ($\gamma \gg 1$) we can rewrite the equations leaving only the important terms:

$$mc^2\frac{d\gamma}{dt} = qc\boldsymbol{E} \cdot \boldsymbol{\beta} - P_{cl}, \tag{1.22}$$

$$\frac{d\boldsymbol{p}}{dt} = q\left(\boldsymbol{E} + c\boldsymbol{\beta} \times \boldsymbol{B}\right) - \boldsymbol{\beta}P_{cl}. \tag{1.23}$$

The simplest physical system we can look at to show the effect of classical radiation reaction is a single electron moving into a uniform and constant magnetic field perpendicular to the velocity of the particle. If no radiation were emitted, the electron trajectory would be a circle with radius $r_L = mv/(eB)$, angular frequency $\omega_L = eB/(2m)$ and, centripetal acceleration $a_L = |\boldsymbol{F}_L|/m = qvB/m$. We can notice that the larger the particle speed (and so the particle kinetic energy), the larger the radius and, the larger the magnitude of the centripetal acceleration. We saw in section 1.1 that the bigger the acceleration of the particle, the more radiation is emitted, so just from this qualitative analysis we can assume that the emitted power of a faster particle would be greater than the one of a slower particle. This agrees at first order with the idea of a continuous particle slowing down until $\gamma = 1$, when no more kinetic energy is stored in the particle. Quantitatively we can refer to [7] and find an equation to describe $\gamma(t)$:

$$\frac{d\gamma(t)}{dt} = K(1 - \gamma^2), \tag{1.24}$$

where we defined $K = \tau_0 B^2/(m\Omega)$ with $\Omega = 2\omega_L$. Once integrated it gives the solution:

$$\gamma(t) = \tanh\left[\text{atanh}\left(\gamma(0)\right) + Kt\right] \approx \frac{\gamma(0)}{1 + Kt} \text{ for } \gamma(0) \gg 1. \tag{1.25}$$

This solution clearly shows that the higher the energy the bigger the negative slope of $\gamma(t)$ so the faster the particle loses energy, tending asymptotically to arrive smoothly at the value $\gamma = 1$. This case can be shown to yield to a trajectory with the shape of a closing spiral.

1.2 Quantum radiation emission and back reaction

1.2.1 Inverse Compton scattering and quantum parameters

An electron moving into an electromagnetic field can exibit behaviours which description needs a quantum approach. In the regime where quantum effects are not negligible, determining the spectral properties of the emission radiated away by an electron in an arbitrary external field is greatly simplified when considering ultra-relativistic electrons (i) in the presence of a large slow-varying field (ii) with respect to the characteristic time scale for photon production [10]. These two conditions can

shown to be fulfilled if (i) $\gamma_e \gg 1$ and (ii) [10]

$$a_0 = \frac{e|A^\mu|}{m_e c^2} \gg 1, \tag{1.26}$$

with A^μ being the four potential related to the electromagnetic tensor $F^{\mu\nu} = \partial^\mu A^\nu - \partial^\nu A^\mu$. The quantity a_0 is often called "normalized vector potential" and is a measure of the strength of the electromagnetic field in a point in space.

Respecting the aforementioned conditions allows us to assume that the dominant photon emission process in the system is the *inverse Compton scattering* which is the quantum generalization of the synchrotron emission [10], for which the rate of photon production has been derived in [5] and will be given in eq.(1.36). Before that we need to introduce some parameters of fundamental importance in order to understand eq.(1.36), namely, χ_e and χ_γ.

We will now define the electron quantum parameter χ_e which is tightly correlated to the relative prominence of quantum effects. For χ_e values up to $\sim 10^{-3}$ a classical approach is considered sufficient to describe the system, for values larger than $\sim 10^{-2}$ then quantum effects start to be relevant (or even prominent) and should be taken into account for a correct description. The quantum parameter χ_e is defined as:

$$\chi_e \equiv \left| \frac{F^{\mu\nu} p_\nu}{E_s m_e} \right| = \frac{\eta}{\alpha}, \tag{1.27}$$

in which m_e is the electron rest mass, c is the speed of light in vacuum and $F^{\mu\nu}$ is the electromagnetic tensor defined in eq.(1.12), and $\alpha = e^2/(4\pi\epsilon_0 \hbar c) = 1/137$ is the *fine structure constant*, while E_s is called "Schwinger field" which is defined as:

$$E_s = \frac{m_e^2 c^3}{\hbar e} = \alpha E_{cr} \approx 1.3 \times 10^{18} \frac{V}{m}. \tag{1.28}$$

The Schwinger field E_s can be thought as the electromagnetic field amplitude limit at which the behaviour of EM waves in the vacuum becomes non-linear. In classical electrodynamics, two light beams crossing their path just add their amplitude in the crossing point but pass right through each other. This is true until the combined energy of the two beams is not high enough to start the *vacuum polarization* effect. From this point of view, χ can be seen as the ratio between the electromagnetic field experience by the particle in its proper frame by the Schwinger field, if $\chi \geq 1$ then the pair production process is possible and we enter the fully quantum regime.

The quantum paramenter for a single electron moving into an electromagnetic field can be rewritten as follows:

$$\chi_e = \frac{\gamma_e}{E_s} \left| -(\boldsymbol{\beta} \cdot \boldsymbol{E})^2 + (\boldsymbol{E} + \boldsymbol{v} \times \boldsymbol{B})^2 \right|^{1/2}. \tag{1.29}$$

One can also project the electric field in its parallel and perpendicular component relatively to the electron direction of motion and also, assuming that the electron is ultra-relativistic ($\gamma_e^2 \gg 1$) we can simplify the relation which now reads:

$$\chi_e = \frac{\gamma_e}{E_s} \left| \frac{\boldsymbol{E}_\parallel}{\gamma_e^2} + (\boldsymbol{E}_\perp + \boldsymbol{v} \times \boldsymbol{B})^2 \right|^{1/2} \approx \frac{\gamma_e}{E_s} |\boldsymbol{E}_\perp + \boldsymbol{v} \times \boldsymbol{B}|. \tag{1.30}$$

In order to look at the electromagnetic field in the correct way we should either always specify the reference frame in which all the quantities are measured or transform them into Lorentz invariant, ensuring in this way that they are the same in every

inertial reference frame. Since the second option seems more appealing, we will try to discuss, when possible, in term of Lorentz invariants. In order to do so we define the normalized vector potential of the wave similarly to what we have already done in eq.(1.26) :

$$a_L = \frac{e|\boldsymbol{A}|}{m_e c} = \frac{eE_0}{m_e c \omega_0}. \tag{1.31}$$

$\boldsymbol{A}$ has been already defined right after eq.(1.26), and can be thought as the ratio between the amplitude of the electric field of a plane wave and its frequency ω. Eventhough we will work exclusively with pulses which are not plane waves and therefore are not made by a single frequency but by a broad spectrum of frequancies, we will keep using this notation but instead of the plane wave frequency ω, we will use the central frequency ω_0.

The case of a single electron moving uniformly into the field generated by a plane wave is too simple to give an accurate description of complex systems, but is enough to give us a basic understanding of some properties of the processes at play in a wide range of situations. So for a particular case of a single electron moving with $\boldsymbol{v}_e$ parallel to the x-axis which is also the progation direction of a plane wave described as:

$$\boldsymbol{A} = A_L sin \left[\omega_0 \left(x - \frac{t}{c} \right) \right] \boldsymbol{n}_j, \tag{1.32}$$

with $\boldsymbol{n}_j$ the versor of the y-axis. In this case the quantum parameter becomes:

$$\chi_e = \frac{\gamma_e \omega_0 A_L}{E_s} \cos(\omega_0 t) \left[1 - \frac{\boldsymbol{v} \cdot \boldsymbol{n}_i}{c} \right]. \tag{1.33}$$

It should be pointed out that this relation reaches the maximum value if the electron moves in the opposite direction of the propagation of the wave while has a minimum if their propagation is co-directional. The maximization of this parameter is of the utmost importance in order to enhance the photon emission.

Similarly to what done for χ_e we can define a correlated parameter called "photon quantum parameter":

$$\chi_\gamma \equiv \left| \frac{F^{\mu\nu} \hbar k_\nu}{E_s m_e} \right| = \frac{\gamma_\gamma}{E_s} \left| \boldsymbol{E}_\perp + \boldsymbol{v} \times \boldsymbol{B} \right|, \tag{1.34}$$

with γ_γ being the photon energy normalized to $m_e c^2$. Now we can derive the following relation, which will be useful later on, in the assumption of $\boldsymbol{E}_\parallel \approx 0$:

$$\chi_e \gamma_\gamma \approx \chi_\gamma \gamma_e. \tag{1.35}$$

1.2.2 Quantum radiation reaction

Deriving the photon emissin rate for an arbitrary field is too complex, so we will instead place ourselves in the Local-Constant-Field-Approximation (LCFA), assuming that the characteristic time of emission is much smaller than the optical cycle of the external field, and that the Schwinger field is much larger than the external field amplitude [7] [4], and we assume fulfilled all the hypothesis at the beginning of section 1.2.1.

For a single electron the inverse Compton scattering spectral emission rate has been first derived in [5] and reads:

$$\frac{d^2 N_\gamma}{d\tau d\chi_\gamma} = \frac{2\alpha^2}{3\tau_e} \frac{G(\chi_e, \chi_\gamma)}{\chi_\gamma}, \tag{1.36}$$

where τ is the electron proper time, and $\tau_e = r_e/c$ is the time for the the light to cross the classical electron radius defined as $r_e = e^2/(4\pi\epsilon_0 m_e c^2)$.
$G(\chi_e, \chi_\gamma)$ is the quantum emissivity:

$$G(\chi_e, \chi_\gamma) = \frac{\sqrt{3}\chi_\gamma}{2\pi\chi_e} \left[\int_\nu^{+\infty} K_{5/3}(y)dy + \frac{3}{2}\chi_\gamma \nu K_{3/2}(\nu) \right], \qquad (1.37)$$

in which K_n is the modified Bessel function of second kind of order n and:

$$\nu = \frac{2\chi_\gamma}{3\chi_e(\chi_e - \chi_\gamma)}. \qquad (1.38)$$

We can link directly the photon quantum parameter at the emission instant to the electron quantum parameter defining the following useful parameter:

$$\xi \equiv \frac{\gamma_\gamma}{\gamma_e}. \qquad (1.39)$$

We can now use the eq.(1.35) to obtain:

$$\chi_\gamma = \xi\chi_e. \qquad (1.40)$$

Let us now consider a specific reference frame in which the electron is ultra-relativistic, we will hencefort call this frame the laboratory-frame (or lab-frame). The instantaneous power spectrum of the emitted photons can be obtained from eqs. (1.36) and (1.37):

$$\frac{dP_{insta}}{d\gamma_\gamma} = \frac{P_\alpha}{\gamma_e}G(\chi_e, \chi_\gamma) = \frac{\sqrt{3}\xi}{2\pi\gamma_e}P_\alpha \left[\int_\nu^{+\infty} K_{5/3}(y)dy + \frac{3}{2}\chi_\gamma \nu K_{3/2}(\nu) \right], \qquad (1.41)$$

in which $P_\alpha = P_{cl}/\chi_e^2$ with P_{cl} being the classical Larmor radiated power defined as in eq.(1.10).
A more compact and easier to handle relation for the classical power can then be found as:

$$P_{cl} = \frac{2\alpha(m_e c^2)^2}{3\hbar}\chi_e^2. \qquad (1.42)$$

Integrating eq.(1.41) we obtain the "quantum corrected instantaneous power radiated by the electron" that reads:

$$P_{rad} = P_{cl} \cdot g(\chi_e) = P_{cl}\frac{9\sqrt{3}}{8\pi} \int_0^{+\infty} \left[\frac{2\nu^2 K_{5/3}(\nu)}{(2 + 3\nu\chi_e)^2} + \frac{4\nu(3\nu\chi_e)^2}{(2 + 3\nu\chi)^4}K_{2/3} \right] d\nu. \qquad (1.43)$$

$g(\chi_e)$ is called "quantum correction" and can be shown to converge towards unity for small enough χ_e ($\leq 10^{-2}$) bringing us back to the classical case. Looking at figure 1.3 two things can be understood. The first is that higher χ_e means higher energy of the emitted radiation as one can see looking at the differences between curves of different colors. The second is that approaching $\chi_e \sim 0.1$ a fully classical description is not sufficent anymore, and a quantum correction is needed. Increasing even more the value of χ_e, the quantum nature of radiation reaction becomes preminent ad a fully quantum approach is needed.
Quantum radiation reaction results from the cumulative effects of energy and momentum loss of the charged particles emitting photons. As in QED high energy photon emission is a random process, its modelling usually relies on Monte Carlo
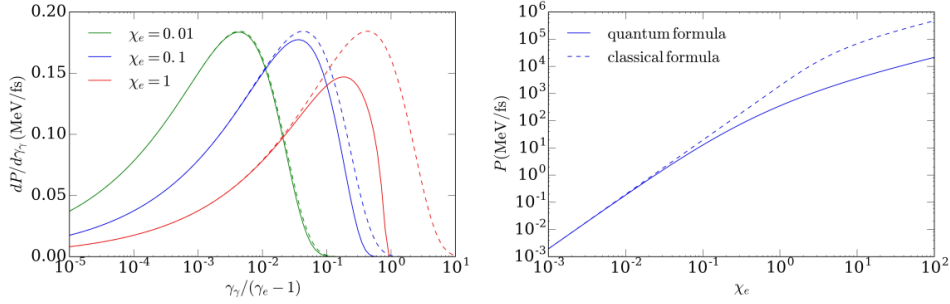
Figure 1.3: Classical power radiated vs quantum corrected formula. It is clear how the agreement between calssical and quantum description becomes weaker the bigger χ_e becomes. In particular we can see how the emmision at the high end of the spectrum is overestimated by the calssical approach.[4]

methods [11] [12][13].
In these methods we draw randomly the time of emission and the energy of the emitted photon. For the limit of $\chi_e \ll 1$ it has been shown [10] that this approach is equivalent of applying eq.(1.43).
A fully quantum approach is already available in *Smilei*[7][3]. The details on how this approach is implemented in the code will be discussed later on in section 3.8.

1.3   Emission by many charged particles

Up to now we described systems with only one electron emitting radiation, now we will see that the radiation emitted by a many-particle system is characterized by properties which in general are not the sum of the features of many single electron systems.
In general any kind of radiative behaviour can be classified as either "coherent" or "incoherent"[10][14]. The first means that nearby particles collectively contribute to the radiation emission, while the second kind of behaviour means that each particle emits independently from each other. We know that the emission of a single particle is deeply affected by the electric field in its surroundings, so if the space scale of the fields inhomogeneities is of the order of or smaller than the average distance between the particles, then each particle has to emit indpendentely from each other since the environment in which is found is remarkably different from the others. For the case of a typical laser pulse of $\lambda_L \sim \mu$m the scale at which the field varies can be estimated roughly to $\lambda_L/10 \div 100$, so about $10^2 \div 10^1$nm. The typical distance between electrons in an NCD plasma would be of the order of $n_c^{-1/3} \sim$nm, meaning that on average we find tens if not hundreds of electrons in the characteristic spatial scale for variation of the fields. In this range we find both coherent and incoherent radiation emission and, PIC codes have different way to account for the two of them. Figure 1.4 shows a depiction of coherent and incoherent photon emission.
  We have already shown in eq.(1.9) that in the case of a single radiating particle, the radiated power is proportional to the charge squared of the radiating particle, so $P_{inc}^s \propto q^2$ with "s" indicating the species. To compute the total power radiated we then need to sum the single particle power over all the N_s particles, and being electrons the only particles radiating in our regimes we can write $P_{inc} \propto N_e e^2$.
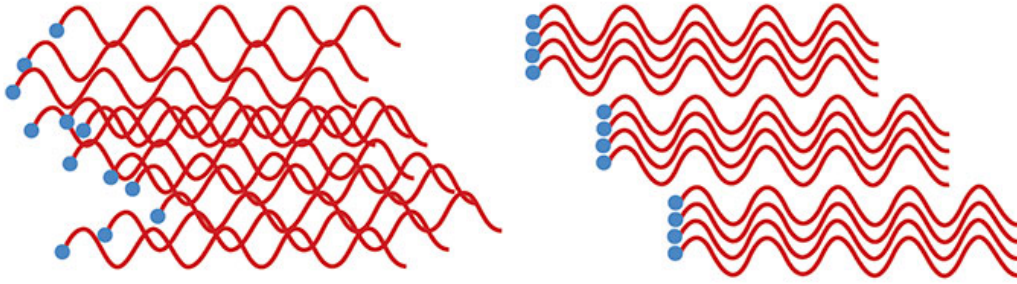
Figure 1.4: Depiction of incoherent radiation (left) and coherent radiation (right). Reprinted from [15].

On the other hand if all the electrons radiates in unison then, they are like a big particle of charge $q = N_e e$ radiating. Since the power is proportional to the square of the charge of the radiating particle then we get $P_{coh} \propto N_e^2 e^2$ which can be significantly different from P_{inc} depending on the physical system.

As we will se in chapter 3, coherent radiation is not well described above a certain energy threshold in *Particle-In-Cell* codes like the one we used in this work, so it would be appropriate to study systems for which the coherent component is negligible with respect to its incoherent counterpart. Fulfilling the following hypothesis grants exactly that:

1. Slow varying field with respect to the characteristic photon formation time Δt_γ

2. Collisional effects among particles, and in particular electrons, are negligible

3. Wavelength of the emitted photon $\lambda_\gamma \ll n_c^{-\frac{1}{3}}$

Condition number one ensures that the environment in which the electron is does not vary in the time needed for the electron to emit the photon. This hypothesis translates to the fact that, from the electron point of view the process of emission is almost instantaneous. Its practical effect is that the photon is emitted in the forward-direction, which is the same as the electron instantanoeus velocity. It can be shown that this condition is verified for $a_0 \gg 1$ [10][14].
The third condition is related to the first one since has been shown that $\lambda_\gamma \propto \Delta t_\gamma$ [10], but gives us a more direct measure of the photon energy intervall in which we are committing a negligible error not modelling the coherent radiation. With a 800nm laser we get a critical density of $n_c \approx 1.7 \times 10^{21} \text{cm}^{-3}$ which, recalling condition 3 above, transalte into $\lambda_\gamma < 0.8$nm, which in energy becomes $h\nu_\gamma \sim 1.5$KeV or equivalently $\gamma_\gamma > 3 \times 10^{-3}$.
An awkward interval is formed between the minimum energy required for incoherent emission dominance ($\gamma_\gamma > 3 \times 10^{-3}$) and the maximum energy for which the code can account for coherent radiation ($\gamma_\gamma < 5 \times 10^{-4}$ in our specific set up). Following the hypothesis above grants us the negligibility of the emitted energy in this "uncon-fortable middle-ground" and relying only on the much more confortably modelled incoherent emission. For a deeper reading on the topic we refer to [14].
We will always refer to incoherent radiation whenever we use terms such as "photons", "radiation" or similar, unless otherwise specified.

Chapter 2

Laser-plasma interaction

In the previous chapter we discussed how energetic electrons in strong fields can radiate, now we will summarize how energetic electrons are produced using an ultra-intense laser pulse.

After a brief introduction of state-of-the art high intensity lasers, the discussion will start with an overview of the interaction between electrons and pulsed lasers, defining different regimes of interaction. We will see how energetic electrons are produced in various regimes, and in particular in the one we are interested in: the Near-Critical regime.

Finally, when we understand how energetic electrons are created, we will discuss how those electrons behave in the system. Radiation emission is the phenomenon in which we are interested the most, but is not all those electrons will lead to. As we will see, a hot plasma naturally expands, and gives rise to a complex dynamics in which also ions are involved. Although we are not directly interested in ion acceleration, we will briefly describe how ions are accelerated by energetic electrons and their effect on the dynamics of the system in order to have a more complete picture.

In order to keep the focus on the specific work of this thesis we will only talk about near-critical-density (NCD) plasmas and in particular we will always assume that we are in the overcritical regime, unless specified otherwise. For a more general treaty of Laser-Plasma interaction we refer to [16][17].

2.1 Multi-PetaWatt Lasers

Since the invention of *Chirped Pulse Amplification* (CPA) (1985) [18] the power of laser facilities has grown at an incredible rate (Fig.2.1).

Through new records in laser intensity, it has been possible to access relativistic laser-matter interaction, which allowed us to experimentally explore new physical mechanisms.

Before 1985 the maximum achievable laser intensity had reached a saturation value due to the fact that higher itensities would have damaged the amplification medium. An elegant solution to this problem is to expand the pulse before amplification reducing its intensity, amplify this weaker pulse, and then compress it to the desired duration afterward.

Nowadays the most powerfull laser facilities all use CPA-based technology and they are divided into two cathegories (summarized in fig.2.2):

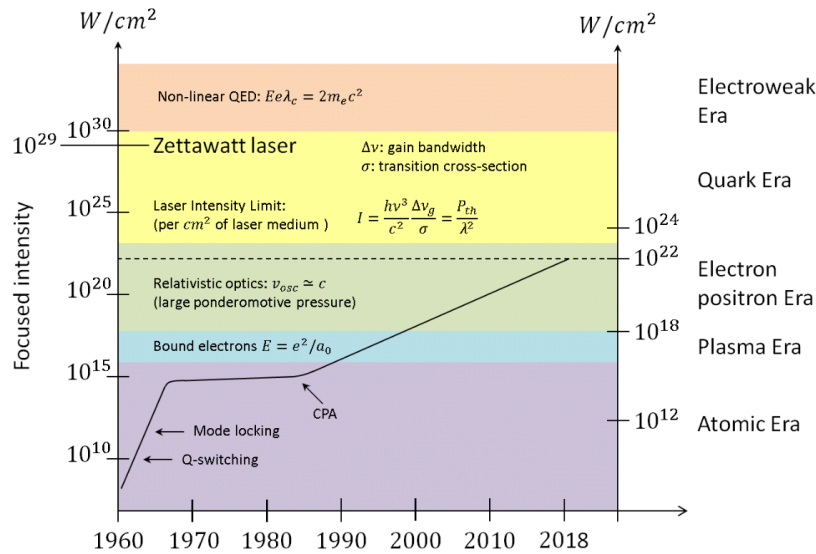- High Energy Density (HED)

- Ultra High Intensity (UHI)

Figure 2.1: Evolution of laser intensities from the '60s to 2018.[19]

To the first belong all facilities capable of delivering $\sim$ kJ of energy per pulse, with a typical pulse duration of $\sim ns$. These facilities are often used for the study of warm matter and are fundamental in fields like (but not exclusive to) planetology, hydrodynamic plasma instabilities and, inertial confinement fusion. In order to achieve MJ order of energy multiple beams are used simultaneously as in the *Nationl laboratory for Inertial Fusion* (NIF) and *Laser MegaJoule* (LMJ) facilities.

Ultra High Intensity Lasers are obtained when compressing a smaller energy ($\sim 10^2$J)
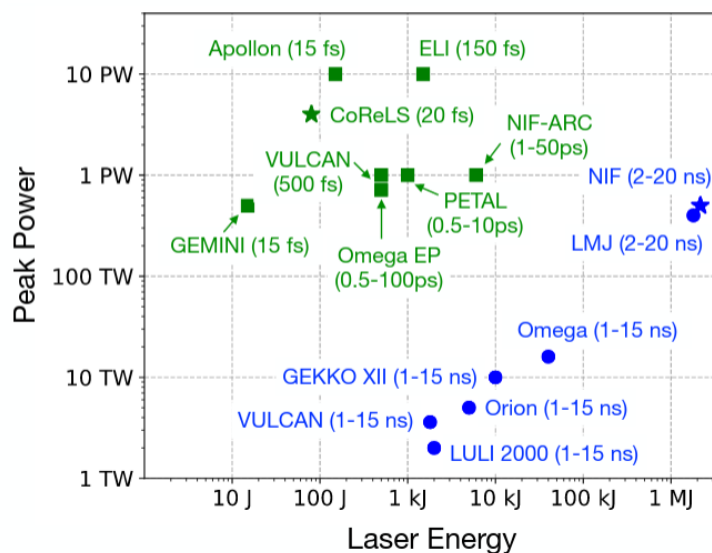
Figure 2.2: Main UHI (green) and HED (blue) facilities in the world.

into a ultra-short pulse ($\sim 10^1$fs $\div$ ps) allowing us to achieve intensity values of $\geq 10^{21}Wcm^{-2}$ and powers of the order or higher than ~ 1 PW. Another important difference between UHI and HED is the repetition rate. The bigger the energy the

longer the amplification medium takes to cool down, causing a MJ facility to be able to shoot at full power only few times per day. On the other hand UHI lasers can shoot as much as few times per minute, having "only" few tens or hundreds of Joules to dissipate. In particular we will focus on the UHI facility *Apollon* being built at the CEA site in Saclay, France. The system is a Titanium:Sapphire based laser able to deliver pulses with duration (Full-Width-Half-Maximum in time) of ~ 20fs. This facility is scheduled to start experiments in Spring 2020 with a peak power on target of about 1PW, and in few years reach almost 10PW. We will discuss its specific parameters and its modelling in section 4.1.

Our goal is to shoot a powerful laser pulse onto a target, transforming it into a plasma, and then exploit some features of the laser-plasma interaction in order to create the favorable condition to radiate away γ-photons. We will see that the quality of this interaction is determined by the properties of both plasma, and laser.

2.2 Single particle interaction

First we want to look at a very simple system that is far away from reality but nonetheless it can give us insights about the description of a more complex system. Let's follow more or less [20] and consider a single non-relativistic electron interacting with a laser pulse of central frequency ω propagating along $\boldsymbol{k}$:

$$\boldsymbol{E}(\boldsymbol{x}, t) = \boldsymbol{E}_0(\boldsymbol{x}) \cos(\boldsymbol{k} \cdot \boldsymbol{x} - \omega t). \tag{2.1}$$

In order to simplify the notation we writing the cosine phase as ϕ. To describe the dynamic of the system we have to solve Newton equation of motion:

$$\ddot{\boldsymbol{x}} = \frac{q}{m_e} \left(\boldsymbol{E} + \dot{\boldsymbol{x}} \times \boldsymbol{B} \right). \tag{2.2}$$

We will look at an approximate solution using the linearized equation. First we need to use a perturbative approach and write:

$$\boldsymbol{x} = \boldsymbol{x}^{(0)} + \boldsymbol{x}^{(1)}, \tag{2.3}$$

in which the first term is the solution to the linearized equation (order zero dynamics) and the second is the perturbative effect (first order dynamics). Expanding the field around the electron position $\boldsymbol{x}_e$:

$$\boldsymbol{E} \approx \boldsymbol{E}(\boldsymbol{x}_e) + \left[\left[(\boldsymbol{x} - \boldsymbol{x}_e) \cdot \nabla \right] \boldsymbol{E} \right]_{x=x_e}. \tag{2.4}$$

Now we are able to linearize eq. (2.2) and solve for $\boldsymbol{x}^{(0)}$:

$$\boldsymbol{x}^{(0)} = \boldsymbol{x}_e - \frac{q\boldsymbol{E}_0(\boldsymbol{x}_e)}{m_e\omega} \cos(\phi) = \boldsymbol{x}_e - \frac{\boldsymbol{v}^{(0)}}{\omega} \cos(\phi). \tag{2.5}$$

Plugging relation (2.3) into eq.(2.2) we can derive an expression for $\boldsymbol{x}^{(1)}$:

$$\ddot{\boldsymbol{x}}^{(1)} = - \left(\frac{q}{m_e\omega} \right)^2 \left[(\boldsymbol{E} \cdot \nabla)\boldsymbol{E} + \boldsymbol{E}_0 \times \nabla \times \boldsymbol{E}_0 \sin^2 \phi + (...) \sin \phi \cos \phi \right]. \tag{2.6}$$

The first term is function only of the spatial dishomogeneities while the last two terms depend also on time, oscillating with frequency 2ω. Averaging over the laser period ($\langle \rangle$) we can get rid of these two terms:

$$m_e \frac{d^2 \left\langle \boldsymbol{x}^{(1)} \right\rangle}{dt^2} = -\frac{q^2}{4m_e\omega^2} \nabla |\boldsymbol{E}_0|^2 = \boldsymbol{F}_p, \tag{2.7}$$

which is called *Ponderomotive force*. We should notice that $\boldsymbol{F}_p$ is inversely proportional to the mass of the particle, this implies that only electrons would effectively react to it while ions are left almost in place. This consideration means that neutral atoms would get ionized and electrons would be pushed away from the ions and induce charge separation.

Associated to this force we can fid the *Pondromotive potential*:

$$U_p = \frac{q^2}{4m_e\omega^2}|\boldsymbol{E}_0|^2. \tag{2.8}$$

If accounting for relativistic effects is needed then remembering the definitions (2.15)(2.16) the ponderomotive force becomes [21]:

$$\boldsymbol{F}_p = -m_ec^2\nabla\gamma = -m_ec^2\nabla\sqrt{1 + \langle\boldsymbol{a}^2\rangle}. \tag{2.9}$$

In a non-relativistic regime the main effect of $\boldsymbol{F}_p$ is to push electrons toward regions of space in which U_p is lower, corresponding to smaller field magnitude.

This basic concept of Ponderomotive force can be extremely useful to understand the processes at play in all regimes.

A real system is never a single particle, so is far more complicated than what we saw in this section. A collection of charged particles is a plasma, and depending on its actual charge density we find very different behaviours and different physical mechanisms.

2.3   Regimes of interaction

Before discussing the different regimes of interaction we would like to present a few key parameters which help to describe a plasma. The characteristic length for the phenomena in a plasma is called *Debye length* or *Lambda-Debye* and is defined as:

$$\lambda_D = \sqrt{\frac{\epsilon_0 T_e}{e^2 n_e}}, \tag{2.10}$$

with ϵ_0 being the vacuum dielectric permittivity, and T_e the electronic temperature. Electrons have a priviliged spot in the study of laser-plasma interaction with respect to the ions, since their dynamics is generally much faster than the ions and guides the overall behaviour of the plasma. We will see now why.

The fundamental time scale of the dynamics in a plasma is related to what is called *Plasma frequency* or *Omega-plasma* and is definde as:

$$\omega_p = \sqrt{\frac{q_s^2 n_s}{\epsilon_0 m_s}}, \tag{2.11}$$

with "s" the species considered. It is clear that each species in the plasma will have a different value of ω_p depending on their mass and charge. The time scale can then be defined as $2\pi/\omega_p$.

Let's notice that the mass of the species is in the denominator of the fraction, thus ions respond much slower than electrons to electromagnetic stimuli. In the frame of this work the electron response time is always much faster than the ions, thus we will always assume that any electromagnetic perturbation (the laser pulse) interacts

only directly with the electrons. All processes which result in ions gaining energy are always mediated by electrons and will be briefly described in section 2.6. Henceforth when we will talk about the plasma frequency we will always refer to the electronic plasma frequency, unless otherwise specified.

Depending on the electron number density we can divide the laser-plasma interaction into three regimes: *subcritical* (or *undercritical*), *near-critical* and, *overcritical*. The main difference we want to focus on is if an electromagnetic wave can propagate or not in a plasma of given density.

It is crucial to define the so called *critical density* n_c given by:

$$n_c = \frac{\epsilon_0 m_e \omega_0^2}{e^2} = 1.1 \times 10^{21} cm^{-3} \left(\frac{\lambda}{1\mu m} \right)^{-2}, \tag{2.12}$$

with ω_0 being the central frequency in the laser spectrum, m_e the electron rest mass and, e the proton charge. The complex index of refraction for a transverse monochromatic mode of a cold, collisionless, un-magnetized, non relativistic plasma can be expressed as [22]:

$$\widetilde{n} = \left(1 - \frac{\omega_p^2}{\omega_0^2} \right)^{\frac{1}{2}} = \left(1 - \frac{n_e}{n_c} \right)^{\frac{1}{2}}. \tag{2.13}$$

This expression is very simple and makes use of several restrictive hypothesis, nonetheless eq.(2.13) is usefull to show some crucial points.

If $n_e < n_c$ the index of refraction is real and thus the the electromagnetic wave can be transmitted, propagating through the plasma.

If otherwise $n_e > n_c$, $\widetilde{n}$ will have a non-zero imaginary part, then the equation for the propagating wave will have an exponential dumped amplitude meaning that the wave is not transmitted through the plasma. This is the case of an evanescent wave, which will propagate for a certain distance through the medium but will inevitably be reflected or absorbed during its path.

Therefore we call *subcritical* regime if $n_e < n_c$, *overcritical* regime if $n_e > n_c$ and, *near-critical* regime if $n_e \sim n_c$. The latter is a regime in which the interaction between an electromagnetic wave and a plasma grows in complexity, acting as a middleground between the two extremes. This is the regime we are interested in because it shows a strong laser-plasma coupling that we will try to exploit.

If the laser intensity rises above about $10^{18}\mathrm{Wcm}^{-2}$ then we access the relativistic regime, which leads to more complex physics. Qualitatively we can observe one of the effects of high intensity introducing the Lorentz factor γ as expressed below:

$$\gamma = \sqrt{1 + \langle \boldsymbol{a}^2 \rangle} = \sqrt{1 + \frac{a_0^2}{2}}, \tag{2.14}$$

with:

$$\boldsymbol{a} = \frac{e\boldsymbol{A}}{m_e c^2}, \tag{2.15}$$

$$\boldsymbol{E} = -\frac{\partial_t \boldsymbol{A}}{c}, \tag{2.16}$$

$$I = \epsilon_0 c \langle \boldsymbol{E}^2 \rangle, \tag{2.17}$$

$$a_0 = 0.85 \times \left(\frac{I\lambda^2}{10^{18}\mathrm{Wcm}^{-2}\mu\mathrm{m}^2} \right)^{\frac{1}{2}}, \tag{2.18}$$

in which the angled brackets mean the average taken over a laser period, and $\boldsymbol{A}$ has been defined in section 1.2.1. Relation 2.14 is true only for linearly polarized waves, for circular polarization the argument of the square root becomes $1 + a_0^2$.

The electron mass m_e should then become γm_e and so n_c becomes γn_c. Since $\gamma > 1$ we can see that in relativistic regime a classically overcritical plasma can become subcritical and in so doing also "transparent" to the wave. This mechanism is called "Self-induced relativistic transparency" or "relativistic transparency" for short[16][17]. If the intensity of the laser is high enough to access the relativistic regime then the dynamic of the system grows in complexity also due to non-linear effects. The interaction of this evanescent wave with a near-critical plasma results in electron heating mechanisms which modelling is not trivial at all. The outcome is a plasma which has become hotter thanks to the energy left by the laser. This hot electron plasma will give rise to a wide range of phenomena some of which will be investigated in this work.

It is crucial to point out that as has been shown in past works[23] what really defines the dynamics and the mechanisms at play in the system is not a single parameter of the laser or of the plasma, but instead is the coupling of all the parameters of both plasma and laser which defines the overall interaction. This topic will be addressed when discussing the choice of the specific simulation set-up for this work in chapter 4.

2.4   Overview on undercritical and overcritical regime

The main focus of this work is on the Near-Critical-Density (NCD) plasma ($n_e \sim n_c$) but this regime is a middle ground between the overcritical and undercitical. So in order to understand the mechanisms at play in the NCD regime we need to give a brief overview on both subctricial and overcritical regimes evethough they are not the main focus of this work.

If the plasma in which a laser is propagating is considered deeply subcritical ($n_e \ll n_c$) then depending on the electromagnetic (EM) wave frequency, a longitudinal plasma wave can be excited in the direction of the pulse propagation. When the pulse arrives the field is increasing, pushing electrons forward as we have seen in section 2.2. Since the electrons are slower than light, the laser surpasses them pushing now backward. In a subcritical system the result can be a collective plasma oscillation called *Wakefield*.

The phase velocity of the electron wave is given by the laser group velocity [24] and, recalling eq.(2.13) reads:

$$v_{ph}^{wake} = c \left(1 - \frac{\omega_p^2}{\omega_0^2} \right)^{\frac{1}{2}} = v_g^{laser}, \qquad (2.19)$$

in which the plasma frequency ω_p is defined as in eq.(2.11) and ω_0 is the laser central frequency.

An externally injected electron can ride this *wake* staying in phase with the pulse itself and co-propagate with it. This mechanism generate a quasi-monoenergetic electron bunch in the direction of propagation of the laser.

For proper laser frequencies the oscillation can become resonant, breaking the wave, causing the trapping of electrons near the maximum of the field. Those electrons are now dragged along with the pulse and accelerated (Figure 2.3) without the need of any electron to be externally injected.

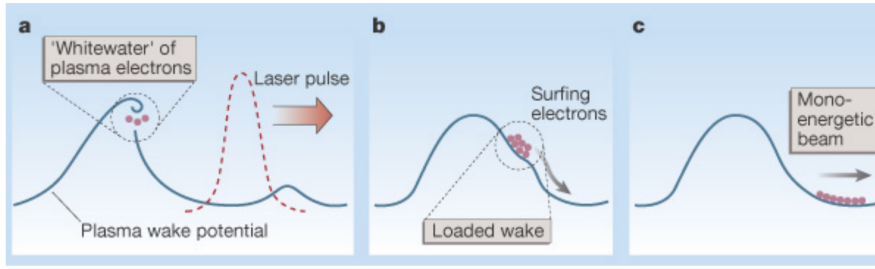In general, the process of accelerating electrons using the *wakefield* is called *Laser*

Figure 2.3: Physical picture of the laser wakefield acceleration mechanism (LWFA)[25].

WakeField Acceleration (LWFA) and is seen to be predominant in the deep subcritical regime [24].
Increasing the density, another physical process starts to be more and more effective: the so called *Direct Laser Acceleration* (DLA)[24].
The Ponderomotive force expels most of the electrons from the laser path creating a channel, and with it huge static magnetic and electric fields. The channel effectively acts like a potential well trapping the few electrons still inside it, making them oscillate at their *Betatron frequency* defined as $\omega_\beta = \omega_p/(2\gamma^{0.5})$. Can be shown that a resonance between the oscillating electrons and the laser is possible for appropriate frequencies [24]. Eploiting said resonances can be an effective way to accelerate electrons which are produced with a *quasi-thermal* spectrum.

In overcritical plasmas the effects are more complicated since the pulse is mainly reflected and the part of the wave propagating is actually evanescent. In these cases the laser can transfer fraction of its energy to the particles but it is referred to this phenomenon as *electron heating*, and will be the focus of the rest of this section.
The laser will always interact mainly with the electrons exploiting their relatively low inertia to tranfer them its energy. In this process the fields amplitudes will drop as the energy stored in them is absorbed by the electrons which will become "fast" or "hot". The exact modelling of the energy and temperature of these "hot electrons" is probably an impossible task, so usually we estimate these quantities with rather simple but effective scaling models.
The simplest is what is called "Ponderomotive model" or "Ponderomotive scaling" and is built on the assumption that the main actor in the electron acceleration is the so called "Ponderomotive force" $\boldsymbol{F}_p$ defined as in (2.9). From this can be estimated that the electron temperature would be roughly:

$$T_h = m_e c^2 (\gamma - 1). \tag{2.20}$$

This scaling is rather simple and easy to use but it does not take into account any effect of polarization nor incidence angle of the laser pulse on the target. In order to include these latter, another scaling has been proposed [26] which is built from the two main heating mechanisms leading to electron heating: $\boldsymbol{J} \times \boldsymbol{B}$ heating, and Brunell effect.
$\boldsymbol{J} \times \boldsymbol{B}$ heating is caused by the oscillation of the ponderomotive force (PF)in the laser period. As we see in eqs. (2.9) and (2.14) the magnitude of the PF is actually a function of the field which is obviously oscillating in time. Working out the math properly we can write the PF as a steady contribution and an oscillating part. The first pushes electrons in the direction of the laser causing steepening in the electron

density distribution, while the second makes electrons go back and forth and actually heating them.

For what we said before it is reasonable to assume that for $\boldsymbol{J} \times \boldsymbol{B}$ heating the related temperature would be proportional to the ponderomotive scaling:

$$T_{J \times B} = C_1 T_{pond} = C_1 m_e c^2 (\gamma - 1), \tag{2.21}$$

with C_1 being a parameter depending on polarization, laser a_0 and thickness of the target.

As for Brunell heating a scaling can be found in [27]:

$$T_{Brunell} = C_2 m_e c^2 \sqrt{\left(1 + f^2 \frac{a_0^2}{2}\right)(\sin^2 \theta - 1) \tan \theta}, \tag{2.22}$$

with f being the field amplification factor due to reflection on the target, usually flat solid density targets can be approximated as perfect mirrors so $f \approx 2$. The angle of incidence is represented by θ and C_2 is a factor just like C_1.

The overall temperature can be expressed as the sum of these two heating effects:

$$T_e = T_{J \times B} + T_{Brunell}. \tag{2.23}$$

It is appropriate to address the fact that for normal incidence $\theta = 0$ Brunell heating has no effect while its importance increase with the incidence angle. A full study on the dependence of the parameters C_1 and C_2 can be found in [27].

It should be pointed out that several heating mechanisms exist apart from the two already mentioned, asuch as: *Collisional absorption, Sthocastic heating, Resonance absorption,* ad others. For all these mechanisms, scalings and models are proposed but they will not be discussed in this section, since the goal is not to give an exhaustive description of all heating mechanisms but only a brief overview on the meaning of "electron heating".

In the next section we will see how NCD targets are produced and employed in nowadays experiments.

2.5   Near-Critical regime and foam-based targets

The *Near-Critical* regime is the most complex of all. Its complexity derives from the fact that is neither a subcritical nor an ovecritical regime but is somewhere in between. We do not have a clear behaviour dominating the laser-plasma interaction, but many phenomena of both subcritical and overcritical plasmas may concurr. When a laser pulse interacts with a Near-Critical-Density (NCD) plasma we can see behaviour which is the combination of the other two extreme cases.

If a plasma is overcritical or "overdense", it does not let a laser pulse propagate acting as a mirror and the pulse is almost perfectly reflected from the target. On the other hand if the plasma is underdense or subcritical, a plasma wave may be generated transporting the energy as it propagates. If $n_e \sim n_c$ the pulse may be able to propagate through the plasma until is almost completely absorbed producing energetic electrons with a *quasi-thermal* spectrum.

The electron density of a regular solid target is usually several hundreds times the critical density and this makes most of traditionally employed targetry not really efficient when converting energy from pulse to electrons. In the last decades effort

has been put into developing a new class of solid-based targets with near-critical electronic density. The aim is to realize targets which have better laser-plasma coupling leading to a longer penetration of the pulse, and increase the number of energetic electrons and their temperature. TIn the frame of this work, these energetic electrons will be used to produce photons as discussed in chapter 1.

The critical density of a plasma is typically very low, in the order of magnitude of the density of the air(few mg/cm^3), so producing such light materials is challenging. There are few techniques which are able to generate a very low density plasma such as various kind of nanostructures(foams, nanotubes, nanorods,...), gas-jets, aerogels, and others[28]. We will focus on what are called "porous nanostructured carbon layer" or more commonly "foams" which have been studied in [20][23][26][27][29][30][31][32] and many other works. They are made of a collection of carbon nanoparticles aggregating with each other in a foam-like structure as shown in figure 2.4.

In order to produce these materials there are few methods but the one used in the
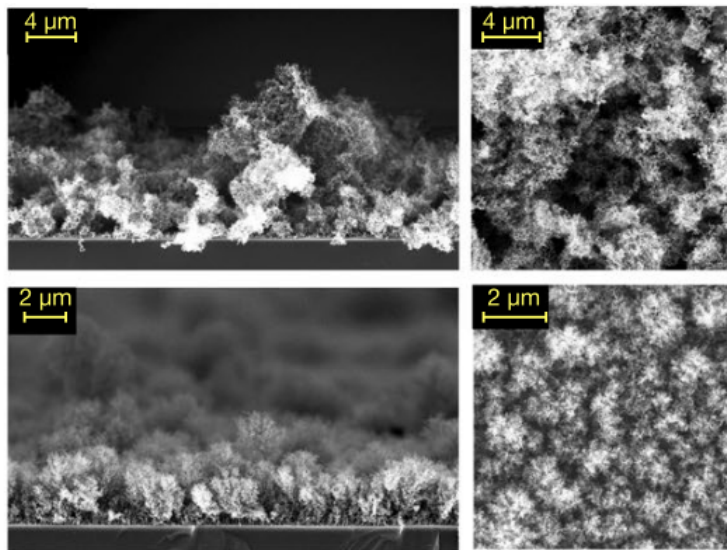
Figure 2.4: SEM images of cross section (left) and top view (right) of an example of porous nanostructured carbon layer.[30]

referenced works is the Pulsed Laser Deposition (PLD) (Figure 2.5). Using a laser in a controlled atmosphere, a graphite target is irradiated and a cloud (or plume) of carbon nanoparticle expands. The nanoparticles start to aggregate with each other and end up deposited onto a solid substrate. The properties of the foam can be controlled changing either the filling gas or its pressure. The aggregation process is complex and its modelling is not trivial, for more details about this topic we will refer to [31][32][33]. The structure results in a porous material in which the total volume occupied by carbon particles is of the order of $\sim 0.1 \div 1.0\%$ of the total volume occupied by the structure. This value is also referred to as "filling factor" and it is a important parameter characterizing the foam properties.

Experimental evidence of increased electron temperature using this kind of targetry has been shown with respect to a bare solid-density foil [22][26][29].

A typical scheme for such a foam-based target is as follows (Figure 2.6):

- Near-critical-density foam layer

- Solid-density substrate

- Pollutants (or "contaminants") layer

The first layer (from the left) is also the first to interact with the laser and is exactly what we expanded upon in this section, tipically few μm thick. Following we find the substrate onto which the foam has grew, usually its thickess is of the order of one (or few) laser wavelength. This part is called different names depending on its actual purpose. This layer is usually referred to as "foil" or "substrate", but fin the frame of this work we will call it "mirror" since we are mostly interested in its ability to reflect a laser pulse minimizing its absorbtion. Finally the last layer is just a few nanometers thick and is made of hydrogenated impurities usually called also "pollutants". These substances (mainly hydrogen) are naturally found on metallic surfaces, and although is indeed possibile to clean them off, they are proven to be advantageous for ion acceleration as we will see in section 2.6.

 This work will not look at optimizing ion acceleration but we decided to keep the
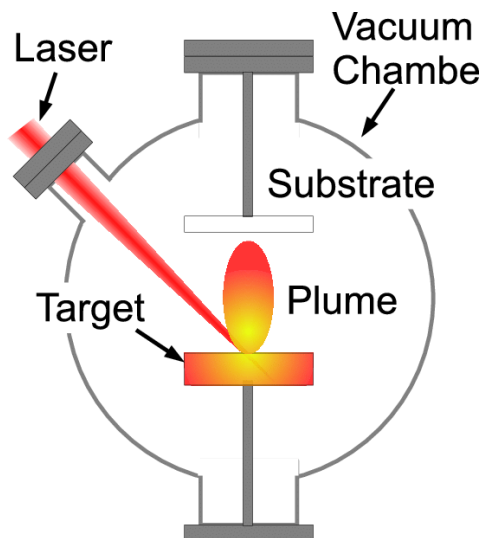
Figure 2.5: Simplified schematics of a typical PLD experimental apparatus.[34]

pollutant layer. The γ-photons production happens mainly in the first two layers so by logic we could erase this last one. Nevertheless we always accounted for it since its computational cost is negligible and helps us having a more realistic target.
It is due to specify that this kind of targets are not the only advanced low-density targetry studied for enhanced photon production. Innovative targetry based on nanotubes has been widely used for various porposes among which synchrotron radiation production [4] and neutron production from D-D fusion [35]. For a more complete treaty on the behaviour of different NCD structures we refer to [30].

2.6   Expanding hot electron plasma and ion acceleration

Since foam-based targets have been shown effective in ion acceleration techniques, we will now give an overview of the main ion acceleration mechanisms.
NCD targets are show to increase the number of hot electrons generated and their temperature. As we will understand better later on in this section, more hot electrons mean more efficient ion acceleration. For these reasons usually NCD targets like the one in fig. 2.6 are used to enhance ion acceleration mechanisms. In the frame of this work we have no interest in producing energetic ions but we want to use these highly
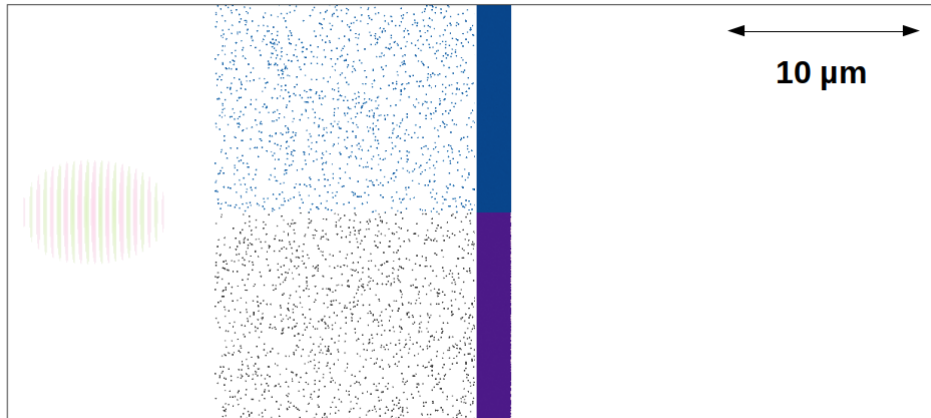
Figure 2.6: Foam-based target scheme. In the top half only the electrons are plotted while in the bottom half onyl ions. The different colors of ions represent different species. More details will be given in section 4.2

energetic electrons to radiate and produce copious amount of photons.
We will start by describing a physical picture of the processes at play starting from the laser arrival at the front surface of the target. Afterward we will discuss the properties of the ions at the back surface of the target, and then we will talk about the processes hapening at its front surface.

2.6.1   Physical picture

Once the laser pulse interacted with the target and the hot electrons are produced, part of them will leave directly the solid material from the front surface while the others will travel through the target itself reaching the backside giving rise to a ion acceleration mechanism called *Target-Normal-Sheath-Acceleration* (TNSA). These electrons are not free to leave the target but if they are energetic enough they can overcome the pulling potential and indeed leave from the back surface. Their respective ions, traditionally metal ions or Carbon in nowadays targetry, are too heavy to follow right away so the electrons accelerated by the laser create a charge separation leading to an electric field, which tends to accelerate any ion in the target. It is clear that if we had light ions ready to be accelerated on the backside the acceleration process would be way more efficient. Is exactly for this reason that usually a really thin ($\sim$ nm) layer of hydrocarburic pollutant is left onto the rear surface [22]. Electrons arriving at the surface need to fight the bulk attraction to leave and this leads to a single electron oscillating back and forth multiple times around the surface before leaving definitively the surface. This mechanism ensures the ionization of the light pollutants which are then ready to be accelerated thanks to their low inertia and favorable position.
While all this is happening the heavy ions which donated the electrons sustain the charge separation. Once lighter ions are accelerated, the field felt by the heavier ions is reduced and so the acceleration of these latter ones is limited.

If a proton beam is needed then impurities and pollutants are the best option, but for some applications it may be needed a beam of heavier ions (i.e. Hadrotherapy). In order to obtain that, we need to suppress the proton acceleration removing any impurities causing the charge separation to be left umbalanced until heavy ions come into play, being accelerated and "absorbing" the energy stored into the sheath field. Figure 2.7 summarizes what just described.
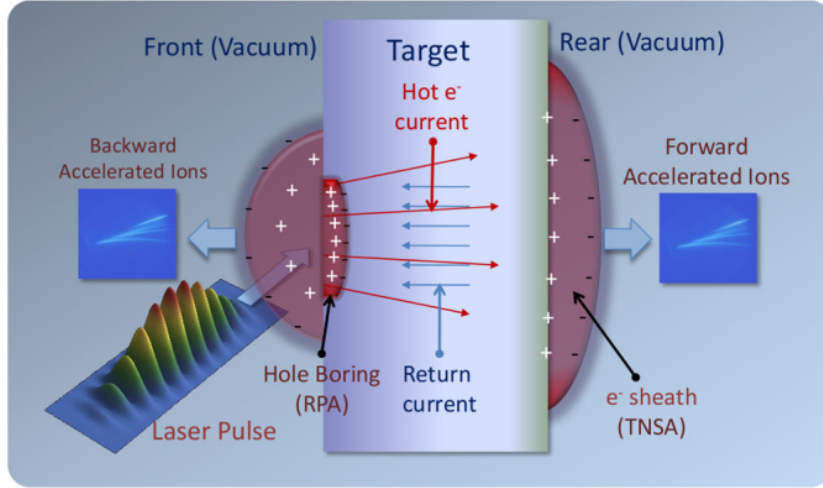
Figure 2.7: Physical picture of the main actors in a traditional (one layer) target. Reprinted from [22]

2.6.2   Particle dynamics on the rear surface: hot plasma expansion

A simple but effective model to describe the dynamics on the back of the target has been proposed in the frame of the expansion of a hot plasma by [22][36][37]. The plasma is treated like a fluid of charged particles with initially hot electrons with a Maxwell-Boltzmann distribution at temperature T_h. We assume the validity of Poisson law at all times t:

$$\epsilon_0 \nabla^2 \phi = e \left(n_e - \sum_s Z_s n_s \right), \tag{2.24}$$

in which ϵ_0 is the vacuum permittivity, ϕ is the electrostatic potential, and the subscript s denotes each specific ions species with atomic number Z_s. For the sake of semplicity we will imagine a 1D system with a plasma made out of only one species of ions. Poisson law then reads:

$$\epsilon_0 \partial_x^2 \phi = e \left(n_e - Z n_i \right). \tag{2.25}$$

The expanding electrons plasma leads to charge separation, which increases the absolute value of the right-hand-side (RHS) of equation (2.25) generating a potential which itself generates a field given by:

$$\boldsymbol{E} = -\nabla \phi. \tag{2.26}$$

Now to describe the ion expansion derived from this field, we use fluid equations which represent respectively mass and momentum conservation:

$$(\partial_t + v_i \partial_x) n_i = n_i \partial_x v_i, \tag{2.27}$$

$$(\partial_t + v_i \partial_x)v_i = -\frac{eZ}{m_i}\partial_x\phi. \tag{2.28}$$

These two equations solved together with Poisson's law would give an analytical solution to the system.

If the plasma is left to expand for a sufficiently long amount of time then its characteristic length of expansion L is much greater then the spatial scale of the electron distribution λ_D defined as in eq.(2.10).

If $L \gg \lambda_D$ then can be shown [36] that LHS of Poisson law becomes very small and thus:

$$0 \approx e(n_e - Zn_i) \rightarrow n_e \approx Zn_i. \tag{2.29}$$

Now, defining the so called "self-similar coordinate" $\xi = x/(c_s t)$ we can rewrite the set of equations which now reads:

$$(v_i - c_s\xi)\partial_\xi n_i = n_i \partial_\xi v_i, \tag{2.30}$$

$$(v_i - c_s\xi)\partial_\xi v_i = -\frac{eZ}{m_i}\partial_\xi\phi, \tag{2.31}$$

with:

$$\omega_{pi} = \sqrt{\frac{e^2 Z n_e}{\epsilon_0 m_i}}, \tag{2.32}$$

$$c_s = \lambda_D \omega_{pi} = \sqrt{\frac{T_h Z}{m_i}}, \tag{2.33}$$

being the ion plasma frequency and the ionic speed of sound respectively.

A solution to this system is found as:

$$n_e = Zn_i = n_e(t=0)\exp\left[-\xi - 1\right], \tag{2.34}$$

$$v_i = c_s(1 + \xi), \tag{2.35}$$

$$\phi = -\frac{T_h}{e}\left(\xi + 1\right). \tag{2.36}$$

This equation gives us a description of a rarefraction wave meaning that the ion density initially $n_i = n_e/Z$ is decreasing as the ions expand into the vacuum. This decrease in density is called "rarefraction" and the corresponding rarefraction wave, being a mechanical perturbation, moves at speed c_s.

At the expansion front quasi-neutrality cannot be ensured so the model fails as we can see in Fig 2.8.

It is now the time to point out that in this model we assumed that we have an infinite supply of electrons at temperature T_h. This can only be achieved by using the hypothesis of a semi-infinite plasma in the direction $x < 0$. If we look at a real system for a long enough time we see that the electrons can actually cool down or simply diffuse away, one of the main reason being the finished interaction with the laser, so the model fails for very long times as well.

One of the main results of this model is that we can get the ion spectrum:

$$\frac{dN}{dv} = n_{io}t\exp\left[-\frac{v}{c_s}\right], \tag{2.37}$$

with n_{io} being the density of ions at time $t = 0$. We can notice how the number of accelerated ions is linear with time and exponentially decreasing in speed, with the
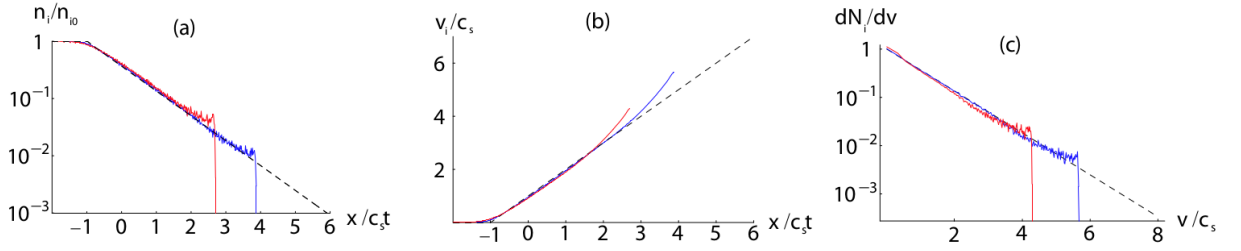
Figure 2.8: a) Self-similar expansion of 1D hot plasma slab. The point $x = 0$ is taken at the plasma boundary fot $t = 0$. b) Average ion velocity. c) The ion velocity distribution normalized to the initial ion density. In red after 10 ions time ($t\omega_{pi} = 10$) and in blue after 20 ions time($t\omega_{pi} = 20$). Reprinted from [37]

same validity points made before.

This model is very useful to describe the rear side of the target after the interaction with the pulse. Moreover, using simple dimensional arguments as done in [20][38] is possible to roughly estimate the maximum ion energy. Let's say that the sheath electric field at the back of the target is:

$$E_{sheath} \sim \frac{T_h}{eL_e}, \tag{2.38}$$

with $L_e \sim \lambda_D$ the length of the protruding electron cloud which is of the order of the Debye length. The temperature can be estimated here with a ponderomotive scaling described in eq. (2.20) which results in $T_e \propto I_0^{0.5} \propto a_0$.

The energy of a test ion acquired in said field is:

$$\epsilon_i \sim ZeE_{sheath}L_e \sim ZT_e. \tag{2.39}$$

Typical experimental values are $a_0 \sim 10^0 \div 10^1$, electron density $n_e \sim 10^{22} \div 10^{23}\mathrm{cm}^{-3}$ ($\sim 10^2 n_c$) and sheath size $L_e \sim \mu$m. These parameters would give us temperatures of the order of few MeVs and sheath field of the order of few MVs. The total energy given to the ion is then of the order of few MeVs per nucleon.

Relating the ion energy to the intensity on target we can find:

$$\epsilon_i \propto P_{laser}^{\frac{1}{2}} \propto I_{laser}^{\frac{1}{2}}, \tag{2.40}$$

with P_{laser} being the laser power and I_{laser} being its corresponding intensity.

In the frame of laser-driven processes, TNSA is the most solid, reliable and effortless way of accelerating ions we have at the moment. Eventhough increasing the intensity of the laser beam will definitely translate into an increased energy for the ions, since it scales like $I^{0.5}$ TNSA might not be the most efficient mechanism to be exploited at ultra-high intensity.

2.6.3 Particle dynamics on the front surface: Radiation Pressure

Electromagnetic waves (EMW) carry momentum which can be transferred to a non-transparent medium (overcritical plasma). With momentum transfer, a force is generated and with it a pressure. This very pressure is what rules the dynamics on the front surface, thus the name of this mechanism is *Radiation Pressure Acceleration*

(RPA).

Assuming a plane wave of frequency ω and intensity I we can write the radiation pressure as [22]:

$$P = (1 + R - T)\frac{I}{c} = (2R + A)\frac{I}{c}, \tag{2.41}$$

with c the speed of light in vacuum and R, T, A the reflective, transmission and absorption coefficients respectively. In general these coefficients are functions of the refractive index $\widetilde{n}$ which is itself function of the EMW frequency, so for a laser pulse we should expect small differences between each coefficient along the spectrum but for the sake of semplicity those differences are neglected. The pressure can be related to the total steady ponderomotive force acting on the particles [22]. As already stated only electrons interact directly with the laser and can get directly accelerated. The pressure would lead electrons to be pushed inward in the surface of the target, piling up, and creating a charge separation that would drag along ions. It is important to address the fact that the ponderomotive force is not a stationary quantity, but leads to oscillations in the electron density. This oscillations are what heat up electrons. Since the ion reaction time is so much longer that the electron's, as far as an ion is concerned it only feels an average force corresponding to the average ponderomotive force over the laser period.

The radiation pressure (RP) pushes the surface inward in the material, deforming it. If the target is thick enough what is observed is only a parabolic deformation of the surface while for very thin targets ($< 1\mu$m) the target as a whole can be pushed along with the radiation. The first regime is called *Hole-Boring* (HB) while the second one is referred to as *Light-Sail-Acceleration* (LSA).

Looking first at the behaviour of a thick target we give a brief description of the HB mechanism.

Putting ourself in the rest frame of the surface we se ions coming towards us moving at velocity $-v_{HB}$, be reflected, and leaving at velocity v_{HB}. The surface recession speed v_{HB} can be computed as shown in [22][39] balancing the momentum flow of the ions with the momentum of the EMW reflected at the surface.

$$\frac{I}{c}\frac{1 - \frac{v_{HB}}{c}}{1 + \frac{v_{HB}}{c}} = n_i m_i \gamma_{HB}^2 v_{HB}^2. \tag{2.42}$$

Solving for v_{HB} we find:

$$v_{BH} = \frac{\Pi^{\frac{1}{2}}}{1 + \Pi^{\frac{1}{2}}}c, \tag{2.43}$$

with:

$$\Pi = \frac{I}{m_i n_i c^3} = \frac{Z n_c m_e}{A n_e m_p}a_0^2. \tag{2.44}$$

The resulting ion energy in the laboratory frame can be computed as:

$$\epsilon_i = 2 m_i c^2 \frac{\Pi}{1 + \Pi^{\frac{1}{2}}}. \tag{2.45}$$

This process produces ions at v_{HB} until the electron sharpening becomes unstable and breaks down. If the laser pulse is still interacting with the surface then the process starts all over producing another bunch of ions at the same velocity. This will go on until the pulse stops to interact with the target.

If the target is thin enough the deformation of the surface can reach the other side and section of the target is physically detached from the rest. The electron and ion

bunch is now carried by the laser pulse much like a sail is carried by the wind, giving the name *Light Sail Acceleration* (LSA) (fig.2.9).

At this point the laser will continue accelerating the bunch until it is completely reflected. This process appears to be more efficient than both HB and TNSA but requires special targets and ultra-high-intensity lasers. In particular the thickness required for a LSA target would be of few tens of nm for intensity of the order of 10^{20}Wcm^{-2}. The main advantage of this regime would be an ion energy scaling proportionally to the laser intensity in the ultrarelativistic regime. This would mean that for ultra-high intensities we may choose LSA over TNSA or HB.

In the frame of this work, although at ultrarelativistic intensity, we used pretty
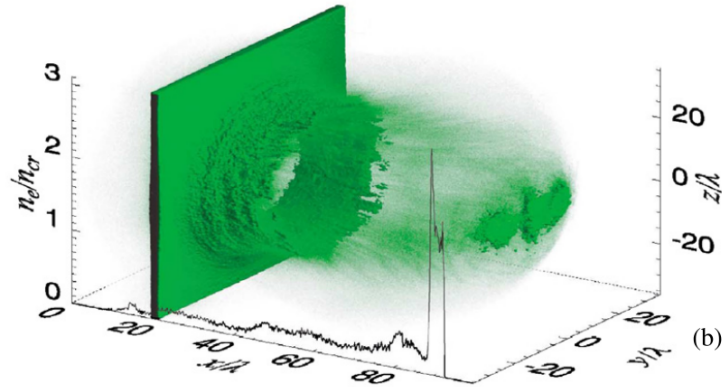
Figure 2.9: Ion accelerated front in light sail regime obtained through PIC simulation.[38]

thick foam-based targets which are specialized in enhancing absorption and suppress reflection, LSA is then never observed. For more thorough discussion on RPA driven mechanisms we refer to [38][39][40].

Chapter 3

The Particle-In-Cell code Smilei

In the previous chapters we discussed the main physical processes underlying the generation of photons driven by high intensity lasers. In chapter 1 we focused on the main mechanisms for the conversion of high energy electrons into photons, while chapter 2 was devoted to the generation of high energy electrons driven by superintense lasers. A reliable theoretical description of such complex system can be obtained only by means of dedicated numerical simulations. In this thesis we ran simulations of (almost) realistic experimental set-ups in order to enstablish the magnitude of the photon production achievable by a UHI laser facility such as Apollon. In this work we used Particle-In-Cell (PIC) simulations, which are the most-established tool to study kinetic effects in the field of laser-plasma interaction. In particular we employed the PIC code *Smilei*[3] which is developed here at *Ecole Polytechnique* by the *Maison de la simulation*. In this chapter we explain how a PIC code works, focusing especially on Smilei.

PIC codes are *kinetic codes*, meaning that they are based on an approximate resolution of the system made of Vlasov equation and Maxwell equations. First we will give an introduction on the kinetic approach, then we will discuss the core of a PIC code: the PIC algorithm.

Finally, a brief explanation of the main physics modules we used which are not included in a standard PIC code, such as ionization mechanisms, collisional processes, and photon production.

3.1   Kinetic description

3.1.1   Kinetic equations

In order to achieve a complete kinetic description of a system of N particles, the set of all positions $\boldsymbol{x}_k$ and momenta $\boldsymbol{p}_k$ of each particle is needed at all times.

The distribution function f_{Ms} describes the evolution in time of the position of all the particles of the species s in phase space $(\boldsymbol{x}, \boldsymbol{p})$ and is defined as follows:

$$f_{Ms}(\boldsymbol{x}, \boldsymbol{p}, t) = \sum_k \delta(\boldsymbol{x} - \boldsymbol{x}_k(t)) \delta(\boldsymbol{p} - \boldsymbol{p}_k(t)), \tag{3.1}$$

in which the subscript k refers to the single k-th particle of the system, while M means that we are looking at the single particles and thus we are adopting a "microscopic" approach. The function δ is the Dirac-delta and is defined as:

$$\delta(w) = \begin{cases} \infty & \text{if } w = 0, \\ 0 & otherwise, \end{cases} \tag{3.2}$$

and

$$\int_{-\infty}^{+\infty} \delta(w)dw = 1. \tag{3.3}$$

We can then define a charge density ρ_M and a current density $\boldsymbol{J}_M$ by suitably averaging the distribution function in the momentum space:

$$\rho_M(\boldsymbol{x}, t) = \sum_s q_s \int f_{Ms} d\boldsymbol{p}, \tag{3.4}$$

$$\boldsymbol{J}_M(\boldsymbol{x}, t) = \sum_s q_s \int \boldsymbol{v} f_{Ms} d\boldsymbol{p}. \tag{3.5}$$

Assuming that the total number of particles in the system does not change in time [4][7] :

$$\frac{df_{Ms}(\boldsymbol{x}, \boldsymbol{p}, t)}{dt} = 0, \tag{3.6}$$

and assuming that every particle experiences the Lorentz force only, we can write what is known as Klimontovich equation [4][7] :

$$\partial_t f_{Ms} + \boldsymbol{v} \cdot \nabla f_{Ms} + \frac{q_s}{m_s} (\boldsymbol{E}_M + \boldsymbol{v} \times \boldsymbol{B}_M) \cdot \nabla_{\boldsymbol{p}} f_{Ms} = 0. \tag{3.7}$$

This equation once solved would give us all the information about all particles of the system. Unfortunately, the combination of the incredibly large amount of particles present in typical systems ($\sim 10^{10} \div 10^{20}$) and the limited resolution of nowadays numerical codes ($> 10^{-10}$m), makes it impossible to have an accurate solution for each particle in the system. We can simplify the system writing each microscopic quantity as the sum of an averaged (or collective) quantity and a microscopic fluctuation denoted by the symbol δ :

$$f_{Ms} = f_s + \delta f_s, \tag{3.8}$$

$$\boldsymbol{E}_M = \boldsymbol{E} + \delta \boldsymbol{E}, \tag{3.9}$$

$$\boldsymbol{B}_M = \boldsymbol{B} + \delta \boldsymbol{B}, \tag{3.10}$$

$$\boldsymbol{F}_L = q(\boldsymbol{E} + \boldsymbol{v} \times \boldsymbol{B}). \tag{3.11}$$

By applying this concept and averaging ($\langle \rangle$) eq.(3.7) we can find [4][7] :

$$\partial_t f_{Ms} + \boldsymbol{v} \cdot \nabla f_{Ms} + \frac{\boldsymbol{F}_L}{m_s} \cdot \nabla_{\boldsymbol{p}} f_{Ms} = -\frac{1}{m_s} \langle \delta \boldsymbol{F}_L \cdot \nabla_{\boldsymbol{p}} f_{Ms} \rangle. \tag{3.12}$$

The left hand side (LHS) arise from the collective properties of the plasma while the right hand side (RHS) is due to the microscopic (or collisonal) behaviour. Collisional effects are born from the Coulomb interaction of the single charges with one another. The colder the plasma, the more important the collisional behaviours become. As a useful rule of thumb, a plasma can be described as collisionless if [4][7] :

$$\Lambda = n_e \lambda_D^3 \gg 1. \tag{3.13}$$

Where Λ is called "plasma parameter", n_e is the number density of the electrons and λ_D is the Debye length(defined in eq.2.10). In the frame of this work we will consider mostly strongly relativistic electrons with temperatures of the order of or greater than the electron rest energy (for which $\lambda_D \sim 10^{-2}$cm) and densities of the order of or greater thna the critical densities $n_c \approx 1.7 \times 10^{21}$cm^{-3}. That would yield to a plasma parameter $\Lambda \sim 10^{15} \gg 1$, well inside the hypothesis of negligibility of collisional behaviour unless otherwise specified.

Neglecting the RHS of eq. (3.12) we get another famous equation in plasma physics known as Vlasov equation which reads [4][7] :

$$\partial_t f_s + \boldsymbol{v} \cdot \nabla f_s + \frac{\boldsymbol{F}_L}{m_s} \cdot \nabla_{\boldsymbol{p}} f_s = 0. \tag{3.14}$$

3.1.2   Kinetic description of radiation reaction

As we discussed in section (1.1.3) radiation reaction enters the particle equations of motion as:

$$\frac{d\boldsymbol{p}}{dt} = \boldsymbol{F}_L + \boldsymbol{F}_{RR}, \tag{3.15}$$

in which the first term on the RHS is the Lorentz force and the second is the feedback force due to the photon emission. Following the steps in [7] we can then write an equation for the electron distribution function that reads:

$$\partial_t f_s + \boldsymbol{v} \cdot \nabla f_s + \frac{1}{m_s} \nabla_{\boldsymbol{p}} \cdot \left(\boldsymbol{F}_L + \boldsymbol{F}_{RR} \right) f_s = 0, \tag{3.16}$$

which is really similar to Vlasov equation. Let's notice that if $\nabla_{\boldsymbol{p}} \cdot \boldsymbol{F} = 0$ then it means that the generic force $\boldsymbol{F}$ does not change the volume in phase-space of the distribution function and because of that we can say that $\boldsymbol{F}$ does not change the total energy stored in the particles [7]. For $\boldsymbol{F_L}$ this is true, as we saw in section 1.1.1 an electron under the effect of the only Lorentz force will start rotating at constant angular velocity ω_L and constant radius r_L conserving its total energy. $\boldsymbol{F}_{RR}$ instead implies a trasfer of energy from electrons to photons thus decreasing the total energy stored in the particles, reducing the phase-space volume of f_s (or f_e since the only radiating particles in this work are electrons). This means that in this case $\nabla_{\boldsymbol{p}} \cdot \boldsymbol{F}_{RR} > 0$ [7]. Expanding then the last term of eq. (3.16) we can write a Vlasov equation accounting for classical radiation reaction [4][7] :

$$\partial_t f_s + \boldsymbol{v} \cdot \nabla f_s + \frac{1}{m_s} \left(\boldsymbol{F}_L + \boldsymbol{F}_{RR} \right) \cdot \nabla_{\boldsymbol{p}} f_s = -f_s \nabla_{\boldsymbol{p}} \cdot \boldsymbol{F}_{RR}. \tag{3.17}$$

In the next section we will see how the flow of a PIC code in its main parts addresses the problem of solving this equation coupled with the Maxwell systems.

3.2   PIC algorithm

Particle-in-cell (PIC) codes approximately solve the system of equations made of Vlasov (eq. 3.18) equation and Maxwell equations (in SI units in this work) (eqs. (3.19)-(3.22)) for a collection of charged particles.

$$\partial_t f_s + \boldsymbol{v} \cdot \nabla f_s + q_s \left(\boldsymbol{E} + \boldsymbol{v} \times \boldsymbol{B} \right) \cdot \nabla_{\boldsymbol{p}} f_s = 0, \tag{3.18}$$

$$\nabla \cdot \boldsymbol{E} = \frac{\rho}{\epsilon_0}, \tag{3.19}$$

$$\nabla \cdot \boldsymbol{B} = 0, \tag{3.20}$$

$$\nabla \times \boldsymbol{E} = -\partial_t \boldsymbol{B}, \tag{3.21}$$

$$\nabla \times \boldsymbol{B} = \mu_0 \boldsymbol{J} + \frac{1}{c^2} \partial_t \boldsymbol{E}, \tag{3.22}$$

with $f_s = f_s(\boldsymbol{x}, \boldsymbol{p}, t)$ is the distribution function in phase space $(\boldsymbol{x}, \boldsymbol{p})$ and in time. The subscript s denotes the specific species characterized by a charge q_s and a mass m_s. The electromagnetic fields generated by the charges are computed from the charge density ρ and the current density in the plasma $\boldsymbol{J}$, and of these quantities can be computed starting from f_s. We can notice that the number density of particles of species s and their flux are respectively:

$$n_s(\boldsymbol{x}, t) = \int f_s d\boldsymbol{p}, \tag{3.23}$$

$$\boldsymbol{\phi}_s(\boldsymbol{x}, t) = \int \boldsymbol{v} f_s d\boldsymbol{p}. \tag{3.24}$$

The total charge density and current density are then defined as:

$$\rho(\boldsymbol{x}, t) = \sum_s q_s \int f_s d\boldsymbol{p}, \tag{3.25}$$

$$\boldsymbol{J}(\boldsymbol{x}, t) = \sum_s q_s \int \boldsymbol{v} f_s d\boldsymbol{p}. \tag{3.26}$$

It is clear that this system is self-consistent and every equation has feedback on the others so in general these equations cannot be solved separately but need to be satisfied simultaneously.

Let's emphasise that the performance of nowadays supercomputers and softwares does not allows us to describe the evolution of the motion of every fondamental particle, so the PIC algorithm uses what are called *macroparticles* which are fictitious particles representing each one a group of real particles. PIC codes approximately solve the system above, solving instead the system made of Maxwell equations and Newton equation of motion for each *macroparticle*. In order to do so, the configuration space is divided into regions of size Δx^m (with "m" the dimensionality of the system) called *cells* and time into a sequence of discrete jumps Δt called *timesteps*, defining space and time not as a continous coordinates anymore, but as discretized ones. This way, each coordinate in space along any diurection, i.e. x, will be a multiple of the cell size in that direction, i.e. Δx. Another quantity which is very important is what is called "space resolution" or $1/\Delta x$. In the frame of this this line of research it is usually given in "points per λ_0", referring to how many cells can be fit into a laser wavelength. Nonetheless in this work we wanted to keep the focus on the experimental reality, so we will always give Δx in μm or in nm, and so the resolution in "points per μm".

The discretization process is pretty straightforward and is based on the approximation of the derivatives with finite differences as follows:

$$\frac{\partial f}{\partial x} \to \frac{f_{i+1} - f_i}{\Delta x}, \tag{3.27}$$

$$\frac{\partial f}{\partial t} \to \frac{f_{n+1} - f_n}{\Delta t}, \tag{3.28}$$

in which i denotes the cell number in the $x-direction$ and n the timestep at which the values are taken. And of course integrals are now finite sums over a specific coordinate:

$$\int f dt \to \sum_n f_n \Delta t. \tag{3.29}$$

In order to find a solution each eqaution is solved iteratively in what is called the "PIC loop" structured as represented in figure 3.1.

Tipical resolutions for works similar to this thesis are on the order of $10^{-8} \div 10^{-9} m$
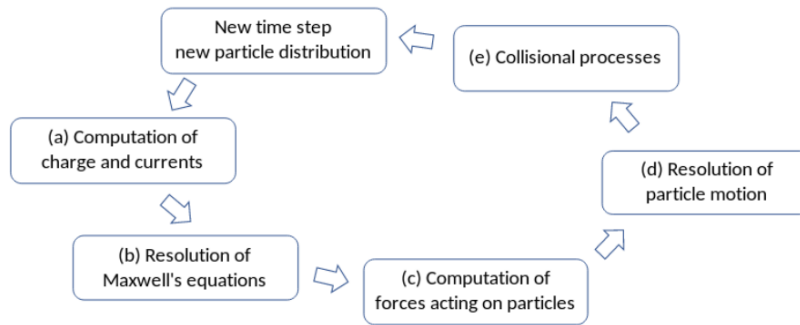
Figure 3.1: Schematics of the PIC loop. [4]

which is far from enough to describe the motion of an electron around a nucleous, and, even if it were possible to reach adequate resolutions, questions on the physical meaning of said description would arise.

The PIC approach is enough to describe processes with characteristic length greater than the resolution, for this reason collision-like processes are usually taken into account by implementing tailored Monte Carlo modules and tables.

Lastly, it is really important to point out the difference between the term *macroparticle* and *nanoparticle* (from sec.2.5). A *macroparticle* has been described in this chapter and is a numerical escamotage in order to simulate the behaviour of several real particles, which would be otherwise an impossible task. A *macroparticle* is just a numerical tool, is not a physical characteristic of the system, even a perfectly uniform plasma would still be divided into *macroparticles*. A *nanoparticle* is instead a physical characteristic of a system, such as foams, which have a peculiar structure. A *nanoparticle* is a collection of atoms aggregated together which is roughly as dense as a solid $(10^2 \div 10^3 n_c)$. The structure of a foam as seen in section 2.5 is roughly a collection of *nanoparticles*, for which the average density is two or three orders of magnitude lower than the solid density. From this should be clear that *macroparticle* and *nanoparticle* are two very distinct concepts and the reader should pay attention not to confuse them.

3.3 Mesh and interpolation method

Each time the code needs to compute on a grid point any particle quantity, and vice versa, an interpolation is required. This process is not trivial and here we will

summarize how is generally done in PIC codes.

For the sake of semplicity we will look at the 1D representation of a more general 3D mesh, but all the concepts are easily generalized to higher dimensionalities. Let's appoint the fact that all the quantities realative to the particles (ρ and $\boldsymbol{J}$) are computed at the particle coordinates (x_k) while the fields are calculated at the mesh points (X_i). In order for the code to solve the equations we need all the quantities evaluated at the same point in space, so we need to interpolate in order to find the data we are missing. Following the core PIC loop as delineated in the previous section, we project currents and charge densities onto the mesh points. This is necessary in order to solve Maxwell equations and get the updated fields. Now what is needed is to interpolate the newly computed fields onto the particles positions in order to compute the Lorentz force acting on each one of them.

The interpolation is always made using a "shape function" S as described below:

$$\rho(X_i) = \frac{1}{\Delta x^m} \sum_s \sum_k q_s S(X_i - x_k), \tag{3.30}$$

$$\boldsymbol{J}(X_i) = \frac{1}{\Delta x^m} \sum_s \sum_k q_s v_k S(X_i - x_k), \tag{3.31}$$

where m is the dimensionality of the discretized space($m = 1$ in 1D), and denoting the Heaviside function $H(w)$ with $w = x/\Delta x$:

$$H(w) = \begin{cases} 1 & \text{if } w \geq 0 \\ 0 & otherwise. \end{cases} \tag{3.32}$$

We can deifne the shape function of the order 0 as:

$$S^0(w) = H\left(w + \frac{1}{2}\right) H\left(w - \frac{1}{2}\right), \tag{3.33}$$

$$S^0(w) = \begin{cases} 1 & \text{if } -\frac{1}{2} < w < \frac{1}{2} \\ 0 & otherwise. \end{cases} \tag{3.34}$$

In the way described in [4] we can derive the shape functions for higher orders of approximation:

$$S^1(w) = \begin{cases} w+1 & \text{if } -1 \leq w \leq 0 \\ 1-w & \text{if } 0 \leq w \leq 1 \\ 0 & otherwise, \end{cases} \tag{3.35}$$

$$S^2(w) = \begin{cases} \frac{3}{4} - |w|^2 & \text{if } |w| \leq \frac{1}{2} \\ \frac{1}{2}\left(\frac{3}{2} - |w|\right)^2 & \text{if } \frac{1}{2} \leq |w| \leq \frac{3}{2} \\ 0 & otherwise. \end{cases} \tag{3.36}$$

Is important to point out now that discontinuities in the value of S or in its first derivative are detrimental from the point of view of numerical oscillation since it has been shown that they enhance numerical noise [4]. For this reason commonly used in nowadays PIC codes are order of interpolation 2, 3, 4.
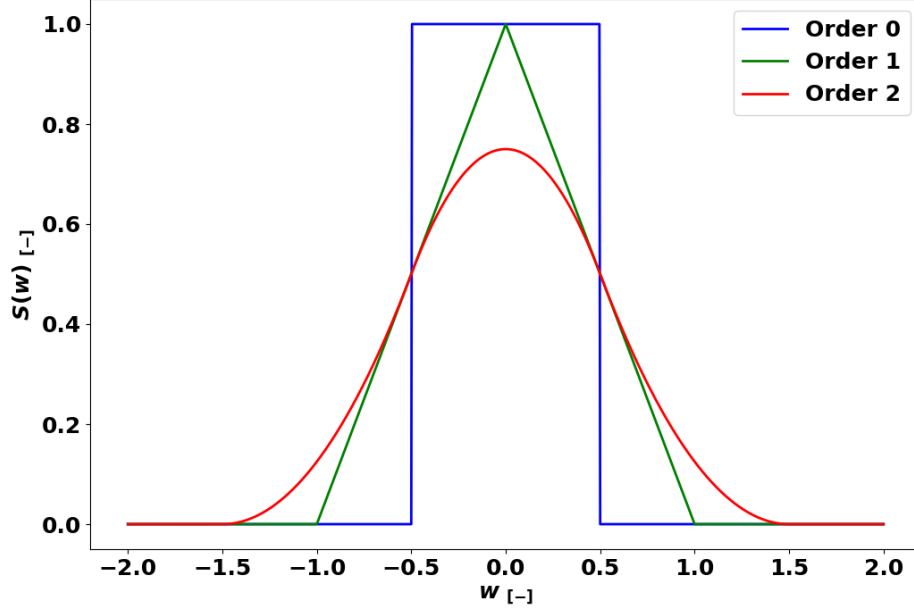
Figure 3.2: Plot of the shape functions for order 0,1 and 2. It is preferable to use smooth functions with no discontinuities, so modern PIC codes use order of 2 and above.

3.4 Order reduction

Before describing the solver itself and its discretization it is worth highlighting how solving Maxwell equations (eqs.(3.19)-(3.22)) can be reduced to solve only Faraday law, Ampere law and the conservation of charge given that Maxwell-Gauss laws are satisfied for $t = 0$. Assuming:

$$\nabla \cdot \boldsymbol{B}(t = 0) = 0, \tag{3.37}$$

and

$$\epsilon_0 \nabla \cdot \boldsymbol{E}(t = 0) - \rho(t = 0) = 0. \tag{3.38}$$

We can apply the divergence to faraday's and Ampere's law leading to:

$$\nabla \cdot \nabla \times \boldsymbol{E}(t) = -\partial_t \nabla \cdot \boldsymbol{B}(t), \tag{3.39}$$

and

$$\nabla \cdot \nabla \times \boldsymbol{B}(t) = \mu_0 \nabla \cdot \boldsymbol{J}(t) + \mu_0 \epsilon_0 \partial_t \nabla \cdot \boldsymbol{E}(t). \tag{3.40}$$

The first term of these equations is identically zero so we can rewrite the system as:

$$\partial_t \nabla \cdot \boldsymbol{B}(t) = 0, \tag{3.41}$$

and

$$\nabla \cdot \boldsymbol{J}(t) + \epsilon_0 \partial_t \nabla \cdot \boldsymbol{E}(t) = 0. \tag{3.42}$$

From eq.(3.41) we can see that the divergence of the magnetic field would be a constant in time, so if it is equal to zero at one time then it will remain zero during all the considered time interval.

In eq. (3.42) we will plug Gauss theorem to get:

$$\nabla \cdot \boldsymbol{J}(t) + \partial_t \rho(t) = 0, \tag{3.43}$$

which is exactly the expression for the charge conservation valid for each time t considered. Thanks to this reasoning, the complexity of the system of equations to be solved has been reduced by two, with the removed equations solved only at the beginning of the simulation, so only for one timestep.

Ensuring charge conservation is not as trivial as it sounds and a specific algorithm has been implemented in some PIC codes, among which Smilei, that grants the coherence between charge and currents throughout the simulation [41]. This algorithm will be explained in section 3.7.

3.5   Solving Maxwell's equation: Yee solver

We will give an introduction to one of the most popular Maxwell solver for PIC codes which is also used in Smilei: the "Yee solver". We will only go through its main features explicitly describing its discretization but we will not discuss its effectiveness or efficiency, for a more thorough reading we will refer to the original work [42] or to [4].

Figure 3.3 shows the spatial discretization, more precisely what is shown is the diagram of a single cell and the position in which the quantities are evaluated in the algorithm. The Yee solver exploits a "staggered grid" and a "leap-frog" scheme. The former means that different quantities are evaluated on different grids relatively shifted with respect to one another. This approach is useful because allows us to compute derivatives in a simpler and more stable way while the main drawback is that it is limited to a cubic cell geometry [4]. Generally PIC codes focus more on producing stable results activating as many physical processes as possible rather than to make exotic cell geometries available. In general not all numerical solvers use staggered grids, for example in most commercial CFD codes irregular or self-adaptive grids are a more suitable choice.

Leap-frog means that coupled quantities (e.g. E and B) are not computed at the
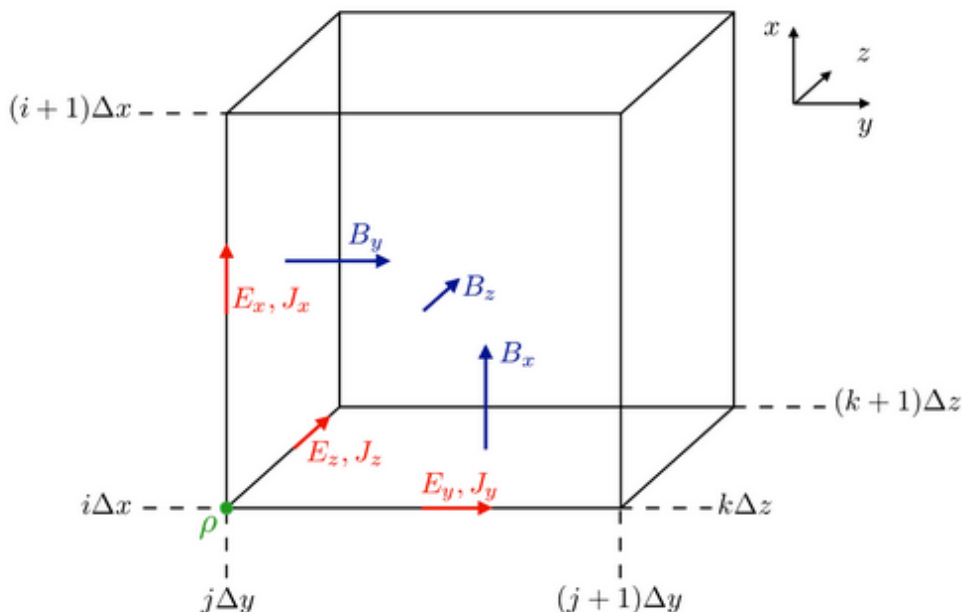
Figure 3.3: Figure rapresenting the discretization space and the place where the quantities are computed.[43]

same timestep, which can be seen as expoilting a staggered grid in time which has the same pros and cons of a staggered grid in space. This approach is particularly useful if one quantity or its space derivatives are functions of the time derivatives of the other. For example $\partial_t(\boldsymbol{B})^n$ which is the time derivative at the timestep n is obtained by the difference of the $\boldsymbol{B}$ field at timesteps $n + 1/2$ and $n - 1/2$. In Maxwell equations the partial time derivative of the magnetic field is related to the space derivatives of the electric field which is computed at timestep n.

Using the above discretization method we can then rewrite Faraday law that reads:

$$\frac{(B_x)^{n+\frac{1}{2}}_{i,j+\frac{1}{2},k+\frac{1}{2}} - (B_x)^{n-\frac{1}{2}}_{i,j+\frac{1}{2},k+\frac{1}{2}}}{\Delta t} = \frac{(E_y)^n_{i,j+\frac{1}{2},k+1} - (E_y)^n_{i,j+\frac{1}{2},k}}{\Delta z} - \frac{(E_z)^n_{i,j+1,k+\frac{1}{2}} - (E_z)^n_{i,j,k+\frac{1}{2}}}{\Delta y},$$
(3.44)

$$\frac{(B_y)^{n+\frac{1}{2}}_{i+\frac{1}{2},j,k+\frac{1}{2}} - (B_y)^{n-\frac{1}{2}}_{i+\frac{1}{2},j,k+\frac{1}{2}}}{\Delta t} = \frac{(E_z)^n_{i+1,j,k+\frac{1}{2}} - (E_z)^n_{i,j,k+\frac{1}{2}}}{\Delta x} - \frac{(E_x)^n_{i+\frac{1}{2},j,k+1} - (E_x)^n_{i+\frac{1}{2},j,k}}{\Delta z},$$
(3.45)

$$\frac{(B_z)^{n+\frac{1}{2}}_{i+\frac{1}{2},j+\frac{1}{2},k} - (B_z)^{n-\frac{1}{2}}_{i+\frac{1}{2},j+\frac{1}{2},k}}{\Delta t} = \frac{(E_x)^n_{i+\frac{1}{2},j+1,k} - (E_x)^n_{i+\frac{1}{2},j,k}}{\Delta y} - \frac{(E_y)^n_{i+1,j+\frac{1}{2},k} - (E_y)^n_{i,j+\frac{1}{2},k}}{\Delta x}.$$
(3.46)

Keep going with the discretization method used until now we can also rewrite Ampere law in its discretized form:

$$\frac{(E_x)^{n+1}_{i+\frac{1}{2},j,k} - (E_x)^n_{i+\frac{1}{2},j,k}}{c^2 \Delta t} =$$
$$\frac{(B_z)^{n+\frac{1}{2}}_{i+\frac{1}{2},j+\frac{1}{2},k} - (B_z)^{n+\frac{1}{2}}_{i+\frac{1}{2},j-\frac{1}{2},k}}{\Delta y} - \frac{(B_y)^{n+\frac{1}{2}}_{i+\frac{1}{2},j,k+\frac{1}{2}} - (B_y)^{n+\frac{1}{2}}_{i+\frac{1}{2},j,k-\frac{1}{2}}}{\Delta z} - \mu_0 (J_x)^{n+\frac{1}{2}}_{i+\frac{1}{2},j,k},$$
(3.47)

$$\frac{(E_y)^{n+1}_{i,j+\frac{1}{2},k} - (E_y)^n_{i,j+\frac{1}{2},k}}{c^2 \Delta t} =$$
$$\frac{(B_x)^{n+\frac{1}{2}}_{i,j+\frac{1}{2},k+\frac{1}{2}} - (B_x)^{n+\frac{1}{2}}_{i,j-\frac{1}{2},k-\frac{1}{2}}}{\Delta z} - \frac{(B_z)^{n+\frac{1}{2}}_{i+\frac{1}{2},j+\frac{1}{2},k} - (B_z)^{n+\frac{1}{2}}_{i-\frac{1}{2},j+\frac{1}{2},k}}{\Delta x} - \mu_0 (J_y)^{n+\frac{1}{2}}_{i,j+\frac{1}{2},k},$$
(3.48)

$$\frac{(E_z)^{n+1}_{i,j,k+\frac{1}{2}} - (E_z)^n_{i,j,k+\frac{1}{2}}}{c^2 \Delta t} =$$
$$\frac{(B_y)^{n+\frac{1}{2}}_{i+\frac{1}{2},j,k+\frac{1}{2}} - (B_y)^{n+\frac{1}{2}}_{i-\frac{1}{2},j,k+\frac{1}{2}}}{\Delta x} - \frac{(B_x)^{n+\frac{1}{2}}_{i,j+\frac{1}{2},k+\frac{1}{2}} - (B_x)^{n+\frac{1}{2}}_{i,j-\frac{1}{2},k+\frac{1}{2}}}{\Delta y} - \mu_0 (J_z)^{n+\frac{1}{2}}_{i,j,k+\frac{1}{2}}.$$
(3.49)

The code will now solve this system of discretized equations for each point on the grid, giving us the complete distribution of fields inside the simulation domain (also called "simulation box") for a given timestep.

The Yee solver is an "explicit" solver, which means that each equation is solved only once for timestep, since in each equation only one unknown quantity is present

at once. This approach is different from an "implicit" one, for which in general is required the numerical solution of a linear system of equations.

For explicit solvers, and in particular for the Yee solver the resolution in time is not independent from the one in space because it can be shown that the following condition, i.e. the CFL condition,

$$\left(\frac{1}{\Delta x^2} + \frac{1}{\Delta y^2} + \frac{1}{\Delta z^2}\right)(c\Delta t)^2 \leq 1. \tag{3.50}$$

must be satisfied in order to avoid any numerical instability [4]. This condition is meant to prevent any kind of information to travel too much distance between timesteps and causing divergence in the solver. This condition practically corresponds to avoid letting a particle travelling of more than one cell during any timestep. In Smilei the recommanded timestep is 0.95 of the CFL limit.

It is worthy to point out now that this method of computing derivatives as differences between the two closest adjacent points which have the same relative weight is often called *centered method* or *centered scheme*. This method implies that the flow of information in a specific region of space is not strongly directional and can propagates in the same way in all direction. For simulations based on electromagnetic interaction this is true, since the electromagnetic information in principle can travel in all directions at fixed velocity c. This characteristic isotropy in information propagation is also typical of diffusion-like problems like heat conduction.

3.6   Newton solver: Boris pusher

Now that all fields are computed it is time to compute their effects on the charged particles in the box. What needs to be solved are Newton equations and since in general particles move at velocities comparable to c, relativistic Newton equations are needed. The algorithm that solves this system of equations related to the particles motion is often called "pusher" since it is responsible for appropriately "pushing" the particles. One of the most common choices which is also implemented in Smilei is called "Boris pusher" [44].

We follow the steps from [4][7] and start by writing down the equations of motion:

$$d_t\boldsymbol{x} = \boldsymbol{v}, \tag{3.51}$$

$$d_t\boldsymbol{p} = q_s\left(\boldsymbol{E} + \boldsymbol{v} \times \boldsymbol{B}\right), \tag{3.52}$$

in which $\boldsymbol{p} = \gamma m\boldsymbol{v}$ is the relativistic momentum of the particle and we can recognize Lorentz force in the right hand side of eq. (3.52). Discretizing eq.(3.51) we get:

$$\boldsymbol{x}^{n+1} = \boldsymbol{x}^n + \frac{\boldsymbol{p}^{n+\frac{1}{2}}}{m_s\gamma^{n+\frac{1}{2}}}\Delta t. \tag{3.53}$$

In order to discretize eq. (3.52) we need to use the Lorentz force to transform $\boldsymbol{p}^{n-\frac{1}{2}}$ in $\boldsymbol{p}^{n+\frac{1}{2}}$. This is not trivial since both the electric and magnetic fields are competing to accelerate the particle but with different effects. The magnetic field bends the trajectory of the particle with a magnitude related to the particle's velocity that is being modified by the electric field. The Boris pusher does this in three steps exploiting two intermediate momenta $\boldsymbol{p}^-$ and $\boldsymbol{p}^+$:

1. Accelerate particles with $\boldsymbol{E}^n$ for half timestep from $\boldsymbol{p}^{n-\frac{1}{2}}$ to $\boldsymbol{p}^-$

2. Rotate the particles momentum with $\boldsymbol{B}^n$ from $\boldsymbol{p}^-$ to $\boldsymbol{p}^+$

3. Accelerate particles with $\boldsymbol{E}^n$ for half timestep from $\boldsymbol{p}^+$ to $\boldsymbol{p}^{n+\frac{1}{2}}$

The first and last step are obviously more similar to each other and read:

$$\boldsymbol{p}^- = \boldsymbol{p}^{n-\frac{1}{2}} + \frac{q_s \boldsymbol{E}^n}{m_s} \frac{\Delta t}{2}, \tag{3.54}$$

$$\boldsymbol{p}^{n+\frac{1}{2}} = \boldsymbol{p}^+ + \frac{q_s \boldsymbol{E}^n}{m_s} \frac{\Delta t}{2}, \tag{3.55}$$

The second step instead involves a normalized magnetic field $\boldsymbol{b} = q_s \Delta t \boldsymbol{B}^n / (2 m_s)$ and consists in a pure rotation:

$$\boldsymbol{p}^+ = \frac{2}{1+b^2} \begin{bmatrix} -b_y^2 - b_z^2 & b_z + b_x b_y & -b_y + b_x b_z \\ -b_z + b_x b_y & -b_x^2 - b_z^2 & b_x + b_y b_z \\ b_y + b_x b_z & -b_x + b_y b_z & -b_x^2 - b_y^2 \end{bmatrix} \boldsymbol{p}^-. \tag{3.56}$$

The Boris pusher may seem a simplistic way to approximate the motion of a particle inside an electromagnetic field but has actually given really good results for what PIC codes are concerned, so that it is one of the most commonly used.

3.7 Esirkepov correction for charge conservation

As already discussed in section 3.4, the Maxwell solver is required to solve only Ampere and Farady law in order to compute the fields in all space at all times given that Poisson condition is guaranteed at $t = 0$ and charge continuity equation is ensure at all times. PIC codes therefore require charge conservation but the definitions of charge and currents of eqs. (3.30) (3.31) make it not trivial to actually ensure it. We will now summarize a method proposed in [41] which is nowadays considered the most reliable algorithm to address the problem of charge conservation.
Recalling the definition given of ρ in eq. (3.30) and assuming linearity between the terms we can focus on the single macroparticle contribution to charge density and afterwards sum all contribution together. We then define:

$$\rho_p(\boldsymbol{X}) = q_p S(\boldsymbol{X} - \boldsymbol{x}_p), \tag{3.57}$$

in which we called $\boldsymbol{X}$ the coordinate of the grid centers and $\boldsymbol{x}$ the coordinates of the single macroparticle p. We can also define what are called *density decomposition vectors* in the following way:

$$\boldsymbol{W}_{i,j,k} = -\nabla^+ \cdot \boldsymbol{J}_{i,j,k} \frac{\Delta t}{q_p}, \tag{3.58}$$

with the operator ∇^+ defined as:

$$\nabla^+ f_{i,j,k} = \left(\frac{f_{i+1,j,k} - f_{i,j,k}}{\Delta x}, \frac{f_{i,j+1,k} - f_{i,j,k}}{\Delta y}, \frac{f_{i,j,k+1} - f_{i,j,k}}{\Delta z} \right). \tag{3.59}$$

Since the indices (i, j, k) are repeated we will drop them when writing $\boldsymbol{W}_{i,j,k}$ and, using eq. (3.57) and the continuity equation discretized as follows:

$$
\frac{\rho_{i,j,k}^{n+1} - \rho_{i,j,k}^{n}}{\Delta t} +
$$
$$
\frac{(J_x)_{i+\frac{1}{2},j,k}^{n+\frac{1}{2}} - (J_x)_{i-\frac{1}{2},j,k}^{n+\frac{1}{2}}}{\Delta x} + \frac{(J_y)_{i,j+\frac{1}{2},k}^{n+\frac{1}{2}} - (J_y)_{i,j-\frac{1}{2},k}^{n+\frac{1}{2}}}{\Delta y} + \frac{(J_z)_{i,j,k+\frac{1}{2}}^{n+\frac{1}{2}} - (J_z)_{i,j,k-\frac{1}{2}}^{n+\frac{1}{2}}}{\Delta z} = 0,
$$
$$\tag{3.60}$$

we get the relation between the decomposition vectors and the shape functions:

$$
W_x + W_y + W_z = S(x + \Delta x, y + \Delta y, z + \Delta z) - S(x, y, z). \tag{3.61}
$$

The right hand side of this last equation is called "3D shift of the shape function" while the vector $(\Delta x, \Delta y, \Delta z)$ is called "3D shift in the macroparticle position". Now, because we assumed linearity we can say that any 3D shift in shape function can be expressed as a linear combination of 1D shifts in a shape function. In order to simplify the notation we will define eight functions each one corresponding to one particular position shifts combination:

$$
f_1 = S(x, y, z), \tag{3.62}
$$

$$
f_2 = S(x + \Delta x, y, z), \tag{3.63}
$$
$$
f_3 = S(x, y + \Delta y, z), \tag{3.64}
$$
$$
f_4 = S(x, y, z + \Delta z), \tag{3.65}
$$
$$
f_5 = S(x + \Delta x, y + \Delta y, z), \tag{3.66}
$$
$$
f_6 = S(x + \Delta x, y, z + \Delta z), \tag{3.67}
$$
$$
f_7 = S(x, y + \Delta y, z + \Delta z), \tag{3.68}
$$
$$
f_8 = S(x + \Delta x, y + \Delta y, z + \Delta z). \tag{3.69}
$$

Given these definitions it can be shown[41] that the decomposition vectors can be written as:

$$
W_x = \frac{1}{3} \left(f_8 - f_7 + f_2 - f_1 \right) + \frac{1}{6} \left(f_6 + f_5 - f_4 - f_3 \right), \tag{3.70}
$$

$$
W_y = \frac{1}{3} \left(f_8 - f_6 + f_3 - f_1 \right) + \frac{1}{6} \left(f_7 + f_5 - f_4 - f_2 \right), \tag{3.71}
$$

$$
W_z = \frac{1}{3} \left(f_8 - f_5 + f_4 - f_1 \right) + \frac{1}{6} \left(f_7 + f_6 - f_3 - f_2 \right). \tag{3.72}
$$

Now that we defined $\boldsymbol{W}$ as a function of the shifted shape functions we need to solve eq. (3.58) in order to find the right current $\boldsymbol{J}$ to plug it in the PIC loop.

It should be stressed that this method is valid only for Cartesian geometries, but can be used for any shape functions order given that the 3D shape function can be written as product of 1D shape function such as:

$$
S^{3D}(x, y, z) = S^{1D}(x) S^{1D}(y) S^{1D}(z). \tag{3.73}
$$

The algorithm also assumes that all macroparticles cannot move along a straight line of more then a cell length per timestep, but this is already ensured by the CFL condition (eq. (3.50)).

3.8 Radiation reaction in PIC codes

In chapter 1 we described the process of photon emission and we discussed from a theoretical point of view the concept of *Radiation Reaction* (RR). We discussed also the differences between coherent and incoherent radiation, and we said that coherent radiation is not well accounted for in PIC codes, but we did not explained why. Now that we have explained the fundamental features of a PIC code we can understand how photons are created and thus how radiation is managed inside the code.

In PIC codes each macroparticle is treated independentely, and so incoherently, with respect to the others. All macroparticles meet the requirement to emit individually, regardless of the nearby macroparticles. This means that all the photons (macrophotons) produced by the radiation reaction modules are always representative of an incoherent kind of radiation.

Since we always refer to *synchrotron-like* radiation, all kind of charge oscillation with spatial scale larger than the mesh resolution Δx is accounted in the code. The electromagnetic fields created by any oscillation of space scale larger than Δx can in fact be resolved by the grid. This kind of radiating behaviour transfers energy directly into the fields and thus does not create a macrophoton. Practically this translates into a minimum wavelength which can be resolved by the mesh ($\lambda_\gamma > \Delta x$), and following the steps of section 1.3 we can find out what this threshold wavelength is, and thus the maximum photon frequency (and energy) accounted by this process in the code ($\gamma_\gamma < 5 \times 10^{-4}$ corresponding to $\epsilon^{photon} \sim 250$eV). It is crucial to point out that it is nearly impossible to measure any energy emitted by a macroparticle in this way. The radiation emitted in this process is, by the definitions of section 1.3, considered a coherent kind of radiation [10][14]. This is the only coherent radiating behaviour that a PIC code is nowadays able to accurately describe.

As for incoherent radiation emission, the specifics on how a macroelectron can radiate a macrophoton, depending on the employed method, will be given in the following subsections. The basic concept is that if an electron (macroelectron) is found fulfilling the necessary condition to radiate, then a photon (macrophoton) is emitted in the forward direction, which coincides with the direction of the instantaneous velocity of the electron. The energy and momentum of the radiating particle are updated considering the properties of the emitted photon. In opposition to what said regarding coherent radiation, now (incoherent behaviour) the energy radiated away by the particles is stored into macrophotons, and thus is easily measurable.

We have seen that coherent radiation of wavelength $\lambda_\gamma > \Delta x$ ($\sim$ 5nm in our configurations) is accounted in the code as it modifies directly the fields values. Incoherent radiation instead is accounted, as we have seen in section 1.3, up to a maximum value of wavelength ($\lambda_\gamma < 0.8$nm in our configurations). A range of wavelengths is created which is not modelled by the code. Fulfilling the hypothesis of section 1.3, we can ensure that the amount energy radiated in this awkward interval of wavelengths is negligible to the energy emitted in the rest of the spectrum [14].

While running simulations with Smilei the user can select different approaches for the computation of radiation reaction: Landau-Lifshitz (LL), quantum corrected Landau-Lifshitz (cLL), Focker-Planck (FP) or Monte-carlo (MC). The first three methods are based on the Landau-Lifshitz continuous radiation emission described in section 1.1.3, while the last one takes into account the stochastic effects at play for χ approaching 1.

3.8.1 Classical radiation reaction

Classical radiation reaction can be taken into account within the Boris pusher we talked about in section 3.6 as a correction on the final momentum $\boldsymbol{p}^{n+\frac{1}{2}}$ using the results at the end of section 1.1.3. More specifically we compute the correction using the properties of the particle at the previous timestep as[7]:

$$\Delta\boldsymbol{p}_{RR} = -P_{cl}\frac{\Delta t}{c}\boldsymbol{\Omega}^{n-\frac{1}{2}}, \tag{3.74}$$

with $\boldsymbol{\Omega}$ being the normalized momentum:

$$\boldsymbol{\Omega} = \frac{\boldsymbol{p}}{|\boldsymbol{p}|}, \tag{3.75}$$

so that now eq. (3.55) becomes:

$$\boldsymbol{p}^{n+\frac{1}{2}} = \boldsymbol{p}^{+} + q_s\boldsymbol{E}^n\frac{\Delta t}{2} + \Delta\boldsymbol{p}_{RR}. \tag{3.76}$$

This model is referred as "Landau-Lifshitz" or "LL" in this work and in the documentation of Smilei [45].

It is possible to apply a "quantum correction" to the classical approach as described in eq. (1.43), which is unfortunately way too complicated to be implemented in the solver. In order to correct the purely classical formulation, a fit proposed in [46] is used. The fit function reads:

$$g(\chi_e) = \left[1 + 4.8(1 + \chi_e)ln(1 + 1.7\chi_e) + 2.44\chi_e^2\right]^{-\frac{2}{3}}. \tag{3.77}$$

In this case eq.(3.74) becomes:

$$\Delta\boldsymbol{p}_{RR} = -P_{cl}g(\chi_e)\frac{\Delta t}{c}\boldsymbol{\Omega}^{n-\frac{1}{2}}, \tag{3.78}$$

The user is always encouraged to use the quantum corrected version of the LL model ("cLL" - as in "Corrected") if $10^{-3} < \chi < 10^{-1}$. If then the quantum parameter reaches unity a stochastic method should be used like the Focker-Planck or the full Monte Carlo method.

The Focker-Planck method follows a classical approach but considers some of the stochastic effects intrinsic of quantum mechanics. This method has been shown to be almost equivalent to the full Monte Carlo approach up to $\chi_e \sim 1$ [45][47].

All the methods explained in the present section consider a radiation emitted in a continuous spectrum, and do not consider the radiation emitted as made up of individual photons.

3.8.2 Monte Carlo method

This subsection is written following the steps from [4][7][45].

When the electron quantum parameter χ_e approaches 1 the photons energy becomes of the order of the electron kinetic energy. In this scenario the single photon feedback is important on the overall electron dynamics, so each photon emission should be accounted singularly. In order to do that PIC codes use a Monte Carlo approach.

At the beginning of the simulation, to each electron is assigned a "final optical length" τ_f sampled as $\tau_f = -\log(r)$ with r a random number in the interval $]0; 1]$. A "current optical depth" τ_c is also assigned and initialized to zero. The process

now is to increment τ_c once for each timestep until it reaches τ_f and in that moment the electron emits a photon, τ_c is brought back to zero, and τ_f is sampled again. In order to modify the current optical length additional steps are added to the PIC loop in which τ_c is increased following:

$$\frac{d\tau_c}{dt} = \int_0^{\chi_e} \frac{d^2 N_\gamma}{d\chi_\gamma dt} d\chi_\gamma, \tag{3.79}$$

in which the integrand is the spectral rate of emission of eq. (1.36). When $\tau_c \geq \tau_f$ a photon is emitted with energy that can be computed sampling another random number ξ in the same interval $]0;1]$ and then reversing the following relation to find χ_γ which is a parameter related to the photon energy defined in eq.(1.34) [4][7]:

$$\xi = \frac{\int_0^{\chi_\gamma} G(\chi_e, \chi'_\gamma) d\chi'_\gamma / \chi'_\gamma}{\int_0^{\chi_e} G(\chi_e, \chi'_\gamma) d\chi'_\gamma / \chi'_\gamma}. \tag{3.80}$$

It is important to say that the value of χ_e is taken at the moment of the emission. From this last equation we can extract χ_γ and with it using eq. (1.35) we can get the photon energy:

$$\epsilon_\gamma = m_e c^2 \gamma_\gamma = m_e c^2 \frac{\gamma_e \chi_\gamma}{\chi_e}. \tag{3.81}$$

At this point the electron momentum has to be corrected accordingly, so considering only forward emission we add a step into the Boris pusher just like eq.(3.76) with:

$$\Delta \boldsymbol{p}_{RR} = -\frac{\epsilon_\gamma}{c} \boldsymbol{\Omega}, \tag{3.82}$$

in which we rember that $\boldsymbol{\Omega}$ represents the direction of motion of the particle.
It is due to mention at this point that this method is granted to conserve the total momentum in the system but not the total energy, although the error has been shown to decrease with the increse of the electron energy and be negligible for $\gamma_e \gg 1$ [7].

3.9 Ionization and collisions

Here we will give a brief overview on how effects like *Tunnel ionization* (or *Field ionization*) and binary collisions are implemented in Smilei. In chapter 5 we will investigate how these two phenomena will afect the simulations output.

3.9.1 Field ionization

In general field ionization is a process of particular importance for laser-plasma interaction in the non-relativistic regime and, it could likely be relevant in the ultra-high intensity regime. It afffects the energy trasfer from laser to electrons, and thus could be important in the dynamics of the whole system. This process is not described in the standard PIC (Vlasov-Maxwell) formulation, and an *ad hoc* description needs to be implemented. A Monte Carlo module for field ionization has thus been developed in Smilei [48].
This method is based on the cumulative probability $F_k^{Z^*-1}$ to ionize from 0 to k times an atom/ion with initial charge state $Z^* - 1$ during a single timstep Δt defined as:

$$F_k^{Z^*-1} = \sum_{j=0}^{k} p_j^{Z^*-1}, \tag{3.83}$$

in which $p_j^{Z^*-1}$ represents the probability to ionize the atom/ion exactly j times. The module proceeds by sampling a random number r with uniform distribution from 0 to 1, and checks if $r > p_0^{Z^*-1}$ which corresponds to the probability to ionize the atom 0 times, so to not ionize it. If the test fails then the atom is not ionized during the timestep, otherwise it keeps increasing the value of k until $r < F_k^{Z^*-1}$. At that point k is selected as the number of ionization events, a macroelectron with weight k times the one of the ion is created and the ionization state of the atom is increased by the same value. The created macroelectrons have all the same momentum of the parent ion.

Since the atomic structure is not modelled in the code, in order to account for the loss of electromagnetic energy due to ionization, a fictitious current density $\boldsymbol{J}_{ion}$ is defined as:

$$\boldsymbol{J}_{ion} \cdot \boldsymbol{E} = \Delta t^{-1} \sum_{j=1}^{k} I_p(Z^* - 1 + k), \tag{3.84}$$

in which $I_p(Z^* - 1 + k)$ represents the ionization potential of the ion with charge state $Z^* - 1 + k$. It is shown in [49] that introducing this current density into Ampere law leads to a loss in electromagnetic energy due to ionization processes computed as:

$$\frac{dU_{elm}}{dt} = -(\boldsymbol{J} + \boldsymbol{J}_{ion}) \cdot \boldsymbol{E}, \tag{3.85}$$

ensuring energy conservation.

3.9.2 Collision module

Collisions between two particles (Binary Collisions) are implemented in Smilei with the same scheme as in the Particle-In-Cell code CALDER following the model proposed in [50]. We will give a brief summary of how collisions are implemented and we refer to [50] for a deeper reading.

In the center of mass frame, an elastic collision between two particles is equivalent to a rotation. Since the scheme must be valid for arbitrary temporal resolution, even for timesteps larger than the characteristic time between each collision, the code does not measure directly the angular deviation following each collision but computes a cumulative deviation angle ϕ (from the current trajectory) outcome of N collision events. The cumulative angle distribution writes:

$$f(\phi) = \frac{A}{4\pi \sinh A} \exp(A \cos \phi), \tag{3.86}$$

with A being the solution to the equation:

$$\coth A - \frac{1}{A} = \exp(-s_{12}), \tag{3.87}$$

and $s_{12} = N \langle \theta^2 \rangle / 2$ where $\langle \theta^2 \rangle$ is the mean squared scattering angle for a single collision.

Once $f(\phi)$ is obtained, the cumulative deviation angle is extracted stochastically following the distribution and the correction to the momentum in the center of mass frame is computed. Afterwards, the correction is translated into laboratory frame and the particles momenta are updated[50].

In order to consider also inelastic collisions and thus collisional ionization, a Monte Carlo scheme similar to the one described in section 3.9.1 has been implemented to

manage the ionization probability for each collision [51].

It should be remarked now that elastic collisions are implemented among all species, while collisional ionization is currently supported only for *inter-collisions* (collision among different species), and only if one of those species is an electron. It is then impossibile in the code to have, for example, an ion-ion collision resulting in ionization of one or both the particles.

3.10 Goal of this thesis work

At this point, all the elements necessary to understand the motivations and goals of this thesis work have been laid out. In the introduction we gave a brief explanation of why commercial compact photon sources would be interesting, together with an overview on state-of-the-art laser facilities. Different kinds of radiation sources are used for a variety of applications, ranging from medicine, to industry, and research. High energy photons have several applications in all those sectors and nowadays are produced either with radioisotopes or with particle accelerators. The former are non-tunable sources which cannot be switched on and off causing radioprotection issues, while the latter are incredibly expensive and space-consuming devices. Achieving a configuration able to produce high energy, brilliant photon beams but being tunable, realtively cheap, *table-top*, and with reduced radioprotection risk, is therefore of great appeal. We think that significant steps forward in this direction could be done employing the upcoming multi-PW facilities coupled with innovative targetry.

In chapter 1 we discussed the fundamental aspects of the physical processes which lead to the production of photons. We understood that the fundamental requirement to develop a synchrotron-like radiation source is to generate both energetic electrons ($\epsilon_{kin} >\sim 10^1 \mathrm{MeV}$) and huge electromagnetic fields ($a_0 >\sim 10^1$). We then explored the characteristics of the emitted radiation regardless of how the right conditions are obtained, understanding that the more energetic the electrons and the stronger the electromagnetic field sorrounding them, the more copious the emission and the higher the photon energy.

Instead in chapter 2 we focused on how to meet those requirements. Special attention has been given to laser-matter interaction, and in particular to the dynamics and behaviour of electrons in a near-critical-density (NCD) plasma. Modern targetry can reach very low density ($\sim n_c$) being able to enhance the energy transfer from laser to electrons. The more energy is absorbed, the more energetic electrons are produced, thus leading to the emission of more intense and energetic radiation [52][53]. Nanostructured low density targets are then more interesting for this kind of applications than tradiational solid density thick foils. A brief overview of how those innovative targets are manifactured, and their basic properties has also been given.

On paper, the Apollon facility could be a perfect fit to explore the photon production regimes. The "Phase 1" of the facility is almost ready and operational and experimental campaigns are scheduled to start in winter 2020. For the first time what has been studied only theoretically, has now the possibility to be investigated experimentally so that, a need to design complex experiments arises. This thesis places itself in this line of work. Here, we investigate the aforementioned physical system (i.e. the Apollon laser system interacting with double-layer targets) for the purpose of photon generation by means of numerical Particle-In-Cell simulations. The idea is to get a deeper theoretical knowledge on such complex system, with the ultimate goal to support the design of possible future experimental campaigns.

Providing a broad understanding of the behaviour of double-layer targets under such interaction conditions is important not only to guide the experimental design, but also to provide a suitable physical interpretation. In order to do so we need to unvail the full behavior of the system, grasping its complexity and characterizing the consequent outcome. For this reason, special attention will be paid to several crucial aspects related to the numerical modeling, having to compromise between accuracy and feasibility.

Because of the specific nature of the analyzed phenomena, a kinetic approach is the most suitable choice. The essential tool we used to achieve our goal has been the kinetic (Particle-In-Cell) code Smilei[3] we described in chapter 3. We wanted to simulate the behaviour of slightly different set-ups in a parametric study touching upon mainly the average density of the target, its structure and, the laser intensity. Every simulation is carried out with both the nanostructured and homogeneous modelling in order to address the effect of the nanostructure on the outcome. More realistic set-ups would take into account nanostructure, but in order to distinguish between effects due to the structure itself and effects derived from other features consider a homogenous plasma for reference.

Multidimensional simulations are required in order to be representative of a realistic set-up. Ideal would be full 3D3V simulations (meaning 3 spatial dimensions and 3 dimensions in momentum space), but the incredibly high cost of each one of them (estimated $\sim 10^{5 \div 7} CPU hours$) makes them unsuitable for vast parametric studies such as this one. 2D3V simulations were the best choice, considering 1D3V simulations not being representative of the system. Nonetheless, 3D3V version of some of the simulations here presented are to be run atthe insitution in which I carried out this work: the *Theory, Interpretation, Plasma & Simulation* (TIPS) group at the *Laboratoire d'Utilisation des Lasers Intenses* (LULI). Because of the computational cost of each simulation, state-of-the-art supercomputers are needed. All the simulations here presented were carried out on the Irene Joliot Curie machine hosted at the *Très Grand Centre de Calcul* (TGCC).

In particular, the second part of this thesis will be organized as follows:

- *Chapter 4.* Physical and numerical modelling of the laser and the target.

- *Chapter 5.* Analysis of the effect of the modelling of additional physics on the system. In particular, we are interested in understanding if accounting for the ionization processes and the collisional behaviour affects the outcome of the simulations in the regimes of interest.

- *Chapter 6.* Investigation on some important properties of the propagation of an ultra-intense laser pulse into a near-critical-density double-layer target.

- *Chapter 7.* Extensive parametric study on the photon produced by the afore-mentioned configurations.

- *Chapter 8.* The conclusions of this work will be presented, and proposals for future studies and developments are suggested.

Part II

Results and discussion

Chapter 4

Numerical modelling and parameters

In this chapter we will explain the choice of the numerical parameters and the numerical modelling of both the laser pulse and the target.

All simulations are carried out with the open source PIC code Smilei [3].

Is well known that dimensionality plays a crucial role in PIC codes, so chosing 3D3V geometry would help us describe a more realistic set-up. Nevertheless 3D PIC simulations of this kind of systems are too expensive to be used for parametric studies like in this thesis. The cheapest geometry would be 1D3V but unfortunately it is not representative of the system. Every simulation is then carried out in 2D3V geometry, which let us preserve the fundamental behaviours of the system which we will expand upon later.

First we are going to look at the laser and starting from the paraxial equation we will derive the diffraction disk (Airy disk) which is theoritically the most accurate description of any wavefront after a focusing element (lense or mirror). Practically a laser pulse is never described as a diffraction pattern but with a Gaussian shape instead, so next we will fit the Airy disk with a Gaussian function that conserves both peak intensity and total energy. Finally we will take the official specifics of the Apollon laser and we will see how the combination of those parameters and the Gaussian model we derived translates into the numerical parameters of the simulated laser pulse. Next comes the target. We will describe the Multi-Layered-Target (MLT) we are going to use and break down each component, explaining how each one is simulated. Last, we will briefly address the numerical modelling ofsome physics modules which are not included in the standerd PIC loop such as: photon emission, Tunnel Ionization, and Collisions.

4.1 Laser modelling

The Apollon laser is one of the top UHI facilities, and it is in its final stage of construction at the CEA site not far from the Ecole Polythecnique where I conducted this study. One of the aims of this thesis is to understand the behaviour of specific target configurations under the nominal condition of this laser in order to serve as cornerstone to help project experiments in the near future. For these reasons it will now follow a brief description of Apollon's parameters and their implementation in the code.

4.1.1 Paraxial optics and laser front

We will start this chapter briefly addressing the important points in paraxial optics that we will need in the following sections.

Starting from Maxwell equations and assuming light propagates in straight trajectories (paraxial hypothesis), it is possibile to derive what is called "paraxial equation" [7] which reads:

$$\nabla^2_\perp u + 2ik\partial_z u = 0, \tag{4.1}$$

with i being the imaginary unit, k the wave vector of the wave and, u the wave function of the field. The solutions to this equation describe how a light ray propagates into space.

We are interested in finding the analytical shape of the laser front after the focusing mirror of diameter D, and this can be thought as a diffraction problem in which the beam prior the mirror represents the source and the focused beam represents the diffracted field. The field amplitude after the mirror can be written as:

$$E(\boldsymbol{R}) = E_0 M(\boldsymbol{R}) e^{i\frac{k_0 R^2}{2f}}, \tag{4.2}$$

where $\boldsymbol{R}$ is the radial position right after the mirror, M is called "mask function" and is defined as 1 if $R < D/2$ and 0 otherwise, and f is the focal distance of the mirror. The last exponential term represents the curvature that the mirror, or any focusing tool, gives to the beam and is expressed as a phase change.

We are interested in systems which have f-number $f_\# = f/D$ of the order of 2-3 that corresponds to the near-field approximation. Is it possible to write an enough general solution for these kind of problems called "Fresnel integral" or "Fresnel diffraction formula":

$$E(\boldsymbol{r}, z) = -i\frac{e^{ikz} e^{i\frac{kr^2}{2z}}}{\lambda z} \iint_{source} d^2 R E(\boldsymbol{R}, 0) e^{-i\frac{kR^2}{2z} + i\frac{k\boldsymbol{R}\cdot\boldsymbol{r}}{2}}, \tag{4.3}$$

where z is the propagation coordinate. $z = 0$ correspond to our mirror/source, and $\boldsymbol{r}$ is instead the radial coordinate on the plane of the diffraction figure.

Plugging eq. (4.2) into eq. (4.3) and considering $z = f$, rearranging the equation and collect all the phase parameters in front of the integral in the term $e^{-i\phi}$ we can write:

$$E(\boldsymbol{r}, f) = ie^{-i\phi}\frac{E_0}{\lambda f} \int_0^R dR R \int_0^{2\pi} d\theta e^{i\frac{kRr}{f}cos(\theta)}. \tag{4.4}$$

We can now notice that the last integral is one of the definition of the Bessel function of first kind of order zero [54] and so we can rewrite the equation as:

$$E(\boldsymbol{r}, f) = ie^{-i\phi}\frac{2\pi E_0}{\lambda f} \int_0^R R J_0\left(\frac{kRr}{f}\right) dR. \tag{4.5}$$

Using properties of Bessel functions [54] and defining $r_0 = (\lambda f)/(\pi D)$, we can then show that the equation takes the final form:

$$E(\boldsymbol{r}, f) = ie^{-i\phi}\frac{DE_0}{4r_0}\frac{2J_1(r/r_0)}{r/r_0}. \tag{4.6}$$

The intensity of the field is then:

$$I(\boldsymbol{r}, f) = \frac{1}{2}c\epsilon_0 |E(\boldsymbol{r}, f)|^2 = \left(\frac{D}{4r_0}\right)^2 \frac{c\epsilon_0}{2}|E_0|^2 \left(\frac{2J_1\left(\frac{r}{r_0}\right)}{\frac{r}{r_0}}\right)^2 = I_0 \left(\frac{2J_1\left(\frac{r}{r_0}\right)}{\frac{r}{r_0}}\right)^2. \tag{4.7}$$

This function is the representation of a diffraction pattern after a circular aperture and is called Airy disk. We will use this result in the following section when discussing the most fitting shape for the implementation of the laser front.

4.1.2 Intensity profile

In Smilei every laser pulse is completely defined by $B_z(x = 0, t)$, we will then specify the profile only for this field. Experimentally the spatial parameters can be pretty difficult to measure but the gaussian profile is considered the best representation for high intesity short pulses, so in order to give a description with the best accordance possible to the experiment we will use a taylored gaussian profile.

Smilei always starts propagating the laser for a boundary of the simulation box, so the parameters at the boundary are needed. If the profile is not a plane wave but a gaussian which changes its properties during the propagation, Smilei needs the parameters relative to the focal spot and then it computes the initializing parameters using the maxwell solver to propagate back the pulse to the box boundary.

B_z in the focal spot is then defined as:

$$B_z (r, t) = f (t) g (r), \qquad (4.8)$$

in which $g(r)$ denotes the spatial profile while $f(t)$ the temporal shape.

Assuming the spatial profile is a gaussian we will then write:

$$g (r) = B_0 exp \left[-\frac{r^2}{w_0^2} \right], \qquad (4.9)$$

with:

$$B_0 = \frac{m_e \omega_0 a_0}{e}, \qquad (4.10)$$

where m_e is the electron rest mass, e is the proton electric charge, ω_0 is the laser central frequeny and, a_0 is the normalized vector potential of the field, and w_0 is called "waist of the pulse in the focal spot" and will be define later on.

The nominal temporal profile (without any pedestal or pre-pulse) is given to us by the Apollon team as proportional to a *sin* function so $f(t)$ is defined to be:

$$f (t) = sin \left(\frac{\pi t}{2\tau_p} \right), \qquad (4.11)$$

taken for the intervall:

$$0 < t < 2\tau_p, \qquad (4.12)$$

where $2\tau_p$ is the time length of the pulse. The value of τ_p will later refelect the full-width-half-maximum (FWHM) of the intensity profile. We now have to define the key parameter w_0 not only numerically but also physically. In order to do that we look at the intensity profile of a generic diffracted wave and then travel our way back to the field parameters.

From the experimental point of view what is know is the the energy stored in the pulse U_p, the dimension of the beam before focusing D, the focal distance of the parabola f and the pulse duration τ_p. We will henceforth try to express the intensity profile as a function of these parameters, easily accessible to experimentalists. Aim of this section is to define the pulse using an easy and transversal language among theory, simulation, and experiment.

The intensity of the pulse is then defined as:

$$I(r,t) = F(t)G(r).\tag{4.13}$$

The optics at Apollon give an f-number $f_{\#} \equiv f/D$ ranging from 2.5 to 3.5, in this condition we can put ourselves in the near-field approximation also called "Fraunhofer diffraction". An extensive derivation of the profile is beyond the purpose of this thesis so we summarized the main results in section 4.1.1.

The most rigurous spatial function of a circular beam after a focusing device would be an Airy function (or Airy disk) given by eq. (4.7):

$$G(r) = I_0 \left[\frac{2J_1\left(\frac{r}{r_0}\right)}{\frac{r}{r_0}} \right]^2,\tag{4.14}$$

with :

$$r_0 = \frac{\lambda_0 f}{\pi D},\tag{4.15}$$

$$I_0 = \frac{\pi U_p}{4\lambda_0^2 \tau_p} \left(\frac{D}{f}\right)^2,\tag{4.16}$$

in which λ_0 is the central wavelength of the laser. For the sake of semplicity we will approximate said distribution with a customed gaussian profile with same peak intensity and same area. In order to have the same peak intensity all is needed is having the same I_0. In order to have the same area we need to integrate over all space a generic Gaussian curve and eq. (4.14). The unknown in this last condition would be the pulse waist w_0 which determines how "sharp" the pulse will be. We are then able to write our gaussian profile as:

$$G(r) = I_0 \cdot exp\left[-2\frac{r^2}{w_0^2}\right],\tag{4.17}$$

with:

$$w_0 = \frac{2\sqrt{2}}{\pi}\lambda f_{\#}.\tag{4.18}$$

In Fig. 4.1 we can see as the gaussian approximation conserves the peak intensity but is relatively larger than the main peak of the Airy disk. This effect is due to the choice of having the same area under both curves so that we are able to have the same pulse energy regardless of which profile is used.

  The peak intensity is maybe the most important parameter to take into account to have an intuitive and immediate estimate of the phenomena at play in the target, so it would be very useful to have a compact and easy expression to estimate it only by the main laser parameters. I_0 as expressed in eq. (4.16) is mathematically very simple but we can do better rearranging the dimensional similar terms to find:

$$I_0 \cdot \lambda_0^2 = 3.927 \left(\frac{D}{f}\right)^2 \left(\frac{U_p}{10J}\right) \left(\frac{20fs}{\tau_p}\right) \cdot 10^{22} \frac{W \cdot \mu m^2}{cm^{-2}}.\tag{4.19}$$

This way even without a calculator at hand would be way easier to estimate the peak intesity of the pulse.

All we need now is the intensity temporal profile which is the most simple task at this point. For what we said before we know that the intensity temporal profile is
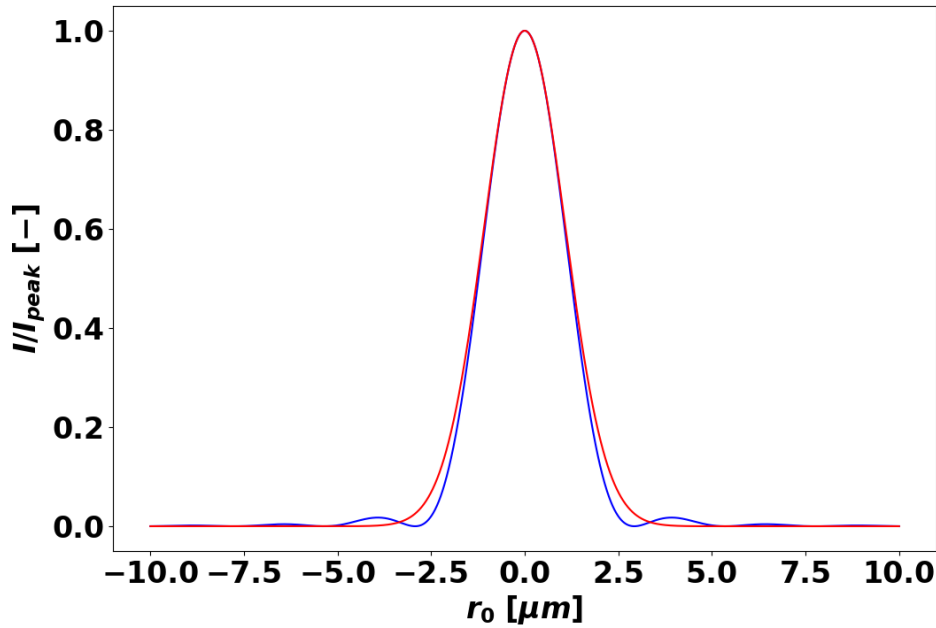
Figure 4.1: Comparison of the Airy function (eq. 4.14) and its gaussian approximation (eq. 4.17). Plotted are the intensity functions, both normalized to their peak intensity which is always I_0 defined in eqs. (4.16) and (4.19).

just the square of the field temporal profile, so we can write simply:

$$F\left(t\right) = sin^2\left(\frac{\pi t}{2\tau_p}\right),\tag{4.20}$$

taken for the intervall:

$$0 < t < 2\tau_p.\tag{4.21}$$

4.1.3 Parameters

Apollon is very close to be operational but the full potential of this structure would actually realize in the next years. We are now entering what is called "Apollon phase 1", with one available beam of total energy 20J, a beam diameter before focusing of 14 cm, optics with f-number 3.5 and a temporal FWHM of 20 fs. This configuration would lead us to an effective peak power on target of about 1 PW.

Next will be the finalization of the contruction of another beamline exploiting 60J with a 40 cm beam diameter prior focusing and $f_\# = 2.5$, always with a pulse duration of 20 fs, leading to a power on target of about 3 PW. This is what is called "Apollon phase 2" and is realization is scheduled for the next years.

Last we find "Apollon phase 3" which should be the last stage in which the energy of the second line should be brought up to 150J, this leading to an effective peak power of about 7.5 PW. We summarized all the main parameters of these different configurations in table 4.1 for easy access and comparison. In order to avoid confusion, in the frame of this work we renamed the official phases of Apollon as letters (A, B, C) instead of numbers (1, 2, 3).

In table 4.1 are present both πr_0 and w_0 belonging respectively to the Airy disk description (eq. 4.7) and Gaussian description (eq. 4.17).

In the frame of this work we only used configuration A and B, while for a study on

Apollon configurations

	A	B	C
Pulse energy (J)	20	60	150
Beam diameter (before focusing) (cm)	14	40	40
f number (-)	3.5	2.5	2.5
I_0 (10^{22} $W \cdot cm^{-2}$)	1.002	5.891	14.73
a_0	68	166	263
πr_0 (μm)	2.8	2.0	2.0
w_0 (μm)	2.52	1.80	1.80

Table 4.1: Three different set of parameters corresponding to the different stages of developping of the Apollon laser. The parameter τ_p is set to 20 fs for every configuration.

C we refer to future works, perhaps when experiments with configuration A and B have already given us data to analyze and compare to this and other works.

4.1.4   Further complications at higher intensities

In a preliminary investigation we found out that for configuration A ($a_0 = 68$, $w_0 = 2.52\mu$m) the exact point at which the laser was focused did not really matter as far as it enters the foam with negative divergence (still focusing). Therefore up until now we focused the laser onto the mirror regardless of the fact that for longer foams we would have slightly smaller amplitude of the field at the entrance of the foam. This effect is totally negligible for configuration A and the reason could be found in the Rayleigh Length $z_R = \pi w_0^2/\lambda_0$ wich is $\approx 25\mu$m. We know that z_r is often identified as the characteristic length of the focusing/defocusing mechanism near the focal point in free propagation of a gaussian pulse. Roughly speaking, if the focal distance of a laser is z_0 then the pulse is still considered focused for $z_0 - z_R < z < z_0 + z_R$. This might seem a naive approximation but it is reflected in the simulations outcome. In this configuration most of the targets have foam layers thinner than z_R so that effectively the laser impacts with the same field on the foam. When we switch to configuration B ($a_0 = 166$, $w_0 = 1.8\mu$m) z_R becomes roughly 13μm which is now smaller than most of the foams. So now we face a big difference in propagation properties from one case to another. The easiest way to look at this problem is to choose between two options: keep the same focal distance for every case and ignore the possibility to find a "best" choice for the sake of consistency, or, change the focal point for each case trying to maximize the efficiency at the expenses of consistency. The second option requires a tailored parametric study on its own and would rely on knowledge on the properties of the propagation of lasers into NCD plasma that we do not have at this point, and also, would make us lose some properties of the systems we will use in the discussion in chapter 7 (i.e. the fact that prior the interaction with the solid substrate every system behaves in the same way for all cases with same a_0 and n_0).
After some consideration we chose to use the same focal length for all simulations that we decided to be 20μm into the foam (only for configuration B with $a_0 = 166$), since that value appeared to be somehow halfway the span of the foam lengths for configuration B.

4.2 Target modelling

After defining the laser shape and parameters is due to decide how to model the target. A crucial point that will be investigated is the ionization state of the target at the beginning of each simulation. When discussing ultra-relativistic regime is always assumed that the target would be immediately and completely ionized by the pulse, so in most works the target is initialized as already a fully ionized plasma[23][30][20][29][52][53][55][56][27][4][33][57][26]. This assumption is based on the fact that for laser intensity $\gg 10^{14} W cm^{-2}$ the atomic bond builds up a potentail barrier which is negligible with respect to the energy given to the electrons by the field. This regime is called "Barrier-less ionization" [58]. Even though the assumption seems solid, the first thing we will do is to try to extend the work done in [29][30] at Politecnico di Milano and check how important is to initialize a foam-based target as neutral with respect to initialize it as a completely ionized plasma from the beginning.

4.2.1 Substrate

The easiest part of the target modelling will be the substrate or "mirror". Since this material is just a plain solid-density foil the obvoius choice would be to use an homogeneous slab-like shape with appropriate density. In literature and in particular in the works [52][53][55] is pretty common to have Aluminium as substrate material. We decided to use Al since is one of the most common substrates in general for foam-based targetry and has high enough electron density to act as a good mirror for laser radiation. The maximum ionization state held by an Al atom is +13, while its mass is taken equal to 27 mass atomic units. The corresponding electron density in fully ionized regime would is computed to be $450 n_c$ with n_c defined in eq. (2.12). In previous works [27] has been show that the substrate thickness has a marginal role in the overal dynamics of the system with respect to the other layers. When using PIC codes is crucial to understand that the most expensive part in the PIC-loop is the particles pusher, therefore the total number of macroparticles in the box has a huge role in the cost of a simulation. For this reason one always tries to use high number of particles only for the components which are interesting to simulate, and the total number of particles is proportional to the volume of a layer, so the smaller a component is the cheaper is to simulate. The role of the substrate is to reflect the pulse once it is hit by it and, if the thickess is sufficient to assolve the job without it being destroyed or damaged excessively, then there is no reason for us to use a thicker substrate that would only increase the computational cost. The thickness has been set to 2 μm since it reasonable and is consistent with the usual thickness of about few laser wavelength as described in literature [27][52][53][55].

4.2.2 Foam structure

The modelling of the foam is surely less trivial. As we can see in [31][32] the processes at play during the production of a foam-based target are complex and their modelling tricky. For a 3D geometry, the choice of the model for the aggregation mechanism is crucial for the final properties of the target [30]. In 2D we cannot hope to reproduce exactly the behaviour of a 3D nanostructure, so we need the 2D structure that let us conserve most of the behaviour we are more interested in.
A near-critical homogeneous layer would be the easiest choice, but as shown in previous works [23] it is not necessarily well representative of a nanostructered foam

even if the average density of the nanostructured case matches the one from the homogeneous one.

The fundamental behaviour we need to conserve is the fact that there must not be any "closure" or "wall" in the laser path, preventing its propagation. This means that in a real porous structure we can imagine to draw a line and pass from one side of the foam to the other without crossing any nanoparticle. This is crucial because otherwise at some point in the propagation the laser could find a "wall" of $n_e \sim 10^2 n_c$ and be almost completely reflected, which never happens with real porous foams.

The only 2D structure that allows us to respect this behaviour is a collection of nanosphere, or more like "circles" since we are in 2D. Phyisically the system will be representative of a collecion of nantotubes with infinite length in the z direction, being the laser propagating in the $x > 0$ direction and calling y the only transverse direction in 2D . Surely this system is not equivalent to structures like the ones in fig. 2.4 but no 2D structure can be, and the one we chose is the closest one: we also defined this collection to be uniformly randomly allocated in the volume to add some disomogeneity tipical of porous materials.

Another important point is the size of the nanoparticles. We do not want the laser
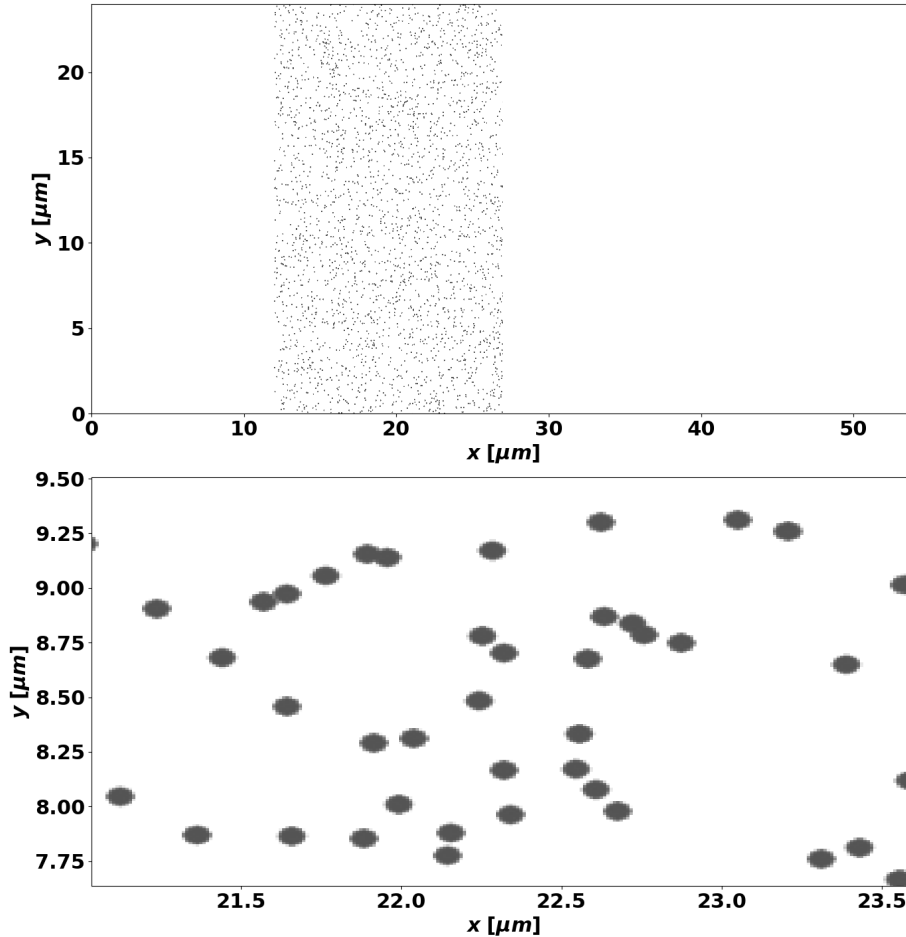
Figure 4.2: Example of foam structure modelled as a collection of spheric nanoparticles, and magnification of the same picture to highlight the single cluster structure.

to be completely reflected by the single particle. In reality this does not happen because the dimension of the cluster is $\ll \lambda_0$. So we want small enough clusters to exploit this property, which should then be no more than $0.1\lambda_0$. Since Apollon is a Ti:Sa laser, its wavelength is 800 nm, so we chose the diameter of the nanoparticles

to be $\sim 80nm$. We could have chosen them to be smaller, but we should keep in mind that PIC codes have a resolution which hardly ever can get below the nm, and we always need enough cells to resolve each nanoparticle. The resolution for this work is 192 point per μm which is equivalent to say that the cell length $\Delta x \approx 5.2$ nm. Choosing 80 nm as a nanoparticle dimension means having roughly 15 cells spanning over its diameter, enabling us to resolve clearly the shape of each nanoparticle. Furthermore the previous work [20][23][29] have all used the same value making our work consistent with prexisting literature.

Two crucial parameters we would like to be realistic are the filling factor and the average density. Unfortunately because of the simulation dimensionality it is impossible to use the same filling factor and the same average density of real 3D foams. Since this work is based on the studies carried on at Nanolab at Polimi ([20][23][29]) we will use their same parameters. The structure is shown in figure 4.2 and the parameters are summarized in table 4.2.

Every simulation will be carried out with both homogeneous and nanostractured foam modelling to appreciate the difference between the two models. We will henceforth refer to these two configurations as HOMO and NANO respectively.

The last thing left to define is the average densities to be used. Since the reason to use foams is to explore the near critical regime we should use densities which are coherent with this point. Although there is no clear threshold for the NCD regime, an appropriate intevall can be $0.1 < n_0/n_c < 10$. Since the laser has incredibly high power, a relativistic correction of the order of 10^{-2} should be applied to the density decreasing by a factor 100. Because of this reason we excluded all value for $n_0 < n_c$ in order to try to stay the closest possible to the NCD regime. We therefore selected the average densities to be $n_0 = \{3,6,9\}$ n_c. The cluster density is now also determined since we will use the same filling factor $f_f = 0.0333$ from [23] in order to be able to relate the two works. The cluster density n_s is then:

$$n_s = \frac{n_0}{f_f}. \tag{4.22}$$

As we already stated we want a strong coupling laser-plasma in all configurations. Different mechanisms of interaction would give more or less efficient coupling. Has been shown by [23] that an important parameter is the "transparency parameter" or "opacity factor" $\overline{n}$ defined as follows:

$$\overline{n} = \frac{n_0}{\sqrt{1 + \frac{a_0^2}{2}}}. \tag{4.23}$$

For $\overline{n} < 0.3n_c$ a channel is generated from the interaction, leading to huge electron currents and effective laser propagation through the foam. Instead if $\overline{n} > 0.8n_c$ the main mechanism is hole-boring (section 2.6.3) which is typical of laser-solid interaction and would not be very interesting in the frame of this work. We would like to highlight, looking at table 4.2, that all cases have $\overline{n} < 0.3n_c$, so we can expect the formation of a clear channel during the propagation in the foam.

4.3 Simulation set-up

In literature when doing PIC simulations all numerical parameters are expressed in function of λ_0 and $tu_0 = \lambda_0/c$, here we decided to do something different. In order to have a more concrete and practical mindset, most of the time we will refer to the

	a_0 Laser	
	68	166
Structure	Randomly arranged spheres	
Sphere nominal diameter (δx)	80 nm	
Filling factor (ff)	0.0333	
Average densities $(\times n_c)$	3, 6, 9	
Corresponding cluster density $(n_s = n_0/ff)$	90, 180, 270	
Normalized opacity factor $(\overline{n}/n_c)$	0.062, 0.12, 0.18	0.026, 0.051, 0.077

Table 4.2: Nanostructured foam physical parameters.

quantities in μm and not in unit of λ_0, eventhough the order of magnitude remains the same it is worth warning that the central wavelentgh of the Apollon laser is $\lambda_0 = 0.8\mu$m therefore the actual length are indeed different using the two different units. The same goes for the time intervalls, we will use fs and not t_0 although should be noticed that $t_0 \approx 2.67$ fs.

4.3.1   Geometry

The main geometrical and numerical parameters are summarized in figure 4.3 and table 4.3.

First, we find two pictures, the top one will be named *Semi-infinite* case (or "configuration", "geometry"), and the other one will take the name of the foam length in front of the substrate (i.e. "15μm geometry"). The top one will be used whenever we need to investigate the behaviour of the foam during the interaction with the pulse, without discussing any phenomena arising from the substrate presence. This will be done mainly in chapter 5 and 6, while from section 6.2 onward we will discuss the behaviour of a system like the one in the bottom row of figure 4.3. Whenever in this work we refer to *Semi-infinite foam* or *Only-foam* cases we will always indicate a *Semi-infinite* configuration, while when for example addressing a "7μm case" or "21μm configuration" we will always refer to a geometry with substrate just like the one in figure 4.3 (bottom row) with respectively foam length of 7μm and 21μm.
Let's start by naming all the fundamental geometrical parameters. L_x and L_y are the size of the simulation domain in the x and y direction. Going from left to right, or from 0 to L_x along the x axis we find first a region of vacuum of length F_{Sx} ("Foam Start x"). Its initialization allows us to look at the entire laser pulse before it interacts with the target itself, using it as a control tool when looking at the simulation results. Moreover since the implementation of boundary conditions can be tricky in PIC codes, it is common use to have the main interaction not too close to the boundary of the simulation box. Its value is fixed and related to the pulse duration in time. Since our intensity time profile is a $\sin^2$ with a FWHM of 20fs as explained in section 4.1.2, the total time duration of the pulse would be twice that value: 40fs. Light in vacuum travels at roughly 0.3μm/fs so multiplying 40fs times this value we get 12μm which is the exact minimum amount of space needed for the pulse to enter completely inside the box unperturbed. We do not want to increase furthermore this value because it would translate only in more expensive simulations without really any benefit. It is necessary to point out that as will be explained in chapter 5, for the first part of this work (ch. 5) we used a pulse with slightly different temporal shape in order to be able to compare results with literature. In particular we used a pulse with FWHM in fields of 40fs, so that actually $F_{Sx} = 24\mu$m for those
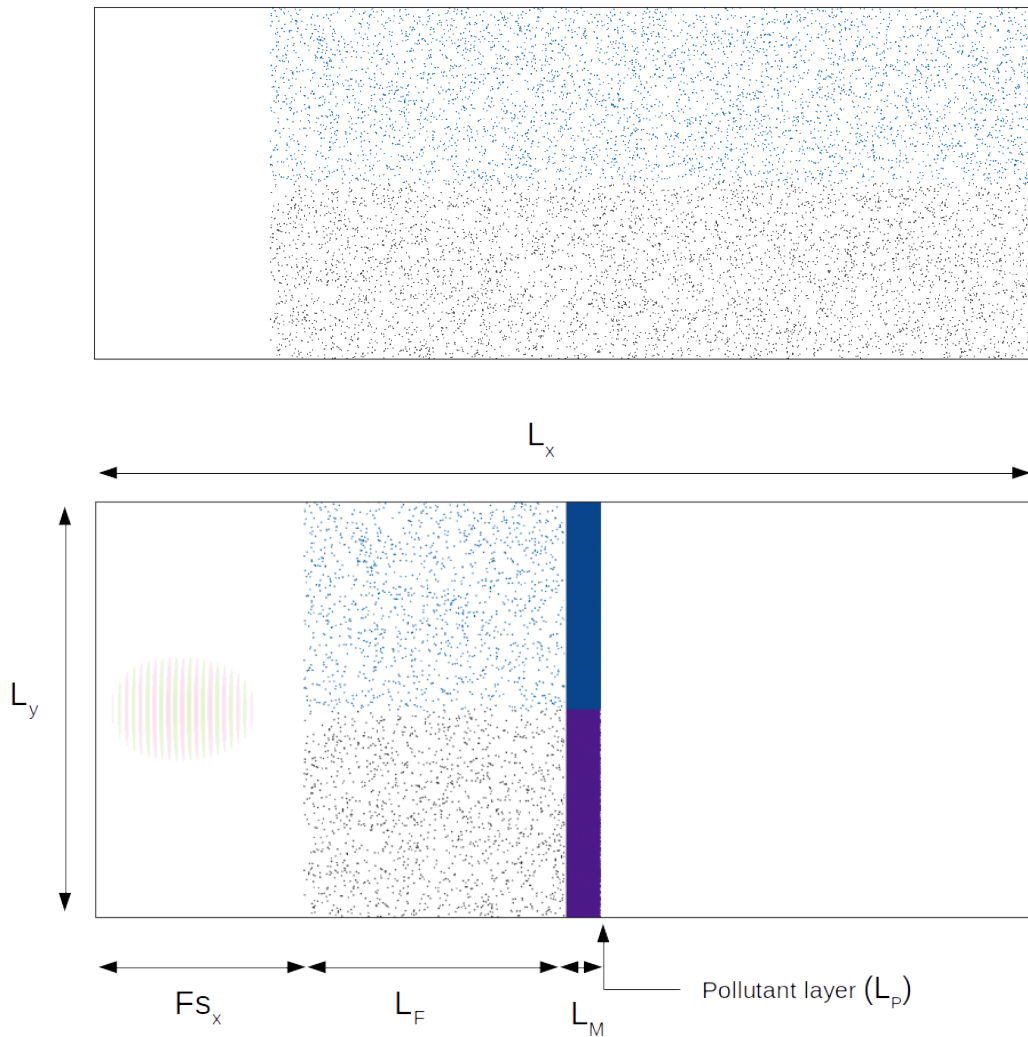
Figure 4.3: Example of geometry employed in the simulations, both are NANO, for a HOMO case the foam should be just "filled" instead of "dotted". The top row represents the configuration used to obtain the results in chapter 5 and section 6.1, called *Semi-infinite* foam. On the bottom row instead is an example of a configuration discussed from section 6.2 onward. In particular this refers to a nanostructured foam of 15μm length with a pulse of temporal FWHM of 20fs. In the top half only elctrons (blue) are plotted while in the bottom half only ions: Carbon (grey), Aluminium (purple) and Hydrogen (red, cannot be seen in this picture because too thin).

and only those cases.

Next we find the foam length L_F. This parameter is actually not fixed but is one of the main three (along with n_0 and a_0) that we are going to scan in order to find the optimal configuration for photon emission. Along all simulations its value varies from 3μm to 36μm. The foam is attached to a mirror (substrate) of thickness $L_M = 2\mu$m as discussed in section 4.2.1. Last we find what in the figure cannot be seen: the pollutant (or contaminant) layer of thickness $L_P \approx 10$nm. It is simply too small to be appreciated in scale with the other layers. Its computational cost is negligible so we decided to initialize it anyway to have a possibily more accurate description of the system.

The total length of the simulation box L_x is not independent from the other parameters but is chosen as $L_x = 2 \times (F_{Sx} + L_F)$. The simulation time T_{sim} is chosen as the time needed for the laser to travel from $x = 0$ to $x = L_x$ in vacuum. By defining these two parameters this way we prevent any part of the main laser pulse to leave the box before the simulation ends and also lets us avoid to loose any energetic particles (photons or electrons) through the right box boundary.

The spatial resolution is fixed to 192 points per μm in order to resolve properly the nanostructured foam as explained is section 4.2.2, but also grants us to resolve the plasma skin depth l_{SD} defined as:

$$l_{SD} = \frac{\lambda_0}{2\pi} \sqrt{\gamma \frac{n_c}{n_e}} \approx \frac{\lambda_0}{2\pi} \sqrt{\frac{a_0}{\sqrt{2}} \frac{n_c}{n_e}} \approx 53\text{nm} > \Delta\text{x} \approx 5.2\text{nm} \qquad (4.24)$$

Resolving the skin depth is essential in order to avoid numerical heating, but is not sufficient, we should be able to also resolve the Debye length associated to the plasma defined as in eq. 2.10. We notice that $\lambda_D \propto \sqrt{T}$ so if the electrons have enough energy the Debye length is resolved, in particular in our configuration we need a temperature greater of about 0.22eV. Initializing electrons with already this energy would mean starting the simulation with particles at already an equivalent temperature > 2500K which is totally unrealistic. If the Debye length is not resolved numerical heating arises injecting noises and errors in the reults, but off course this is a problem occurring only when initializing plasmas, neutral atoms do not give rise to numerical heating because they produce no electrostatic fields. When initializing a full ionized plasma we bypass this problem by first defining the positions of all the ions in the box at $t = 0$ and then placing all electrons on top the respective ions, all particles initialized at $T = 0$K. This way they act almost like a neutral atom having no net fields between each other, and as soon as the laser arrives the electrons are immediately heated up to temperature of the order of $\sim$KeV which is way above the threshold of 0.22eV.

The last numerical parameter are the particles per cell (nppc) which in Smilei must be the same number for both ions and electrons. First we assigned a value of 32 for mirror and pollutant layer which are always modelled as homogeneous. To someone with expertise in PIC simulations this value might seem low for a density of $450n_c$, but it comes from a compromise between realism and costs. Larger nppc would be more realistic but using a value around the few hundreds would make the simulation too expensive. Nevertheless we are interested only in the reflection properties of the substrate, so reducing its density would be unrealistic in the frame of this work. Since we are not interested in the internal dynamics of the mirror we kept the density of $450n_c$ and used a relatively low nppc. This is a trade-off between realism and affordability, but in preliminary investigation we noticed that the difference in behaviour increasing of few times the nppc was negligible.

The nppc for the foam depends on the configuation, the reason being that in general "denser" plasmas need more particles per cell in order to properly interact with the pulse. In HOMO the nppc is set to be 8 in all cases, while in NANO configuration the filling factor of $\approx 1/30$ increases the local electron density so more particles per cell are needed. In NANO configuration a nppc of 120 is used for all densities.

4.3.2 Photon emission

Smilei comes with four different possible radiation reaction modules which we expanded upon in section 3.8 : classical Landau-Lifshitz (LL), quantum-corrected

	Average density n_0		
	3	6	9
Points per [μm]	192		
F_{Sx} [μm]	12		
L_F [μm]	from 5 to 36	from 5 to 24	from 3 to 22
L_M [μm]	2		
L_P [nm]	10		
L_y [μm]	24		
L_x	$2 \times (F_{Sx} + L_F)$		
T_{sim}	L_x/c		
nppc (foam)	(NANO) 120 (HOMO) 8		
nppc (mirror & pollutants)	32		

Table 4.3: Table summarizing the main geometrical and numerical parameters.

Landau-Lifshitz (CLL), Focker-Plank (FP) and, Monte Carlo (MC). In Smilei documentation is expanded upon which module to use depending on the radiating electrons properties, in particular their χ [45]. The classical model should be used when the particles quantum parameter $\chi_e < 10^{-3}$, above that one should use the corrected version up to $\chi_e < 10^{-1}$, above that the Focker-Planck approach should be used until $\chi_e < 1$, then the recommended approach is the full Monte Carlo. Let's clarify that the MC model is the most accurate and can be used even for low χ_e, but it is also the most expensive because it actually creates macroparticles (macrophotons) at runtime which increases the workload on each processor and also memory consumption. For this reason a cheaper choice is recommended when possible.

After a preliminary investigation we found that even for the lesser powerful laser configuration ($a_0 = 68$), the maximum χ_e reached by the particles is $\sim 10^{-1}$ so we would already have the need to employ at least the FP module. Since it is quite obvious that increasing the laser intensity would bring higher value of χ_e, then for consistency we decided to use the MC module in all simulations.

Chapter 5

Foam modelling and additional physics

In this chapter we will discuss if and how the ionization state of the target at time $t = 0$, and collisional behaviours affect the simulations outcome.

A realistic foam prior the interaction with the laser is a collection of neutral atoms, only intense electromagnetic fields are able to ionize its structure. The external field must be stronger than the elettrostatic atomic field defined for hydrogen as :

$$\boldsymbol{E}_H = \frac{e^2}{4\pi\epsilon_0 r_0^2}\boldsymbol{r_0},\tag{5.1}$$

with $r_0 = \hbar/m_e c\alpha$ the Bohr radius $\approx 5.29 \times 10^{-11}$m. A strong electric field strips one electron ionizing the atom, this process is called *Field Ionization* or *Tunnel Ionization* and is activated for a laser with intensity of the order of 10^{14}Wcm^{-2} or above. The actual value depends mainly on the specific element and current ionization state of the atom. For ultrarelativistic lasers the ionizations is thought to be *Effortless* since the field and the intensity are so large that the electron is dragged along without any real resistance from the atomic field [58].

Usually in the frame of works similar to this one, simulations are expensive and so one must find a way to model the system which can be both realistic and affordable, often having to compromise between the two. Initializing a foam as a collection of neutral clusters would be more realistic but also more expensive because it would require to add an ionization module in the PIC-loop, moreover not every PIC code supports ionization schemes. On the other hand initializing the target as an already fully ionized plasma can be too simplistic and might not be representative of the system.

Looking at the values for the parameters in our simulations we thought that since we are in ultra-relativistic regime ($a_0 \geq 68$, $I > 10^{22}$Wcm^{-2}) ionization mechanisms should not play a huge role in the system. Anyway we wanted to know if our belief was true or not so we started from replicating the results obtained in [23][29][30] with the PIC code Piccante [59] and then, using Smilei, add the ionization module, comparing the two cases.

Collisions are instead complex processes which are less and less prevalent increasing the temperature of the particles (eq.(3.13). It is not clear how collisions should affect the system, so we are going to compare collisional and collisionless cases to discuss their effectiveness in this regimes. As already said, larger differences should be found with lower laser intensity, so we used $a_0 = 15$ in order to address the most problematic case in [23][29][30]. First we compared the macroscopic energy

distribution among pulse, electrons and, ions, and then microscopic properties such as electronic and ionic energy spectra at different times.

In order to effectively compare our work with the one done by the NANOLAB at POLIMI we will do this part of the study with their laser parameters: 30 fs temporal FWHM of the intensity and 4 μm waist. Those are enough similar conditions in this context for the conclusions to be extended in our set-up.

We compared the result obtained previously using the code *Piccante* with our code *Smilei*, benchmarking them against each other. This is not usually done by research groups but is crucial because it strongly validates the results of both codes.

We will proceed now looking at two nanostructured cases with different average density $n_0 = \{1, 9\}n_c$. We will run simulations with same geometry and set-up but switching on different physics modules. The resulting configuration will be:

- NTNC → (No Tunnel No Collisions) Foam initialized as a fully ionized collisionless plasma.

- TNC → (Tunnel but No Collision) Foam neutrally ionized. Collisionless.

- TCNI → (Tunnel with Not Ionizing Collisions) Foam neutrally initialized but the collisions are switched on. This kind of collisions are not able to ionize the neutrals themselves.

- TC → (Tunnel and Ionizing Collisions)Foam neutrallyinitialized and collisions are switched on. Also this kind of collisions have the possibility to ionize the neutrals.

For all the simulations in this chapter we used a semi-infinite geometry as defined in figure 4.3 since here we are only interested in simulating the behaviour of the foam and not the photon production.

The last section of this chapter is dedicated at investigating if the differences found in this regime are important for the rest of this work, so we will address the case of a pulse with $a_0 = 68$.

5.1 Ionization in collisionless neutral clusters

First, we compare the effect of ionization on a collisionless system. As we can see in figure 5.1 there is very little difference in behaviour between a fully ionized plasma and a neutrally initialized foam. The curves stick together for long and then after a time of the order of $\sim 10^2$ fs separate. We can see that the neutrally initialized case (TNC) transfers more energy into electrons, which is no surprise. A nanostructured foam is characterized by local high electronic density, and fully ionized nanoparticles act like small mirrors. Eventhough their size is roughly one tenth of the laser wavelength, some of the laser is naturally reflected in the interaction. If the foam is already fully ionized (NTNC) the laser sees nanometric mirrors from the beginning, in TNC configuration this is not the case since initially the pulse propagates into a neutral environment. If the foam is made of neutral clusters then the laser can penetrate into the material ionizing progressively the nanoparticles. The front of the pulse does therefore not see immediately a mirror but a mildly ionized medium which is less reflective than a fully ionized configuration. Since the peak intensity of the pulse is ultra-intense ($I_0 > 10^{22}$Wcm^{-2}), and thus the tail intensity becomes very quickly $\gg 10^{14}$Wcm^{-2}, we do not expect this effect to be extremely significant, but a difference can be spotted between the two cases.
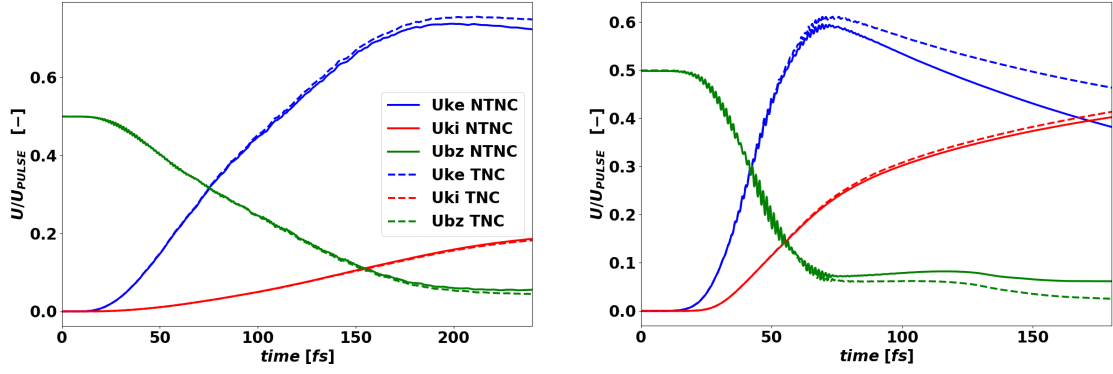
Figure 5.1: Quantitative effect of tunnel ionization on the total energy balance for $a_0 = 15$ and $n_0 = n_c$ (left) and $9n_c$ (right). The fully ionized collisionless behaviour (No Tunnel No Collision - NTNC - solid lines) is compared to the initially neutral foam (Tunnel No Collision - TNC - dashed lines). The plotted quantities are: Electron kinetic energy (uke - blue), Ions kinetic energy (uki - red), and Electromagnetic energy stored in the B_z field (ubz - green).

From a microscopic point of view introducing tunnel ionization slightly increases the particles maximum energy, but even for relatively long times the difference is very small (fig. 5.2).
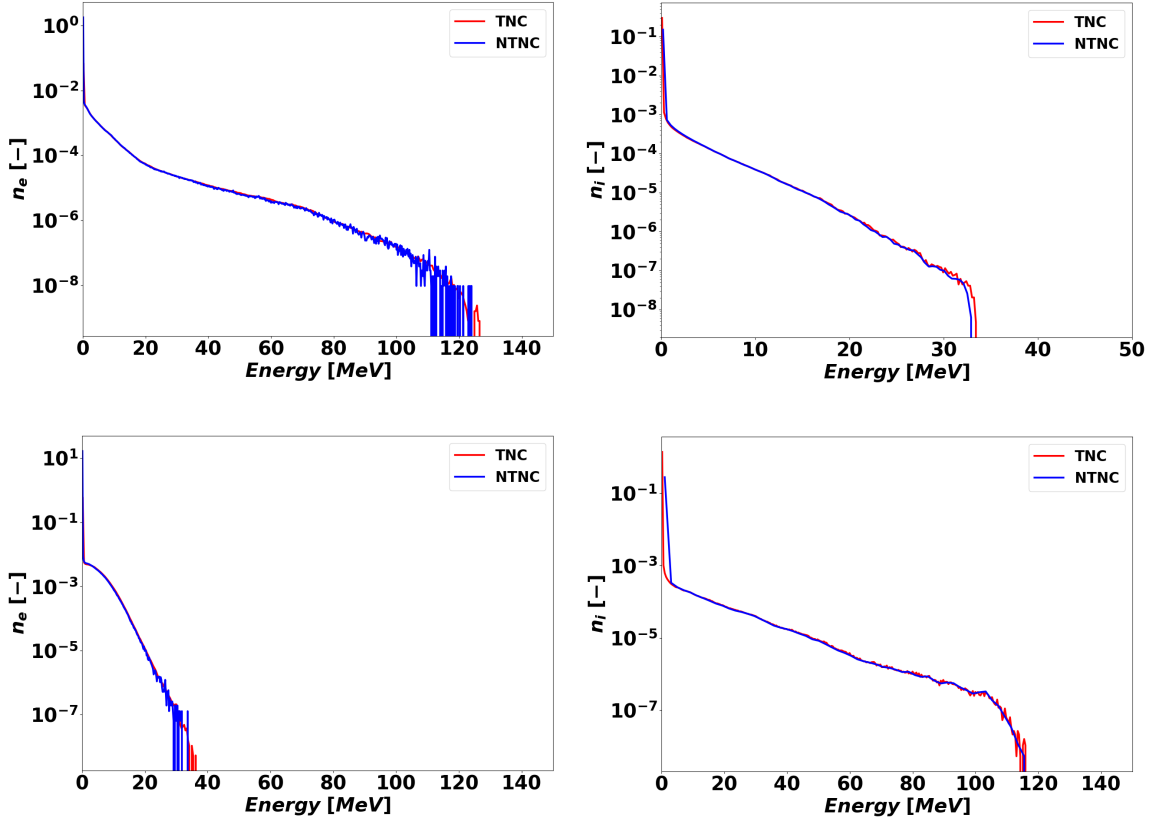
Figure 5.2: Energy spectrum of electrons (left) and ions (right) at $t = 80fs$ for nanostructures of average density $n_0 = n_c$ (top row) and $n_0 = 9n_c$ (bottom row) at $a_0 = 15$.

5.2 Non-ionizing Collisions in neutral nanoclusters

At this point we already suggested the idea that the reason the energy transfer between laser and electrons is more efficient, even if only slightly, is that including ionization processes contributes to lower temporarily the local charge density. One could think that another way of reducing the local charge is to induce the electrons to spread out faster and more evenly in the cluster. One path to achieve this result could also be with collisions. Collisions should force particles with same charge apart, making more difficult to obtain sharp charge density peaks. We know that the higher the temperature the less important collisions are, and often realtivistic plasmas are modelled as collisionless (eq.(3.13)).

In order to see if this phenomenon alone can in some way have any effect on the system we switched on collisions among all species. We do not want the collions to be able to ionize the material yet, so we can focus only on the "spreading" effect. The results are summarized in figure 5.3 . As we can see no difference whatsoever has been found between collisionless and collisional foams. No difference has been found
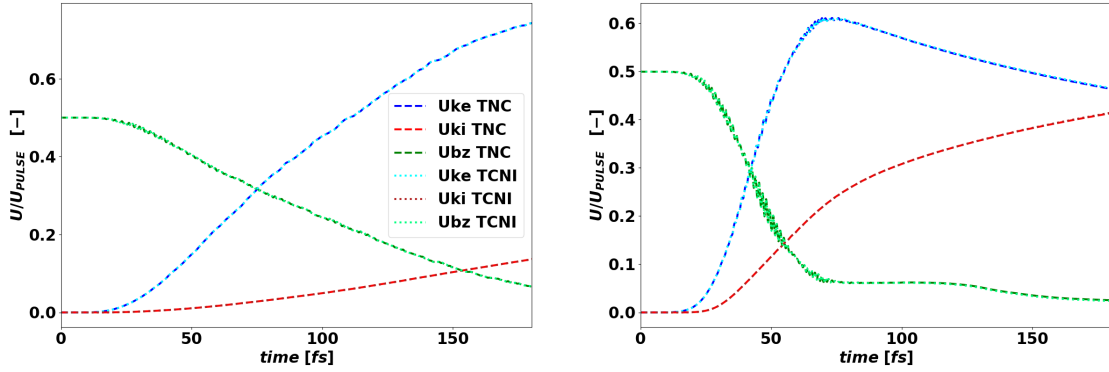
Figure 5.3: Quantitative effect of non-ionizing collisions on the total energy balance of a neutral cluster for $a_0 = 15$ and $n_0 = n_c$ (left) and $9n_c$ (right). The collisionless behaviour (Tunnel No Collision - TNC - dashed lines) is compared to the same system with the addition of non-ionizing collisions among all species (Tunnel Collision Not Ionizing - TCNI - dotted lines). The plotted quantities are: Electron kinetic energy (uke - blue), Ions kinetic energy (uki - red), and Electromagnetic energy stored in the B_z field (ubz - green).

also in the spectra for any time in analysis, pictures are omitted for redundancy. We can conclude that the collisional effect of "spreding" electrons in space is definitely negligible in the regime of interest for this work.

5.3 Ionizing Collisions in neutral nanoclusters

The last case we want to check is when we have both tunnel and collisional ionization switched on. This is also the most expensive configuration for this particular section. As we can clearly see in figure 5.4 we find no difference between the collisional and collisionless cases. No difference has been found also in the spectra for any time in analysis, pictures are omitted for redundancy.

We therefore conclude that collisions are straight-up negligible even for $a_0 = 15$ for the whole range of foam average densities of interest for this work ($n_0 = (1 \div 9)n_c$).
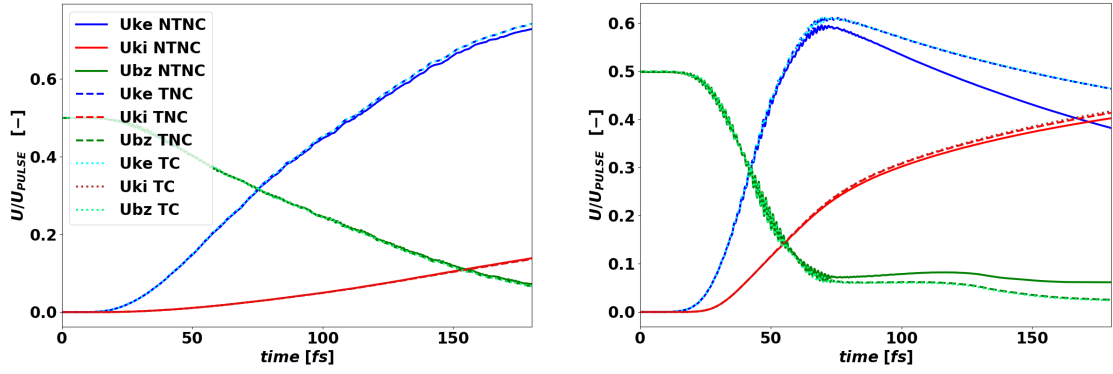
Figure 5.4: Quantitative effect of collisional and tunnel ionization on the total energy balance of a neutral cluster for $a_0 = 15$ and $n_0 = n_c$ (left) and $9n_c$ (right). The complete system with both tunnel and collisional ionization (TC - dotted lines) is compare with previous cases. The plotted quantities are: Electron kinetic energy (uke - blue), Ions kinetic energy (uki - red), and Electromagnetic energy stored in the B_z field (ubz - green).

We are left to check if for higher laser intensities the tunnel ionization effect tends to vanish or is worth modelling.

5.4   Tunnelling for higher intensities

The case with $a_0 = 15$ and average density $n_0 = n_c$ shows no significant changes with or without tunnel ionization, and we expect the difference to only become smaller increasing the pulse intensity. For these reasons we will only test the higher density $n_0 = 9n_c$ at $a_0 = 68$ corresponding to our lowest intensity, and so the potentially most affected case. As we can see in figure 5.5 the foam behaviour is a middleground between the previous cases at $a_0 = 15$, and a reason for this can be found in the opacity factor $\bar{n} = n_0/\sqrt{1 + a_0^2/2}$. We know from work [23] [29] that the processes at play in the foam depend heavily on this factor $\bar{n}$, in particular systems with similar opacity factor tends to behave similarly regardless of the specific value of laser intensity or average electronic density. Computing this quantity for the three cases we get:

$$a_0 = 15, n_0 = 1 \rightarrow \bar{n} \approx 0.09$$

$$a_0 = 15, n_0 = 9 \rightarrow \bar{n} \approx 0.85$$

$$a_0 = 68, n_0 = 9 \rightarrow \bar{n} \approx 0.19$$

We can see how the third case is in between the other two but more shifted towards the first, and this affects the global behaviour of the system.
  Overall we can say that tunnel ionization does not play a huge role in the system until very late in the simulation, at a time for which the pulse would be already reflected by the mirror in our main set-up. To further strengthen this point we look at the energy spectra of the particles at time $t = 80$fs in figure 5.6. We can see how barely no difference can be appreciated here.
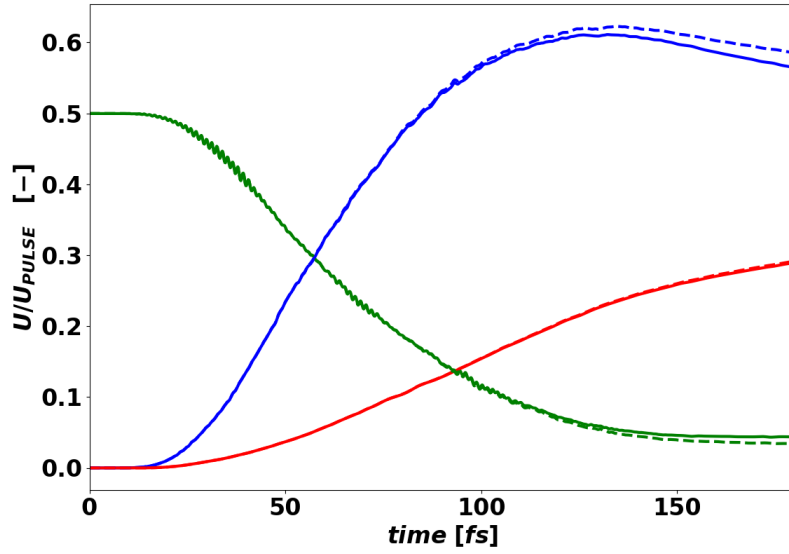
Figure 5.5: Quantitative effect of tunnel ionization on the total energy balance for $a_0 = 68$ and $n_0 = 9n_c$. The fully ionized collisionless behaviour (No Tunnel No Collision - NTNC - solid lines) is compared to the nuetrally initialized foam (Tunnel No Collision - TNC - dashed lines). The plotted quantities are: Electron kinetic energy (uke - blue), Ions kinetic energy (uki - red), and Electromagnetic energy stored in the B_z field (ubz - green).
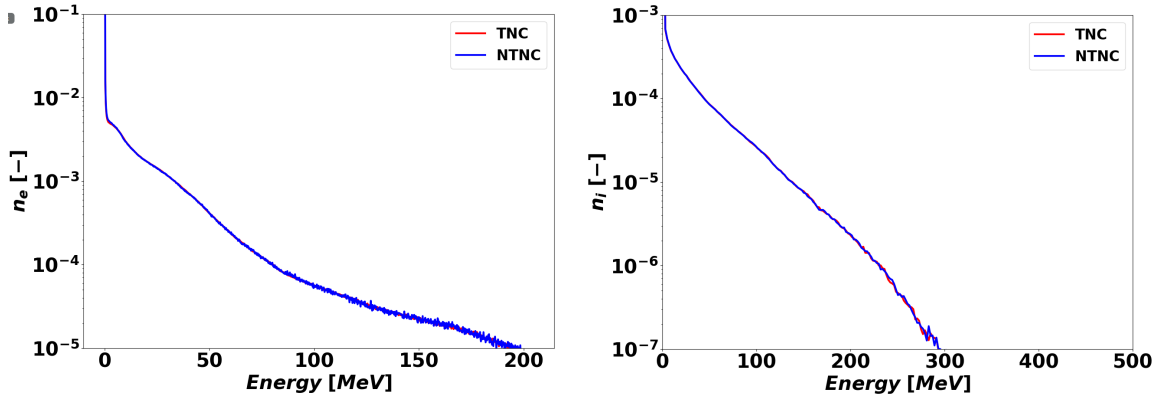
Figure 5.6: Energy spectrum of electrons (left) and ions (right) for nanostructures of average density $n_0 = 9n_c$ at $a_0 = 68$.

5.5 Conclusions on tunnelling and collisions

In this chapter we looked for the effect of both collisions and tunnell ionization on the system dynamics. We observed that collisions play a totally negligible role and without esitation we will never consider them in the modelling in this work. Less trivial is the ionization effect.

We saw in figure 5.1 that tunnelling can be relevant for higher densities, but as the density decreases or the laser intensity increases becomes less and less important. For the frame and the regimes of this work the impact observed can be considered negligible (fig.5.6).

Analyzing the performances we observed that using collisions increases the computa-

tional time by a value often around 100%.

Tunnel ionization instead showed a more irregular behaviour, and estimating its effect on performances turned out to be not as trivial as we thought. Usually switching on the field ionization module results in an increase in computational time ($40\% \div 70\%$) but in some cases increased the efficiency of the code. Initializing a target as neutral is indeed beneficial at the beginning since the number of macroparticle in the box is halved with respect to an already fully ionized plasma (ions and electrons are one neutral particle). Nevertheless at runtime the number of macroparticles increases, but overall number of macroparticles should remain lower than a fully ionized plasma. On the other hand, using an additional Monte Carlo module is always heavier for the code as a whole. These two effects concurr and the effect on performance is relatively unpredictable from the data we collected.

A final remark should be done on the quantitative reliability of 2D PIC simulations. In particular we stress again the fact that 2D systems are not perfectly representative of a complex 3D system. As shown in previous work [20][30], 2D simulations result in an overestimation of the energy output. It is more clear now that a quantitative error of less than few % in 2D results is even less significant knowing that a quantitative difference of the order of $\sim 10 \div 20\%$ is usually observed when switching to 3D simulations.

For everything we just said we chose to initialize the target as a fully ionized plasma and neglect all tunnelling and collisional effect.

Chapter 6

Pulse propagation in foam-based targets

6.1 Plasma lense effect

Near critical density plasmas are able to efficiently focus laser pulses and particle beams. This phenomenon is called "Plasma lense" or "Self-focusing" and has been studied exensively in [60][61] in order to achieve higher intensities for various purposes. As we can see in figure 6.1 this effect is well observed in our simulations. The pulse focuses itself way beyond the Gaussian limit in vacuum, reaches a new waist and then defocuses. Depending on the average density n_0, structure of the plasma and laser intensity, we observe that the maximum amplitude of the laser field (i.e. B_Z) is increased by a factor of roughly $B_Z^{MAX}/a_0 \sim 1.5 \div 2.5$.

In order to better visulalize the self-focusing effect we will always simulate a semi-
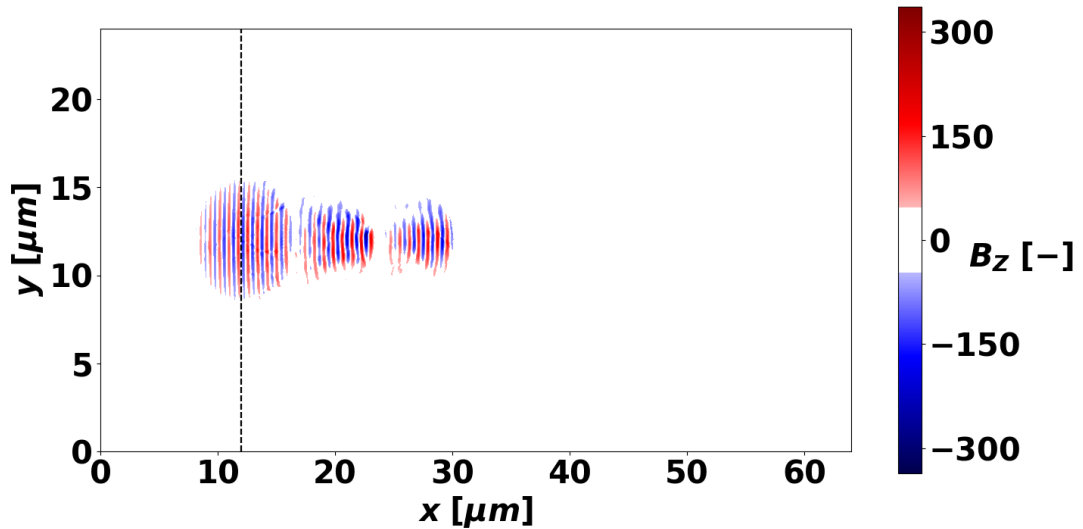
Figure 6.1: Example of self-focusing of the laser pulse inside a homogeneous NCD plasma. In colors is the magnetic field normalized amplitude at three different times, respectively 23, 52, and 79fs after the beginning of the interaction. The vertical dashed line represents the beginning of the NCD foam. The initial peak amplitude of the pulse is in this case $a_0 = 166$, the density is $n_0 = 6n_c$. The snapshots are taken hiding the channel magnetic field that is indeed created, in order to have a clearer view of the pulse.

infinite foam (fig.4.3) in this section.

We observe that the larger the average density n_0, the bigger will be the lense effect.
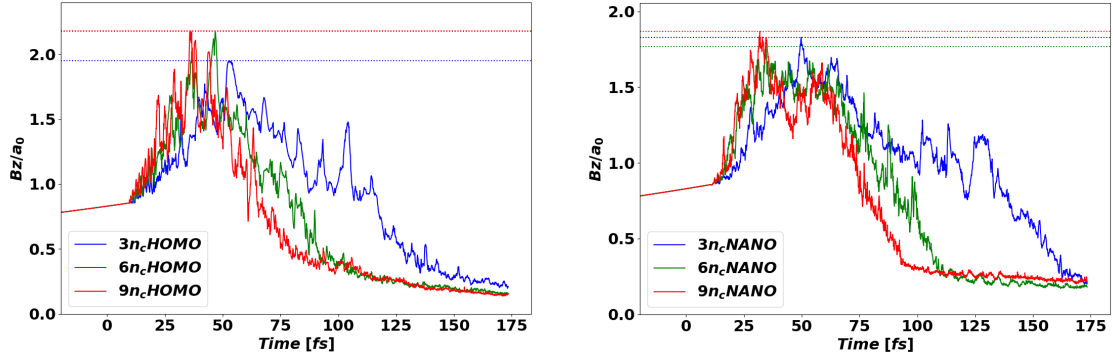
Figure 6.2: Maximum value of the field B_z recorded in the box for each timestep normalized to the initial laser amplitude a_0. The slight ramp at the beginning is just the standard focusing in Gaussian propagation, with the focal length fixed at the beginning of the foam.

We also need to consider the fact that increasing the density (but still remaining in NCD conditions) will increase the plasma absorption (and reflection) draining the pulse from its energy, decreasing the field amplitude faster over time. We can see the results of these two phenomena in figure 6.2 for three different n_0 with $a_0 = 68$ and homogeneous (left) or nanostructured foam (right). The decreasing of the field after the maximum is a sign of both defocusing and absorption. We can see that for higher densities the process of focusing/defocusing seems to be quicker. This is true for both homogeneous and nanostructured foam, although for the latter seems that the density does not really affects the maximum reached value (dashed lines).

Changing the approach we could look at how the energy spread of the pulse varies during the propagation. The pulse is compressed into a smaller and smaller region also concentrating its energy. Of course field amplitude and energy density are not independent, since it is well know that this latter reads $u = \epsilon E^2 = B^2/\mu$ with ϵ and μ the dielectric and magnetic permittivity of the medium. In figure 6.3 we can notice how the energy stored in the electromagnetic fields is progressively focused. In order to obtain that figure we must find for each timestep the x_{MAX} coordinate of the maximum value for the field, and we look at the electromagnetic energy distribution along the transverse direction $u(x_{MAX}, y)$. From this curve, going in direction $y > 0$ we can define two points with coordinates that we will call y_{25} and y_{75}. This points are defined such that the area under the curve (energy) for $0 < y < y_{25}$ is 25% of the total area (total energy), and the area under the curve (energy) for $0 < y < y_{75}$ is 75% of the total area (total energy). This means that in the region of space inside $y_{25} < y < y_{75}$ is enclosed 50% of the total energy. At the end we obtain two points y_{25} and y_{75} for each timestep, which once plotted vs time we obtain figure 6.3. We can notice that the nanostructured case results in more asymmetrical behaviour. This is only caused by the intrinsic chaos of the structure itself. In comparison the homogeneous foam results in more symmetry. It is due to point out that the propagation of the pulse in NCD plasma is not a stable phenomenon and at its front filamentation can be observed, a little asymmetry in the data is then expected.

One can also think of plotting the same point series but vs x_{MAX} instead of time to see the position in space of the maximum of the field varying, but the results are very similar and are omitted for redundancy.
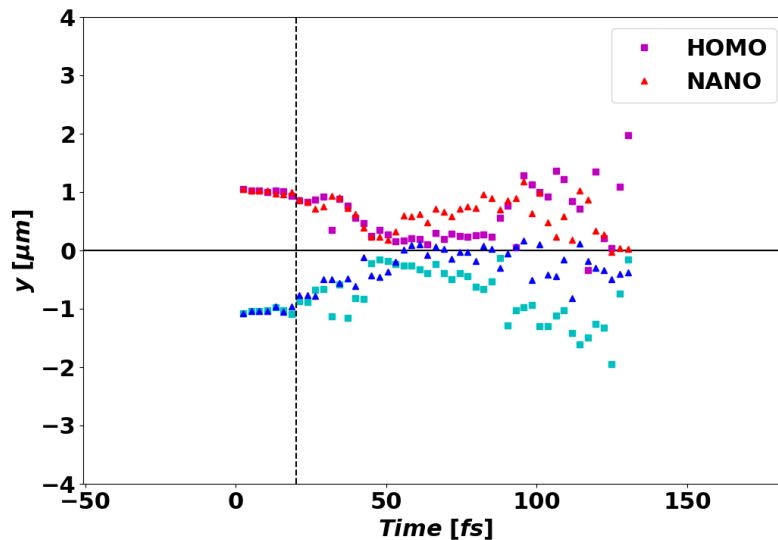
Figure 6.3: Example of self focusing and defocusing inside a NCD plasma of $n_0 = 3n_c$ and $a_0 = 68$ for homogeneous (green (y_{25}) and purple (y_{75}) squares) and nanostructured (blue (y_{25}) and red (y_{75}) triangles) foam. Vertical dashed line represents the moment at which the maximum of the pulse enters the foam. The asymmetry of the NANO configuration is due to its intrisic chaotic structure.

As we showed in section 1.2.1 in order to achieve greater γ emission we should increse the quantum parameter χ_e. We remember also that $\chi_e \propto \gamma_e|\boldsymbol{B}|$, then maximizing the field amplitude is crucial in order to maximize χ_e and thus photon emission.

6.2   Mirror effect

When interacting with a high density material, a laser pulse is reflected and for a brief window of time the incident and the reflected wave interfere with each other. Throughout this work we observed an increase of the field amplitude during reflection by a factor $1.5 \div 2.0$ which is in line with previous works [52][53][55].
In order to maximize photon emission we need to have a foam layer of thickness L_F in front of a mirror so that we can exploit the laser-plasma coupling to accelerate electrons, and then induce a radiation emission thanks to the temporary doubled (almost) field. In order to do that we need to find the configuration which allows us to maximize the field during the reflection. The maximum amplification is achieved if the reflected field is the highest possible, so we use a semi-infinite foam to find the L_F which would allows laser to arrive onto the mirror with the maximum possible field.
 This is done by considering the field amplitude at $y = 0$ for each timestep, and following the pulse along the $x - axis$ in time. This kind of diagnostic is called *streak* and is named after the *streak-camera*. In order to follow the pulse we decided to plot the streak of $B_Z^2(x, 0, t)$, as shown in figure 6.4. We can now check the corrispondance with figure 6.2, and find out the space coordinate of the maximum value for the field amplitude, all in one diagnostic.
We chose to use the square of the field and not the field itself to make sure we do not
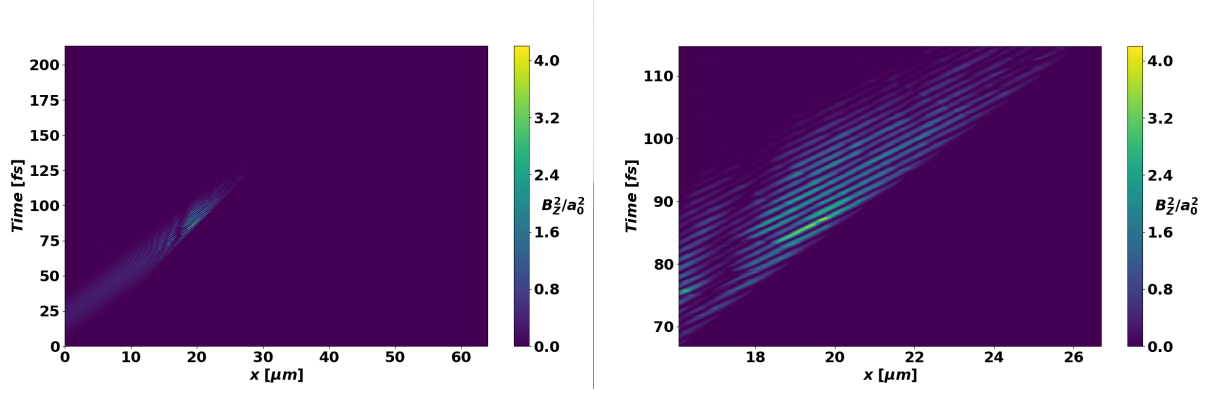
Figure 6.4: Streak of $B_z^2(x,0,t)/a_0^2$, in all the box for all timesteps (left) and, the same picture but magnified in order to better distiguish the region of maximum focusing (right). The y coordinate is set to be in the middle of the box

loose negatives values, and of course every field amplitude has been normalized to a_0^2.
  Now we can directly pinpoint the best penetration length in order to maximize the self
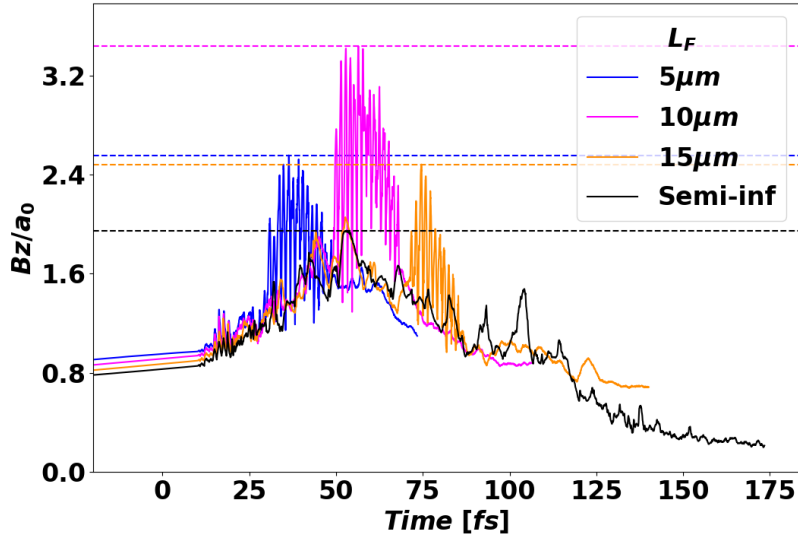
Figure 6.5: Effect of the mirror on the propagation of the pulse in the system. Figure obtained with the same method of figure 6.2 but in four different simulation differing only for the foam length put prior the substrate (mirror). The parameters for this specific example are: $n_0 = 3n_c$, $a_0 = 68$, homogeneous foam. L_{focus} for these parameters is measured at about 10μm, so in the figure we plotted $L_F = \{5, 10, 15\}\mu$m and a semi-infinite foam without a substrate (black) for reference.

focusing. Our job is now to use this information to enhance electronic radiation emission. For each density and each intensity we measured the propagation length for the most efficient focusing effect L_{focus} which will result different from the optimal length for γ-photon generation. In general for each L_{focus} we ran a batch of $4 \div 10$ simulations with foam of lengths roughly like: $\{L_{focus}/2, L_{focus}, 3L_{focus}/2, 2L_{focus}, 3L_{focus}\}$ and few more cases considered of interest. As we can observe in figure 6.5 the reflection acts as we expect increasing of a factor $1.5 \div 2.0$ the field in the system. The configuration with the foam length L_F equal to the focusing length L_{focus} is

indeed the one reaching the highest maximum field amplitude, as we expected. How this will translate into radiation emission is topic for the next chapter.

Interesting is also to look at the focusing effect for each n_0 and a_0 as we show in figure
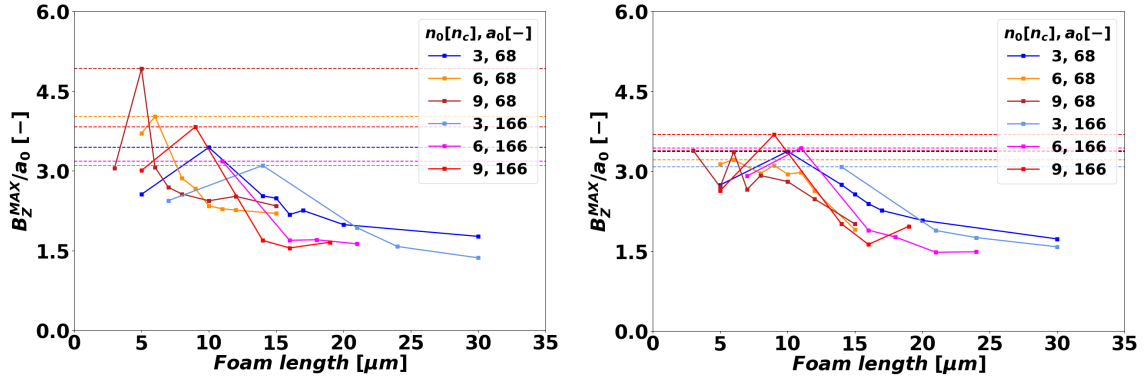
Figure 6.6: Maximum normalized field amplitude normalized to a_0 recorded in the box vs foam length of the simulation for homogeneous (left) and nanostructured (right). The same process of figure 6.5 is applied here but only the maximum values (dashed lines in the referenced figure) are kept and plotted againt the respective foam lenghts L_F (squares). Different colors refer to the different average densities $n_0 = \{3, 6, 9\}n_c$.

6.6. We confirm that if all the other parameters are the same then higher average density leads to a stronger and quicker focusing effect. It should be pointed out the fact that for $n_0 = 9n_c$ we manage to reach an amplification factor of over 4.5 which is the highest in our work. Nanostructured targets follow roughly the behaviour of the homogeneous cases, although the trend is less clear and the amplification is overall less efficient. We will address it many times but nanostructures are complex systems characterized not only by an average density like a homogeneous foam is. Changing the filling factor and the nanoclusters diameter also changes its properties as shown in [52]. Henceforth we need to have the homogeneous foam cases as a comparison in order to help us better interpret the nanostructured cases. An extension of this work studying how all the nanostructure parameters on a 3D foam influence the macroscopic and microscopic phenomena would be extremely useful and extremely important to predict experimental results.

6.3 Conclusions on field amplifications mechanisms

In this chapter we analyzed two independent processes that we are going to exploit to increase the field amplitude in the system: self-focusing, and reflection. The first focuses the pulse surpassing its Gaussian limit, amplifing the maximum field reached by a factor of the order of 2 (fig.6.2). The second yields from the self-interference of the pulse with itself when is reflected by a solid density substrate (mirror), and is also responsible for a factor of the order of 2 in the filed amplification (fig.6.5). The sum of these two effects makes us able to increase the maximum field inside the target of a factor of the order of 4 and thus of a factor of the order of 16 in intensity. We should remark that the lowest intensity we are going to consider is already 10^{22}Wcm^{-2} so increasing by one order of magnitude we reach a laser intensity of the order of 10^{23}Wcm^{-2} on target. In the next chapter we will focus on how everything we said up to this point is translated into photon production.

Chapter 7

Photon production

Here we will discuss the possible production of γ-photons with the available Apollon peak power of 1PW ($a_0 = 68$) and 3PW ($a_0 = 166$). In this chapter the laser parameters are those summarized in column "A" and "B" in table 4.1.

We will again remark that all the generated photons are only from synchrotron-like emission, all other processes (i.e. Bremsstrahlung) are not considered here but are assumed to be negligible in this regimes [4]. Neglected are also all photon-photon interaction such as pair production via Breit-Wheeler (BW) since we are not interested in positron production yet, we will leave this topic for future studies.

We will first look at the macroscopic dynamics of the system, addressing the energy transfer among: electromagnetic fields, electrons, ions, and photons.

Afterwards we will discuss the properties of the electrons and how those are related to the photons dynamics. Finally we will characterize the photons and their properties. The physical modelling of photon production has been summarized in chapter 1, while the numerical simulation tools are described in section 3.8.2.

7.1 Conversion efficiency

7.1.1 Energy transfer in the system

The first effect of the pulse propagation inside the foam is to increase the total electron kinetic energy, which macroscopically translates into an energy transfer from the laser to the electrons. The laser will interact always and only directly with the electrons, and will be the electrons which in turn radiate, producing photons. Since all photon-photon interaction are neglected, the laser cannot interact directly with other photons, thus the electrons are always the only first-hand receiver of laser energy, which then radiate it into photons or transfer it to ions.

For all intensities and densities we observed that the energy absorbed by electrons is almost linear in time during the laser propagation into the foam, and so is also the energy radiated away in photons (fig. 7.1) . At the moment of reflection (shaded region) we can see how all curves change behaviour, in particular the electrons kinetic energy stops its growth, and the radiated energy (photon energy - U_{rad}) increases rapidly. We would like to point out how for the radiated energy we pass from a ramp-like curve (foam propagation) to a *burst* (reflection), and then to a final saturation phase. From now on we will refer to these three behaviours as: *ramp*, *burst* and, *afterglow* respectively. In all three we find the same physics at play but in very different contexts, henceforth the properties of both particles and radiation have

different characteristics that we will try to explain. It should be pointed out how the sum of $ramp(\Delta U_R)$, $burst(\Delta U_B)$, and $afterglow(\Delta U_A)$, gives the total radiated energy so that at the end of the simulation $U_{rad} = \Delta U_A + \Delta U_B + \Delta U_R$.
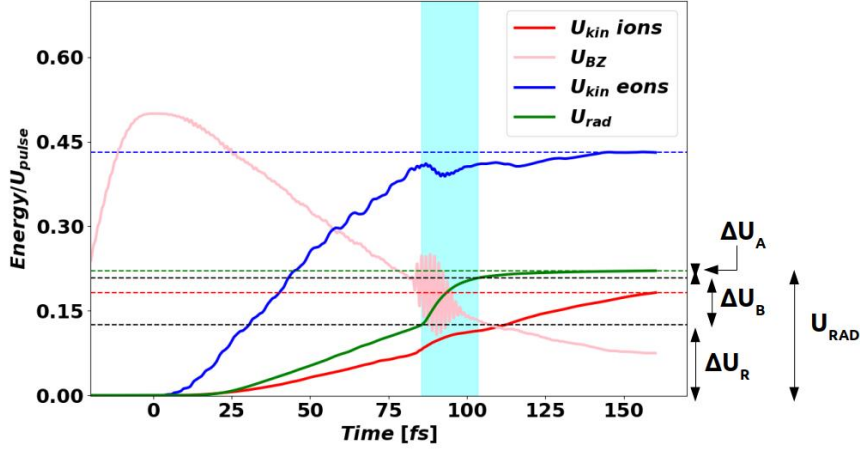
Figure 7.1: Typical evolution of the fraction of laser energy that is converted to: electrons kinetic energy (U_{kin} eon - blue), ions kinetic energy (U_{kin} ion - red), photon energy (U_{rad} - green), and energy stored in the field B_Z (U_{BZ} - pink). We can see the rapid energy conversion to radiation during the reflections (shaded area). The energy stored in the B_Z field is a good indicator of half of the energy still in the pulse at each timestep (the other half is stored in E_y). It should be noticed how the total radiated energy $U_{rad} = \Delta U_A + \Delta U_B + \Delta U_R$.

One can have immediately two ideas to exploit the information just given, in order to enhance the total energy emitted in photons. The first would be that since during the propagation in the foam U_{rad} has a roughly constant slope, having a really long foam would be beneficial. This is shown later on not to be convenient, instead, having a big *burst* is often better than having a long *ramp*. The second idea would be, on the other hand, to say that since quantitatively the *burst* is often between $40 \div 70\%$ of the entire output of radiated energy, the best solution is to look for ways to increase its magnitude forgetting completely about the *ramp*. This approach is also ineffecient too, since the latter has still great importance as shown in fig. 7.2. Looking at this latter figure one can see that the magnitude of the burst is larger for $L_F = 6\mu$m but the overall highest conversion is achieved for foams of around 10μm while for longer foams it lowers, proving how important is to look for a good combination of *ramp* and *burst* in order to obtain the highest photon energy output. The *afterglow* gives often less than $10 \div 20\%$ of the total photon energy, thus is much less interesting than *ramp* and *burst*.

Even for relatively long foams like the 15μm (fig. 7.2 - green line) the *ramp* has more or less constant slope while the *burst* magnitude has less trivial trend. In the next section we will try to break down how the relative importance of those three components changes with our parameters.

It is due now to point out that we simulated situations with several parameters which gave a wide range of results, some systems (usually very thick or very thin foams) behave in substantially different ways from the rest. In order to correctly discuss the dependence of each quantity from the parameters it is necessary to use
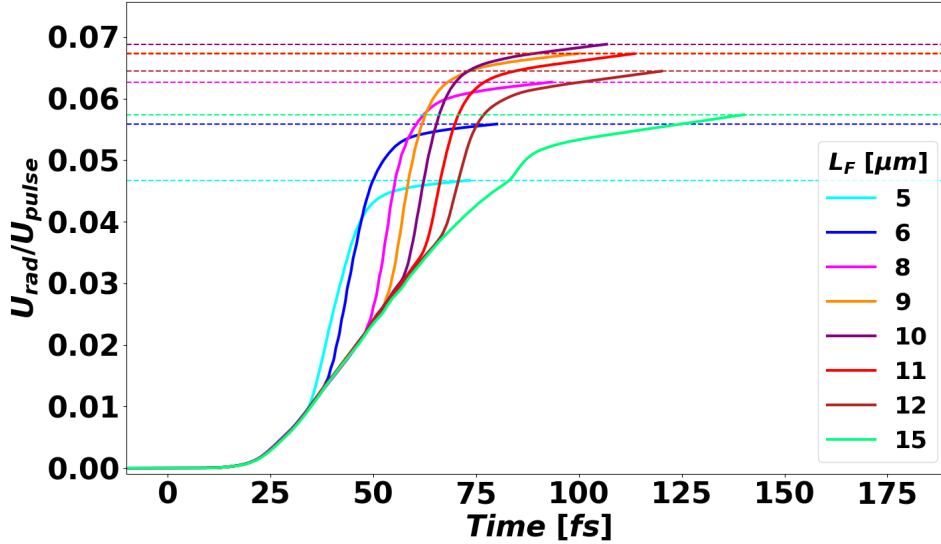
Figure 7.2: radiated energy evolution in time for $n_0 = 6n_c$, $a_0 = 68$, and different foam thickness with homogeneous structure.

systematic and coherent definitions. In some cases we recorded a different behaviour of one configuration from all other similar ones. Usually this comes from a very intuitive and almost trivial reason, for example sometimes the cases with the thickest foams do not have a clear *burst* or the ones with the thinnest foams do not have a proper *ramp*. Sometimes in order to clearly see a trend it is necessary to compare only physical systems which behave in the same way excluding systems which are too different from the others (i.e. a system in which there is no *burst* but only a very long *ramp* instead). Therefore occasionally some points will not be shown in the pictures, because they would not be significant comparisons to the other systems. We will try to always show all the data when appropriate.

7.1.2   Dependence on target geometry and density

If we look only at the overall conversion efficiency defined as U_{rad}/U_{pulse} (fig.7.3) we notice that its maximum value is not achieved for a foam thickness that granted the maximum field amplitude (fig.6.6). Previously we proposed the idea that reflecting the pulse at its maximum focusing would have been the best way of producing photons, but the data suggest that best point in which reflect the pulse is actually somewhere after the point of maximum focusing, where the field amplitude is not at its maximum possible value. The field amplitude is still an important component but results suggest that is not the only relevant one.

From the curves relative to $a_0 = 68$ in homogeneous targets we are brought to think that the lower the density, and the bigger the conversion efficiency reached. The curves for $a_0 = 166$ suggest the opposite instead, implying that a configuration "too transparent" is not really an efficient choice. The hypothesis we made right now is that there is an optimum between transparency and opacity for which the maximum convertion efficiency can be reached. This value we can estimate being around the value reached for $a_0 = 166$ with $n_0 = 6 \div 9n_c$, and $a_0 = 68$ with $n_0 = 3n_c$. The value of opacity factor estimated is in the interval $0.05 \leq \overline{n}c \leq 0.08$ which also correspond to an optimal thickness in the interval $14\mu m \leq L_F \leq 17\mu m$ for all the three cases mentioned.

The behaviour of the nanostructured targets is different and less predictable. We showed previously in this work how the nanostructure influences the focusing/defocusing dynamics in the target, so further investigation is needed to draw conclusions in these cases. All our attempts in order to quantify this behaviour gave unfitting results, further theoretical modelling is needed in order to coherently explain these phenomena.
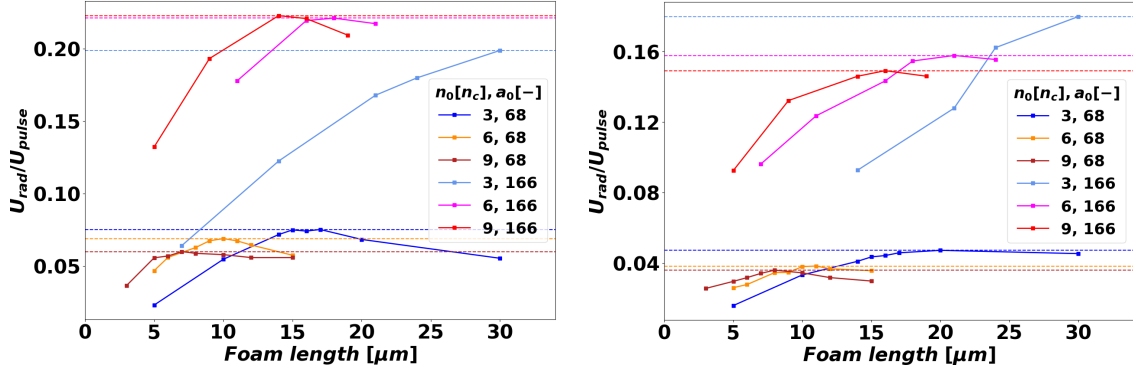
Figure 7.3: Conversion efficency in radiation vs foam thickness for homogeneous (left) and nanostructured (right) cases, at the end of the simulation. Different colors refer to the different densities $n_0 = \{3, 6, 9\}n_c$ and different laser parameter $a_0 = \{68, 166\}$. We can see how the energy converted into photons reaches beyond 7% of the laser energy with $a_0 = 68$ and above 22% for $a_0 = 166$.

Looking at figure 7.4 we can decompose the total conversion efficiency into the three components *ramp*, *burst* and *afterglow*. We should immediately notice that in the first row representing the *ramp* (HOMO on the left and NANO on the right) the curves are roughly linear with the foam length.

These facts will be discussed more in section 7.2.1 and will help us understand the microscopic mechanisms underneath.

The *ramp* slope grows with the average density n_0 (fig.7.4) suggesting a dependence of the *ramp* slope on the focusing dynamics (i.e. how quickly the process of focusing/defocusing happens). This assumption is reinforced by the behaviour of both *burst* and *afterglow*, the first in particular with its *bell-like* shape shows that if the density increases then the condition in order to have the maximum *burst* magnitude are met and lost quicker. Because of what just said we expect a strong correlation between n_0 (or $\overline{n}$) and all macroscopic phenomena.

We should remark now how for $a_0 = 68$ (1PW) we obtained a conversion efficiency above 5% for most cases, reaching a maximum at roughly 7% for $n_0 = 3n_c$ and $L_F = 17\mu$m. This is far beyond what we expected at the beginning of this work and what obtained in previous works [52][55] which suggested the possibility to reach $\sim 1\%$. For a more powerful laser ($a_0 = 166$, 3PW) we obtain up to 22% of converted energy from the laser to photons. These values are incredibly promising and they should be focus of further studies, in particular, 3D3V simulations are to be ran in order to acquire more quantitive resuluts for experimental design. We expect that with the final Apollon power of ≈ 7.5PW will be possibile to reach even higher values.
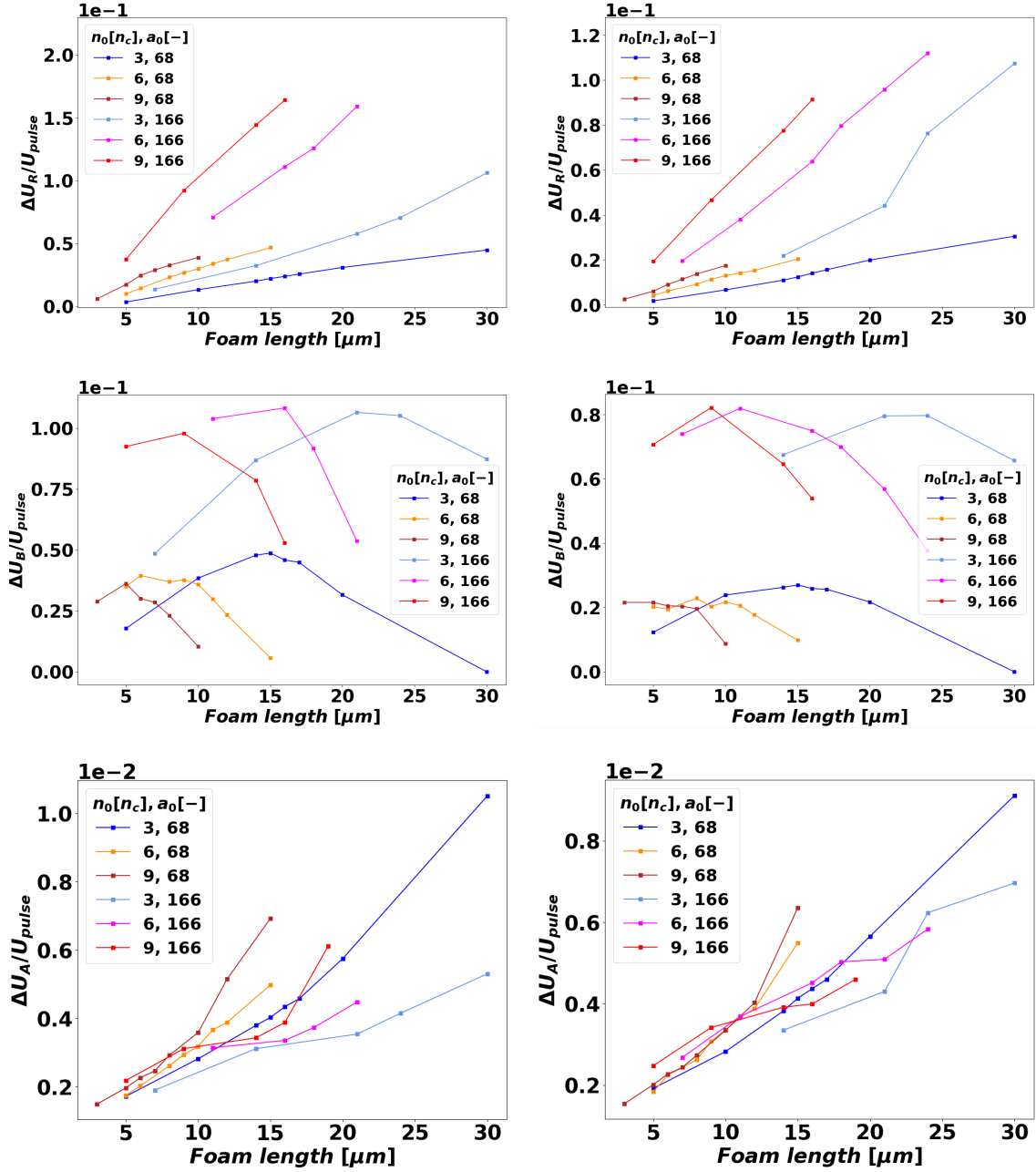
Figure 7.4: Magnitude of respectively *ramp* (top row), *burst* (center row) and *afterglow* (bottom row) for homogeneous (left column) and nanostructured (right column). The magnitude is measured as the fraction of radiated energy over the total pulse energy. The *burst* is generally the most important part, while the *afterglow* is usually less than a tenth of *burst* and *ramp* combined.

7.1.3   Dependence on target number thickness

Up to now the results appear to be function of average density (n_0), laser parameter (a_0), and geometry (L_F). As we have already seen, there is a parameter used in previous works concerning foams [20][29][23] which contains the first two items in the list. The opacity factor $\overline{n}$, defined in eq.(4.23) as $\overline{n} = n_0/\sqrt{1 + a_0^2/2}$ is a parameter which takes into account the *relativistic transparency* of the medium in which the laser is propagating. Expressing the results in function of this parameter could

be interesting, but we can include also the last parameter on the list: L_F. The *mass thickness* is a quantity defined as $(mass\ density) \times thickness$ of a specific medium. Since all simulations have the same materials for the target, we do not really care about the mass density, but rather the charge density. Furthermore, since all electrons have the same charge, we are interested only in the number density of electrons. We can then define a parameter $\overline{\mu}$ as:

$$\overline{\mu} \equiv \overline{n}L_F = \frac{n_0}{\sqrt{1 + \frac{a_0^2}{2}}}L_F. \tag{7.1}$$

Its dimension are the one of a number density (l^{-3}) times a length, which give the dimension of a surface density (l^{-2}).
In fig. 7.5 we show the fraction of the pulse energy emitted in photons during the *ramp* in function of $\overline{\mu}/n_c$. As we can see the curves with same a_0 tend to come together suggesting that all the information related to n_0 and L_F are contained in $\overline{\mu}$.
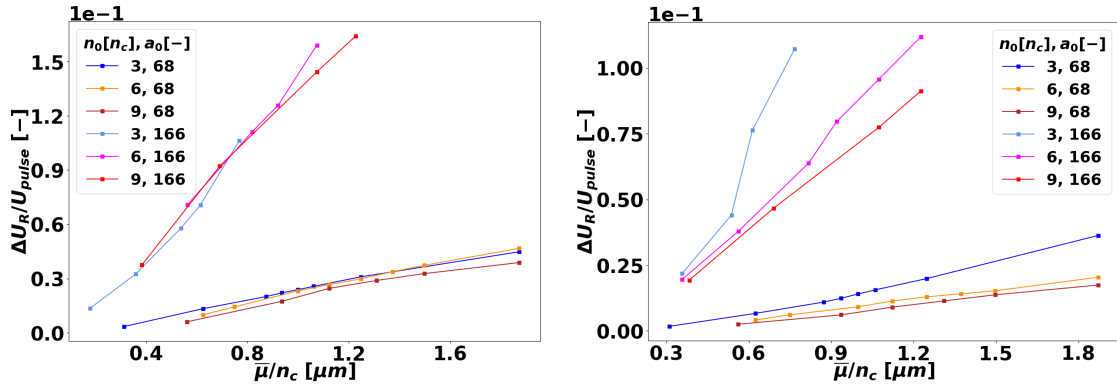
Figure 7.5: Conversion efficency in radiation during the *ramp* ($\Delta U_R/U_{pulse}$) vs normalized number thickness ($\overline{\mu}/n_c$) for homogeneous (left) and nanostructured (right) cases, at the end of the simulation. Different colors refer to the different densities $n_0 = \{3, 6, 9\}n_c$ and different laser parameter $a_0 = \{68, 166\}$. We can see how the curves obtained at the same a_0 tend to overlap regardless of the value of n_0.

Since the cases at $a_0 = 166$ seems to radiate much more than the ones at $a_0 = 68$ we can infer that the dependence on the field strenght is not completely described by the parameter $\overline{\mu}$. As we have seen in chapter 1, the power emitted in photons can be very convoluted in complex systems. Maybe even with the same value of $\overline{\mu}$, the actual magnitude of the laser intensity is important to determine the behaviour of the system. We therefore repropose the same plot but we normalize the fraction of energy radaited away with a factor $a_0^2 \propto I_0$ (fig. 7.6).

We can see how all the curves now tend to overlap suggesting that the radiating behaviour during the *ramp* can be roughly related to the only parameter $\overline{\mu}a_0^2 \propto \overline{\mu}I_0$. What happens in the *burst* is more complicated because it is function not only of the initial intensity of the laser I_0 (or normalized amplitude a_0), but also of the specific condition at the reflection. It is therefore more complicated to propose a simple scaling to describe the *burst* behaviour. Using the same approach as for figure 7.6 we obtain figure 7.7, which shows a tendency of the curves with same a_0 to gather regardless of the specific value of n_0, suggesting that all the information about the
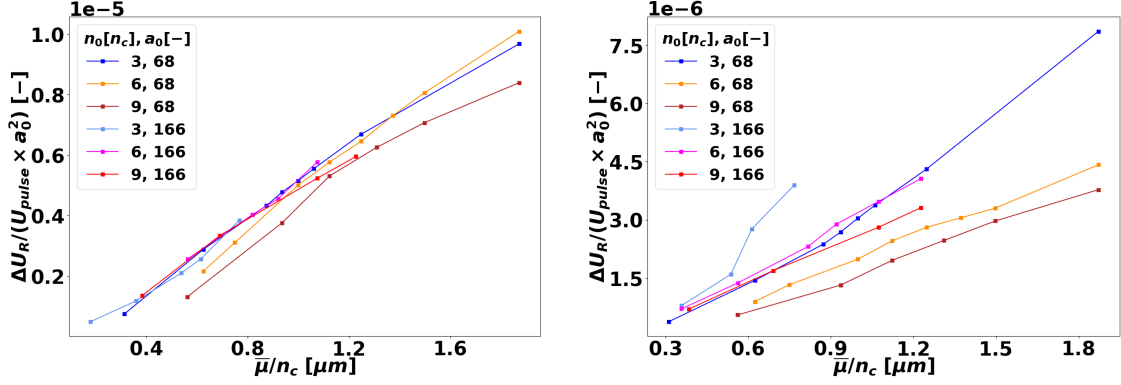
Figure 7.6: Conversion efficency in radiation during the *ramp* ($\Delta U_R/U_{pulse}$) divided by a_0^2 vs normalized number thickness ($\overline{\mu}/n_c$) for homogeneous (left) and nanostructured (right) cases, at the end of the simulation. Different colors refer to the different densities $n_0 = \{3, 6, 9\}n_c$ and different laser parameter $a_0 = \{68, 166\}$. We can see how all the curves tend to overlap regardless of the value of n_0 or a_0.

target properties are contained into the parameter $\overline{\mu}a_0^2 \propto \overline{\mu}I_0$.
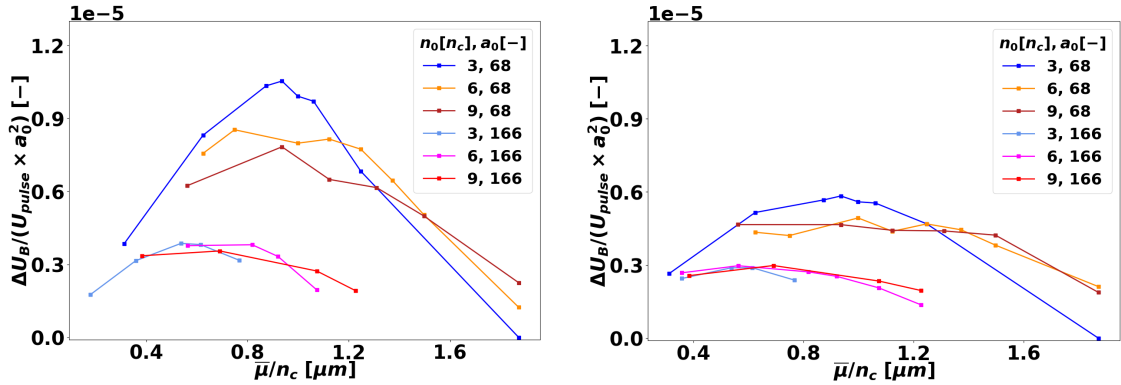
Figure 7.7: Conversion efficency in radiation during the *burst* ($\Delta U_B/U_{pulse}$) divided by a_0^2 vs normalized number thickness ($\overline{\mu}/n_c$) for homogeneous (left) and nanostructured (right) cases, at the end of the simulation. Different colors refer to the different densities $n_0 = \{3, 6, 9\}n_c$ and different laser parameter $a_0 = \{68, 166\}$. We can see how the curves obtained at the same a_0 tend to overlap regardless of the value of n_0.

In general the behaviour of the nanostructured targets is less predictable but still follows, even if less effectively, the principle shown in the homogeneous cases. It was shown in [53] that nanostructures tend to behave more and more like homogeneous plasmas the smaller the size of the nanoparticles, it is therefore reasonable to expect a difference in the evolution of a nanostructured target with respect to a uniform one. Real foams can have characteristic dimension much smaller than 80nm like it was used in this work, thus we expect that real foams ($\delta x \sim 10$nm) can in principle behave more similarly to the homogeneous case than the foams simulated in this work. A parametric study on the effect of the characteristic dimension of the nanosphere δx on the radiation properties would be rather useful in order to gain more insights on this topic.

7.2 Electron microscopic properties

Now that we have a good grasp of the macroscopic behaviour of the system, we will discuss the microscopic properties of the electrons.
First we will look at where the photons are emitted, by looking at where the most active electrons are in the system. Then we will try to pinpoint the region in space for each one of *ramp*, *burst*, and *afterglow*. Lastly we will characterize the electrons in term of their energy γ_e and quantum parameter χ_e in order highlight the difference between *ramp* and *burst*.

7.2.1 Radiating electron location

Up until now we looked at the evolution of some macroquantities, like the radiated energy, in time but we have not said anything about their space evolution. A useful information would be knowing where in the system the photons are produced, so we can better focus our attention. We can very easily plot a map of the estimated classical power emitted by the electrons using the relation $P_{cl} = P_\alpha \chi_e^2$ defined in eq.(1.42). We can use the classical formula to estimate the radiated power since for $a_0 = 68$ we find χ_e which is smaller than 10^{-1} for most electrons, so the error committed is acceptable for a rough estimate. We can correct the classical approach accounting for a quantum factor $g(\chi_e)$ as defined in eq. (1.43), using the Ridgers fit defined in eq.(3.77). This new quantity is called *quantum corrected classical power*, we will refer to it with the acronym cLL standing for *Corrected Landau-Lifshitz* (P_{cll}).
 In figure 7.8 we can see four snapshots of the classical corrected radiated power in the system as the pulse propagates into the plasma. The brighter the color, the higher the χ_e^2 of the particle is, highlighting the most active electrons and their position in the box. It should pointed out that the pulse follows the brighter region almost perfectly, suggesting that the radiating electrons are mostly the ones inside the pulse at each timestep. Furthermore we can see how P_{cll} increases even more in the reflection region at the reflection instant. The *afterglow* effect is shown to be remarkably smaller than *ramp* and *burst*.
It should be remarked that the channel is not left completely empty after the laser passage, and thus moderately energetic electrons are left in the static magnetic field of the channel with equivalent a_0 of th order of $\sim 10^1$. This condition leads undoubtedly to photon emission, but as shown in figure 7.8 is negligible with respect to the emission from the rest of the system. We can then assume that all the photon emission of the *ramp* comes from the electrons directly into the propagating pulse at each instant. At this point we can assume the following:

- The *ramp* is linear in time because most of the power is radiated from the electrons directly into the pulse, and thus is almost constant until the reflection.

- The left-behind electrons radiate but their contribution is negligible.

- The *burst* is a phenomenon happening only in a very small spatial region

In order to asses the importance of the reflection region we integrated over time the map of the corrected classical radiated *power* to obtain a map of the corrected classical radiated *energy*. Furthermore we can integrate over the y-coordinate to obtain a linear energy density radiated away. These two plots are found in figure 7.9.
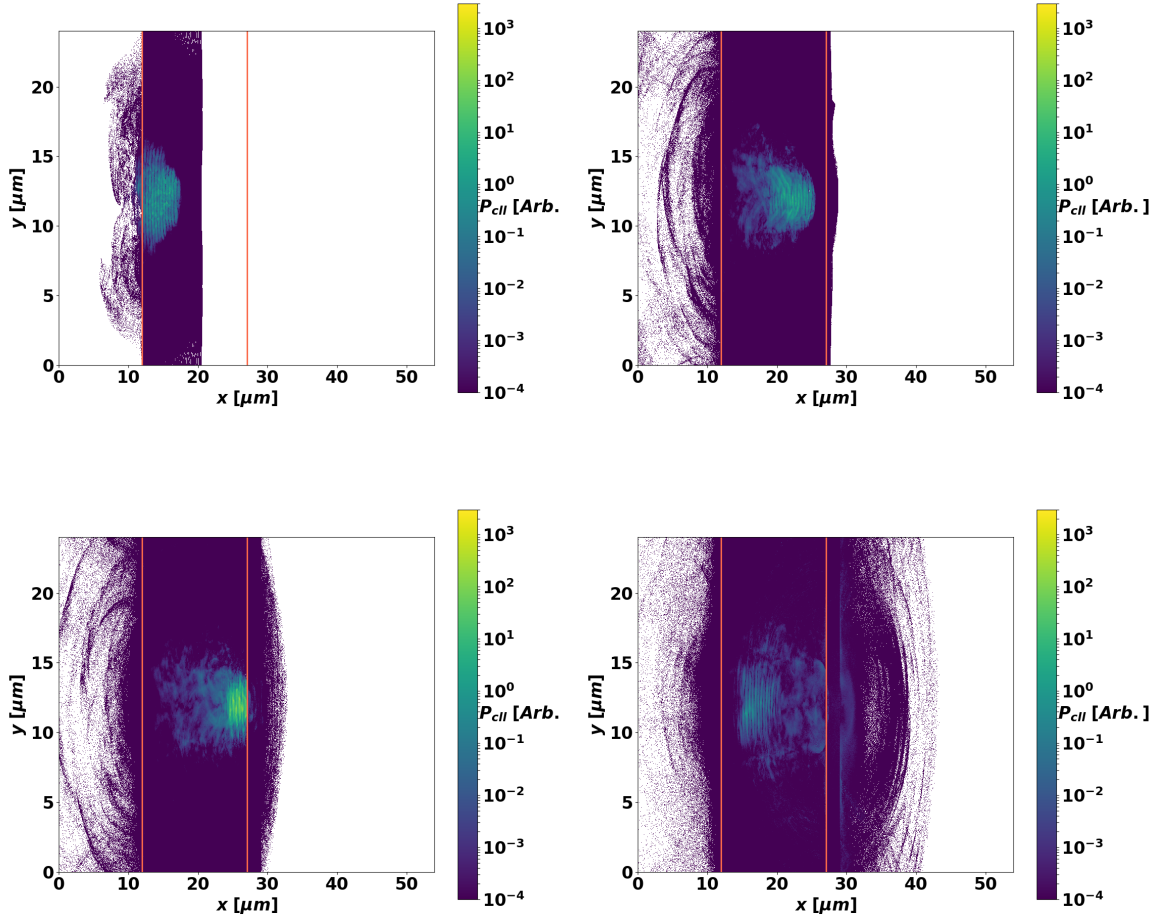
Figure 7.8: Example of evolution of the estimated classical corrected (CLL) radiated power P_{cll} in the system. What is shown in colorbar is P_{cll} in logscale, the units are arbitrary. The orange bars delimit the foam volume prior interaction. The pictures are taken at respectively 30, 63, 78, and 114 fs after the beginning of the interaction. Since the colorbar is in logscale, if an electron has $\chi_e = 0$ it is represented as white, so the colored regions contain electrons which are not perfectly still and thus have $\chi_e > 0$.

We can conclude that spatially the *burst* is confined to the reflection area and that the electrons are radiating because they are in the self-enhanced reflected pulse, and not because of other exotic effects due, for example, to the interaction between particles and solid density mirror. There is indeed a small peak of activity on the rear surface of the target caused by the pull back force of the solid toward the electrons willing to leave the target. Overall we can see that this phenomenon is negligible with respect to the other mechanisms in the system.

It is important to mention that depending on the *burst* magnitude the importance of this region can both increase or descrease with respect to the rest of the box. For most of the cases the *burst* is the main source of photons, and so is also this region of the target. There are few cases in which the burst does not happen because the field is too weak at the reflection. Those configuration are far from the optimum, so we do not bother too much discussing them, since they are interesting only as an extreme reference for the other cases.
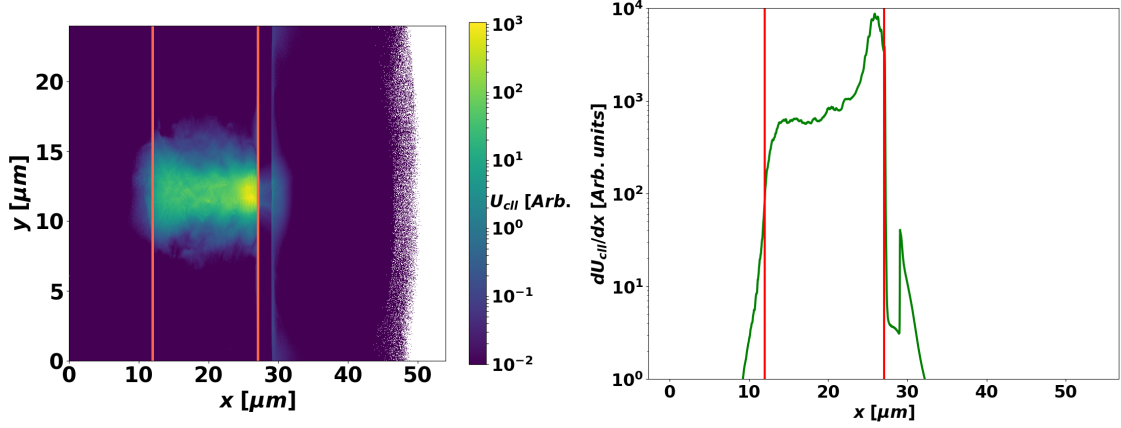
Figure 7.9: Example of estimated corrrected classical radiated energy integrated over time (left) and, same map integrated over y (right). Typically most of the energy radiated away comes from the small ($\sim \mu$m) area where the reflection happens.

7.2.2 Energy spectra and temperature

Now we look at the features of the electrons energy spectra. Fixing a specific a_0 and n_0 we typically observe something like figure 7.10 . The spectra are taken right before the reflection so that we can see the pure effect of the pulse propagation on the electronic spectrum. The energy spectra given in this work will be often given as a differential spectrum ($dn_e/d\gamma_e$), with n_e being the elctronic density, and the quantity γ_e being the electronic Lorentz factor. Recalling its definition we know that $\epsilon_{kin} = m_e c^2 (\gamma_e - 1)$ so actually for $\gamma_e \gg 1$ we have that $\epsilon_{kin} \approx m_e c^2 \gamma_e$, meaning that approximately for $\gamma_e \approx 2$ we have $\epsilon_{kin} \approx 1$MeV. In this work typical values for the maximum electron energy have the order of several hundreds of MeVs ($\gamma_e \sim 10^3$) for homogeneous foams and about 100 MeV lower for nanostructured ones.
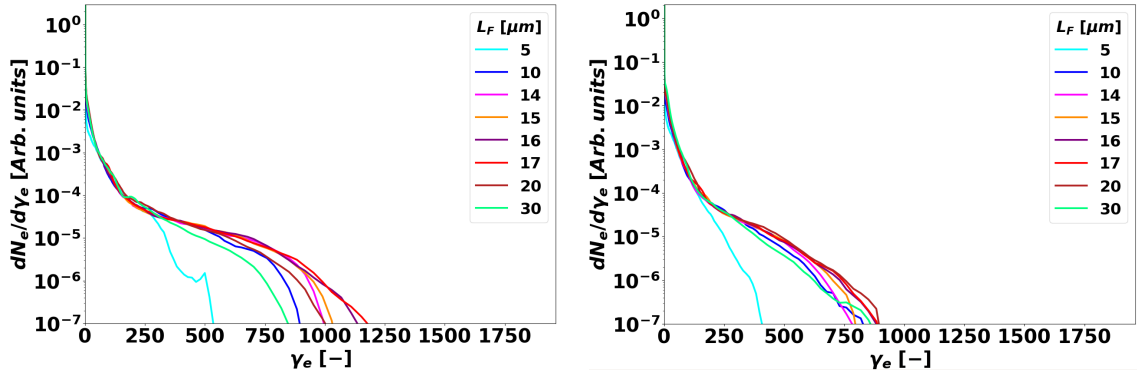
Figure 7.10: Typical spectra for a specific laser intensity and foam average density. In particular this case refers to $a_0 = 68$ and $n_0 = 3n_c$ in both HOMO (left) and NANO (right) configuration.

Often in literature the hot electron temperature is a characterizing parameter so

would be interesting to see how it relates to the other quantities. Unfortunately in this work is not always easy to define a temperature rigourosly for all the analyzed curves. Furthermore the temperature and the maximum energy of the electrons seem unrelated. When talking about radiation emission, the most active electrons are the hottest, so the ones near the maximum for which $\chi_e(\propto \gamma_e)$ can reach the highest values. This leaves us uncertain on how the temperature should relate to the results. We tried three possible fits: Maxwell-Juttner, Maxwell-Boltzman, and simple decaying exponential. Everyone of those did not seem to quite work for every case, and comparing values obtained from different models can be complicated. For these reasons we will not discuss thoroughly the hot electron temperature. We will only say we observed qualitatively that in general higher temperature means higher overall conversion efficiency.

7.2.3 *Ramp* properties

In order to better characterize the *ramp* we need to look at only one more quantity: χ_e.

In figure 7.11 is shown the time-averaged χ_e spectra for $n_0 = 6n_c$, $a_0 = 68$, for both homogeneous and nanostructured foams. We can see that the right part of the spectra, representing also the most active electrons in the system, are very similar and can be barely told apart. This observation agrees with the fact that we see a *ramp* of almost constant slope. The power emitted is infact only a function of χ_e and of the number of electrons with high enough χ_e, so if the differential spectrum $(dn_e/d\chi_e)$ is very similar, also the radiated energy curves will be almost indistinguishable.
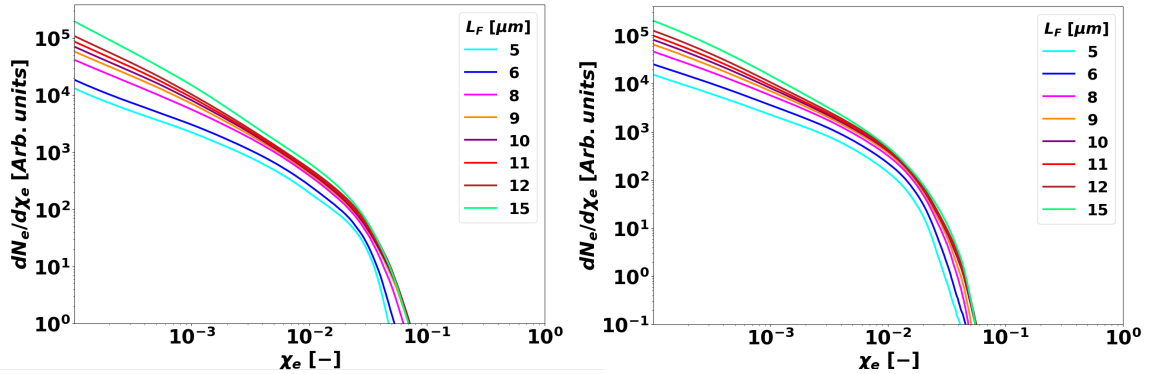
Figure 7.11: Example of χ_e spectrum for $n_0 = 6n_c$, $a_0 = 68$, averaged in the duration of the *ramp*, in HOMO (left) and NANO (right). The spectra are very similar to each other, as expected since the ramp properties should not vary much for the same n_0.

The number of activated electrons should be roughly proportional to the volume covered by the laser inside the foam. From diagnostics like the one in figure 6.4 we computed the propagation speed of the pulse inside the foam, and observed that for a specific density and laser intensity it is roughly constant. Then it is reasonable to assume that the number of active electrons increases almost linearly with time as shown in figure 7.12 .

One can notice that something might not add up in what just said. How come that if the number of activated electrons increases then the power does not? The

explanation comes from the fact that we are just increasing the number of electrons in the left side of the spectrum, which are active but not much, so most of the power come from an almost constant number of electrons.
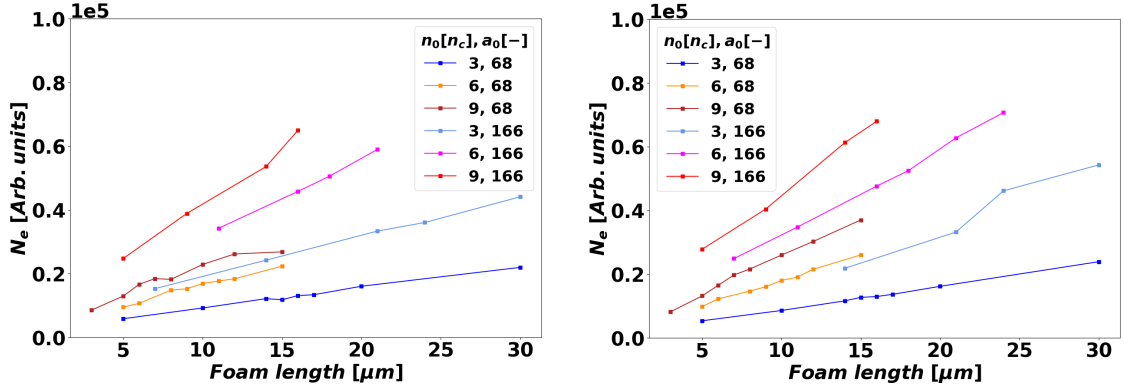
Figure 7.12: Number of electrons with $\chi_e > 0$ (only electrons which interact with pulse) for homogeneous (left) and nanostructured (right) configurations. It is shown an almost linear relation as expected from simple geometrical statements.

7.2.4 *Burst* properties

We begin the discussion presenting figure 7.13, which represents the same case as figure 7.11 but during the burst. In order to focus ourselves on the process of the *burst* we look at what we will call "restricted spectrum" meaning that we are interested only in the particles in the small volume of space of $\sim 1\mu$m $\times 1\mu$m at the boundary between mirror and foam. We prefer to use only these electrons because the burst is a pretty localized phenomenon (as seen in fig. 7.8) and its properties should be only characterized by the properties of the particles in the same volume. Looking at the complete spectrum of all the particles in the box we would find the same value for χ_e^{max} but, on the left part of the spectrum we would have lots of electrons coming from all the box which are not contributing to the burst.
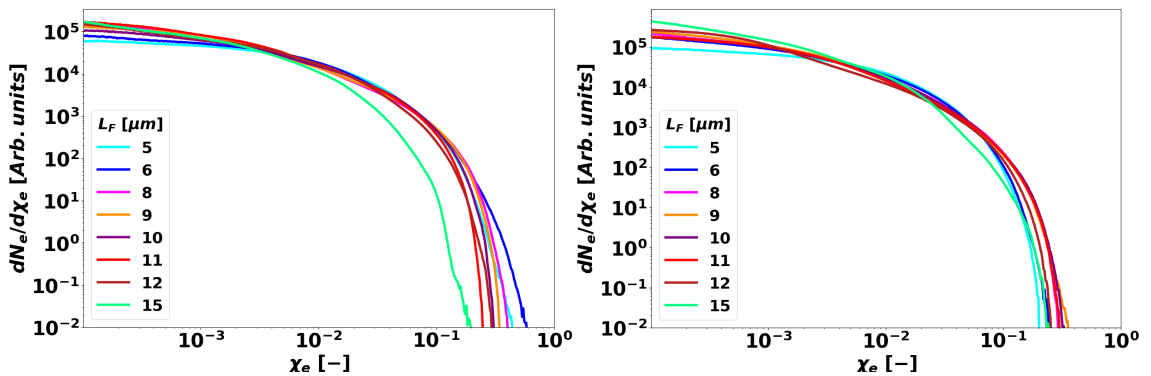
Figure 7.13: Example of χ_e restricted spectrum for $n_0 = 6n_c$, $a_0 = 68$, averaged in the duration of the *burst*, in HOMO (left) and NANO (right). Now the spectra reach sensibly higher values, letting us expect more sever radiation emission.

We should notice that during the *burst* the right part of the spectrum now changes more for different L_F with respect to the spectra in the *ramp*. Furthermore the shape of the spectra in this case is also different having more electrons with higher χ_e values. This is definitely an effect of the enhanced field amplitude experienced by the particles during the reflection.

7.3   Radiation properties

In the previous sections we saw that electrons have different properties if looked at during *ramp* or at the *burst*. This leads us to expect also differences in the spectrum of the emitted radiation. We will characterize the energy spectrum of the photons but also their angle of emission which is important to reach high brilliance.

7.3.1   *Ramp* characterization

The first important quantity we want to look at is the energy spectrum of the photons. In figure 7.14 we can observe both the differential $(dU_\gamma/d\gamma_\gamma)$ and cumulative spectrum (U of all photons with $\gamma \leq \gamma_\gamma$) of the totality of the photons emitted during the *ramp*. Roughly two thirds of the energy goes into photons of less than 1 MeV while only few percent is stored into multi-MeV photons. Nanostructured targets having lower average χ_e emit photons at lower energies as expected from the theory.

In order to have a single parameter to compare different densities and configurations we will look at the energy of the photons when the cumulative curve reaches 90% (second black dashed line) of the converted energy. We call this value γ_{90} and it gives us a good idea of the overall distribution of energy among the photons. In figure 7.15 the quantity γ_{90} is plotted in function of L_F for different values of n_0 and a_0.

It cannot go unnoticed the remarkable difference in values of γ_{90} for the cases at average densities $n_0 = 3n_c$ with respect to the others at $a_0 = 68$. We are not sure about the physical reason behind this behaviour, but since there is no visible differences between the cases with $n_0 = 6n_c$ and $n_0 = 9n_c$, we suggest that a possible threshold mechanism could rise at specific densities or for specific opacity factor $\overline{n}$. The curves for $a_0 = 166$ are fairly more similar in behaviour, suggesting that maybe the threshold hypothesized is around $\overline{n} \sim 0.1n_c$ (refer to table 4.2). Further investigation of more densities and laser intensities is needed in order to reinforce the idea of a threshold mechanism acting for $\overline{n} < 0.1n_c$ which increases the vaule of γ_{90}. Theoretical justification of such phenomenon may be found in different dominant processes at different trasparency regimes (i.e. DLA, LWFA, ...).

As we already did previously in section 7.1.3, we look at the results in function of the parameter $\overline{\mu} = \overline{n}L_F$ and we see how all the curves obtained with $a_0 = 166$ tend to collapse together making sort of a single curve (fig. 7.16) suggesting a common behaviour for $a_0 = 166$.
It is due to remember that the parameter γ_{90} is an arbitrary quantity of our choice to somehow quantitatively compare photon spectra of the type of figure 7.14. The first step in order to do a better analysis would be to find a more characterizing parameter to describe the spectra. In the frame of this work γ_{90} works adequately, so we will no further study other ways of comparing photon energy spectra, and we
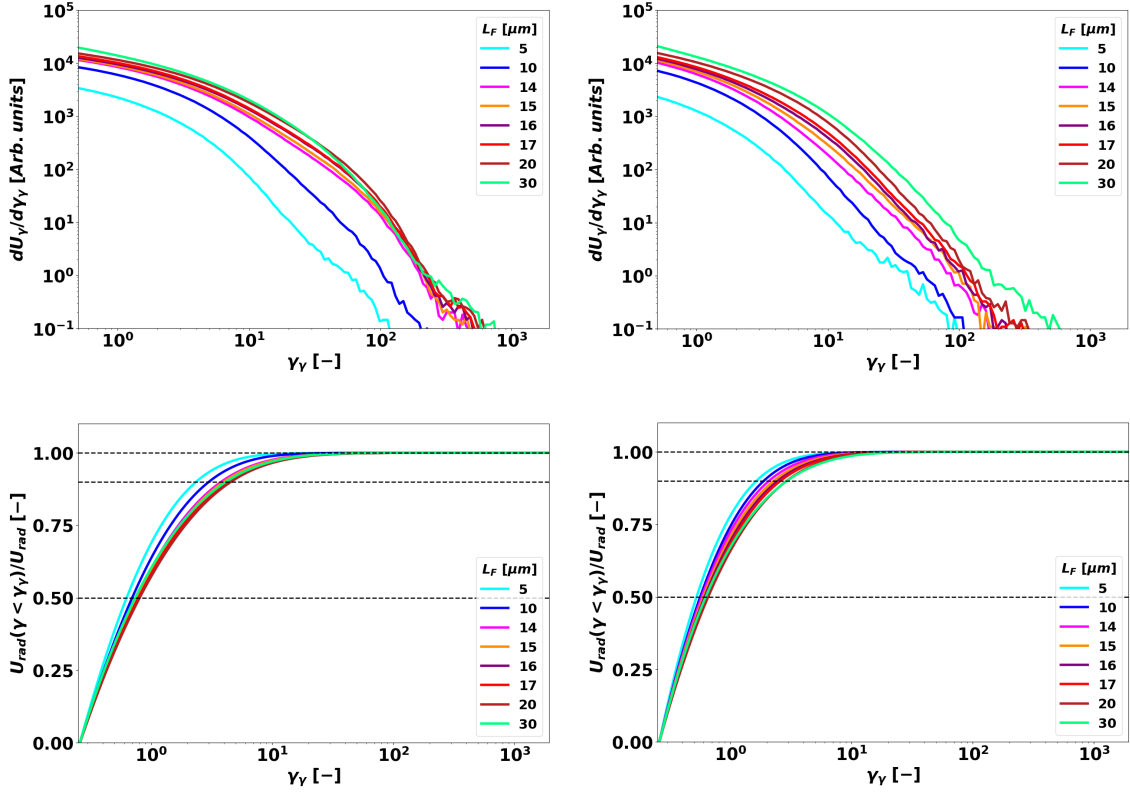
Figure 7.14: Example of differential (top row) and cumulative (bottom) energy spectra for $n_0 = 3n_c$ and $a_0 = 68$ for both homogeneous (left) and nanostructured (right) foams during the *ramp*. The spectrum is taken at the end of the *ramp* and is comprehensive of all photons produced before the *burst*. We notice that more than half of the energy produced is below $\gamma_\gamma = 1$ corresponding to an energy equal to the electron rest mass. While the last 10% of the energy comes from photons of $0.7 \div 2.5$ MeV ($1.5 \leq \gamma_\gamma \leq 5.$). The three black dashed lines represent (from top to bottom) 100%, 90%, and 50% of the total emitted power and are plotted to help the reading of the plot.
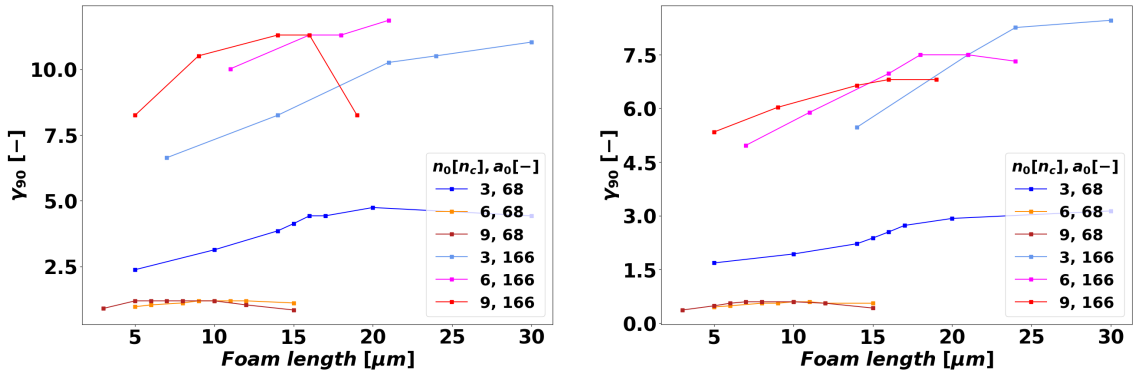
Figure 7.15: Values of γ_{90} of the photons emitted during the *ramp* for a homogeneous (left) and nanostructured (right) target. The difference at $a_0 = 68$ between $n_0 = 3n_c$ and the other densities is remarkable.

will refer to future studies in the matter.

Consideration on the energy spectrum of the produced photons are important, but so is duscussing the angular distribution of said particles. In order to have an effective
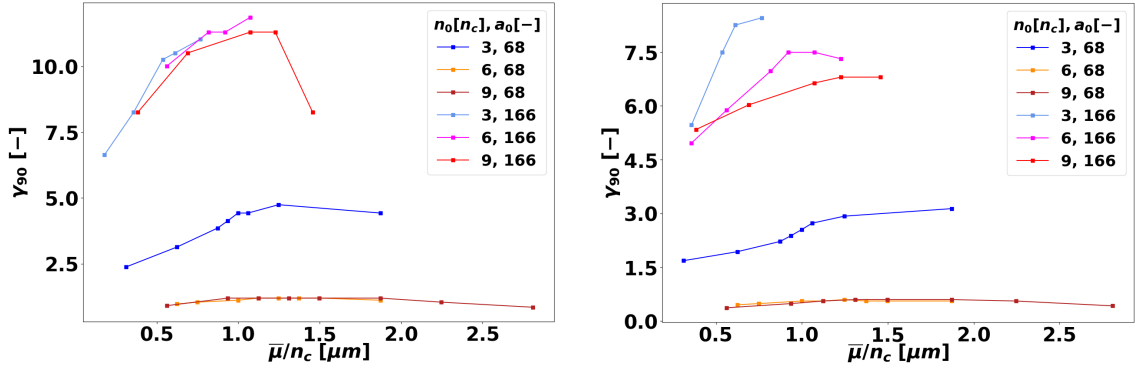
Figure 7.16: Values of γ_{90} of the photons emitted during the *ramp* vs normalized number thickness ($\overline{\mu}/n_c$) for a homogeneous (left) and nanostructured (right) target. The curves at $a_0 = 166$ come together while for $a_0 = 68$ the differences are conserved from figure 7.15.

γ-ray source we should be able to confine the photons into the smallest solid angle possible. As suggested in figure 7.17 longer foams generally correspond to also higher photon maximum energies in the *ramp* regime. Discussing quantitatively a parameter in colors is never easy, so everytime a plot in color is shown we focus mainly on the shape of the colors rather than their precise values. The angle of emission is reported on the y axis and is defined with $\theta = 0$ as parallel to the laser progation ($x > 0$), so that at the center of the image are pictured the photons emitted "forward" while at the top and at the bottom are plotted the ones emitted "backward".
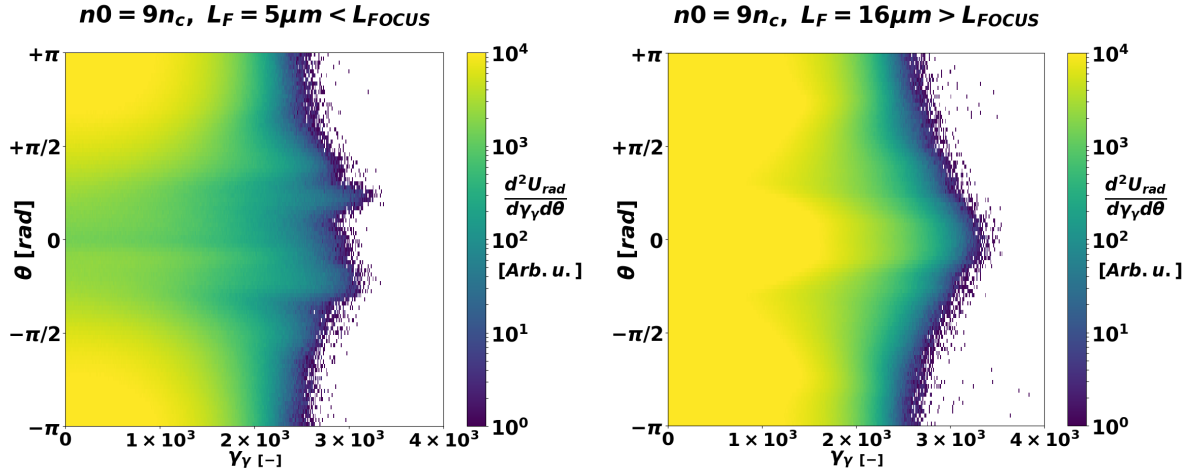
Figure 7.17: Photons angular spectrum at the end of the *ramp* for two specific cases: $L_F = 5\mu$m and 16μm, both are for $n_0 = 9n_c$ and $a_0 = 166$ in homogeneous foam. Radially is plotted the photon energy γ_γ while in colors we find the logarythm in base ten of the relative photon energy distribution. The angle is define so that $\theta = 0$ is parallel to $x > 0$ and the laser propagation. For this configuration $L_{FOCUS} = 14\mu$m.

We should notice a pretty unexpected effect: for short foams we find an angular dispersion of the photons mainly in two symmetric "lobes" (left in fig.7.17), while for longer foams we find also a more "plume"-like shape around the direction $\theta = 0$ (right in fig.7.17). We know that the behaviour in the *ramp* is the same for each configuration up until reflection so this means that the *plume* we see for thicker foams

is produced after the *lobes*. The plot on the right in figure 7.17 is then obtained by a the sum of the *lobes* produced in the early stages of the *ramp* and the *plume* produced on the second part.

Recalling that for incoherent emission we always assume that the photon is emitted in the direction of motion of the electron, we can then observe that the shape we see is also representative of the angle distribution of the electrons motion. Looking at the phase space (p_x, p_y) of the electrons we indeed find the same shape. This peculiar phenomenon seems to be related to the focal length of the pulse in the foam. Reporting all the pictures for all cases (too much pages would be required to do so) we would see the exact same lobes-plume transition passing at roughly the L_{FOCUS} of the system. Its origin is not completely clear, but the effect is to lower the photon dispersion resulting in potentially higher brilliance for longer foams.

7.3.2 *Burst* characterization

First of all we should point out how the spectrum shape changes from *ramp* (fig.7.14) to *burst* (fig.7.18). The first is steeper meaning more energy is emitted in the low-end of the spectrum, while the latter has relatively more energy stored in high frequency photons. The maximum value of γ_γ is roughly the same for both *ramp* and *burst*, what really changes is, as just said, the realtive number distribution of the photons. Further evidence of what just stated is found in the cumulative energy distribution which clearly shows more energy has been converted into high energy photons. Quantitatively now about half of the energy is stored into multi-MeV photons and the parameter γ_{90} is shown in figure 7.19.

As found in the *ramp* we notice a strong difference at $a_0 = 68$ between the cases with average density $n_0 = 3n_c$ and the other cases which are pretty much indistinguishable from the point of view of this parameter. This difference is reflected both in the homogeneous and nanostructured targets leading us to believe there could be some kind of threshold-like mechanism activating for a low/high enough density just like we said in the previous section.

It should be pointed out how for $a_0 = 166$ we reached $\gamma_{90} \sim 50$ which corresponds to $\sim 25\text{MeV}$, much higher than the few MeVs of the $a_0 = 68$ configuration.

As we have already seen in this work, looking at the results from the point of view of the parameter $\overline{\mu}$ could be useful. Looking at figure 7.20 we can see the tendency of the curves at $a_0 = 166$ to collapse on each other, but in a less effective way than we have seen for the *ramp*. The *burst* confirms to be the most complex phenomenon in our system, and proposing a scaling for its magnitude or properties is no simple task.

We want to point out how the same lobes-plume transition is translated into the *burst* spectrum. For short enough foams ($L_F < L_{FOCUS}$) the electron phase-space (p_x, p_y) is shaped more like two lobes while for longer foams it slowly transitions to a more plume-like shape which, since the photon is always emitted in the direction of motion, means a specular shape in photon angular spectrum. Longer foams means more photons along the $x-$axis which is better for high brilliance sources. All the consideration made about this behaviour during the *ramp* are perfectly valid also here. In case of the *burst* the effect is enhanced since plotted are only the photons produced during the reflection and thus the photons are representative of only the electronic phase-space during the *burst*. So if the electrons are more *plume*-like we see only the *plume*-like photons and not the sum of different phase-space shapes. The angular spectrum of the photons in the *burst* are the same as the one produced
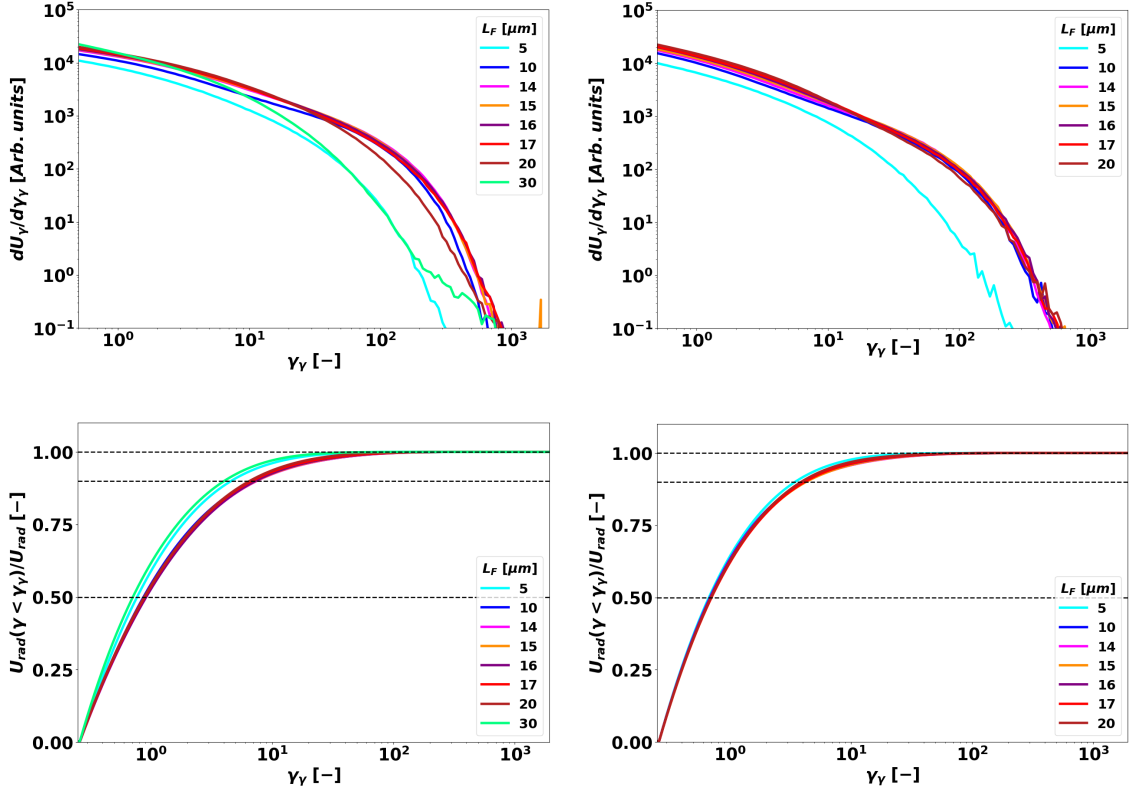
Figure 7.18: Example of differential (top row) and cumulative (bottom) energy spectra for $n_0 = 3n_c$ and $a_0 = 68$ for both homogeneous (left) and nanostructured (right) foams during the *burst*. The spectrum is comprehensive of all photons produced during the *burst*. We notice that now more than half of the energy produced is above $\gamma_\gamma = 1$ corresponding to an energy equal to the electron rest mass. While the last 10% of the energy comes from photons of ~ 5 MeV ($\gamma_\gamma \sim 10^1$).
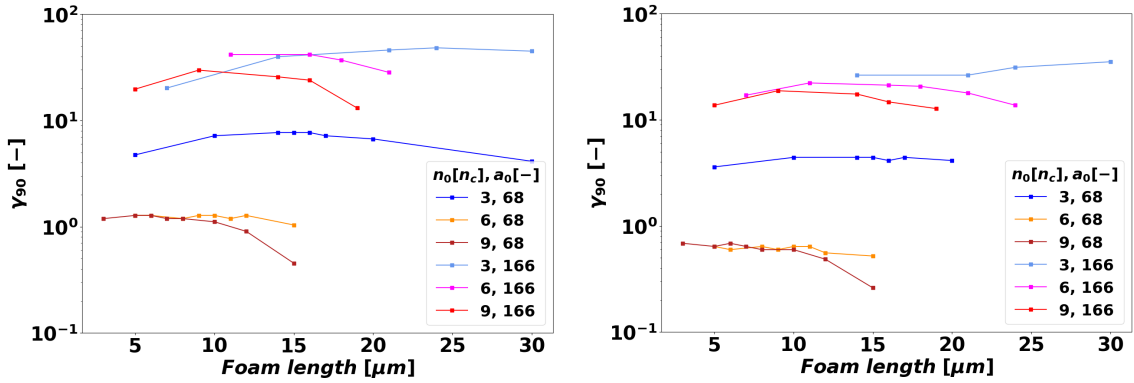
Figure 7.19: Values of γ_{90} of the photons emitted during the *burst* for a homogeneous (left) and nanostructured (right) target. The difference between $n_0 = 3n_c$ and the other densities is remarkable. It should be noticed that the scale of the y axis is now logarithmic.

in the last moment of the *ramp*.
Overall nanostructured cases follow the same trends as homogeneous ones but less efficiently, thus localized higher density seems to be detrimental to the process.
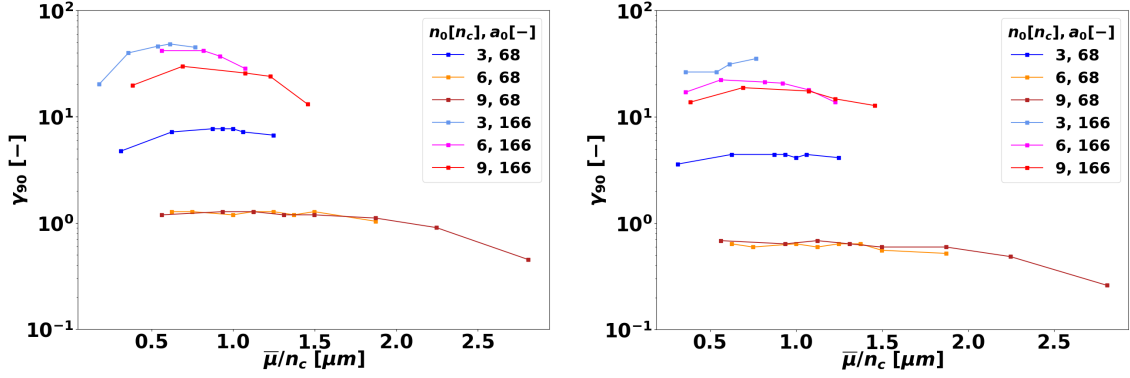
Figure 7.20: Values of γ_{90} of the photons emitted during the *burst* vs normalized number thickness ($\overline{\mu}/n_c$) for a homogeneous (left) and nanostructured (right) target. The difference between $n_0 = 3n_c$ and the other densities is remarkable. It should be noticed that the scale of the y axis is now logarithmic.
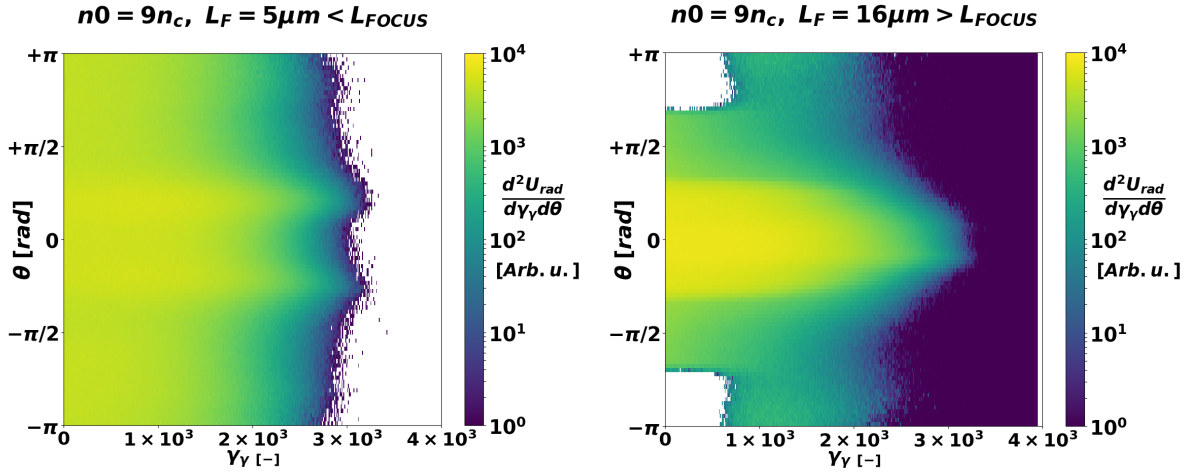
Figure 7.21: Photons angular spectrum during the *burst* for two specific cases: $L_F = 5\mu$m and 16μm, both are for $n_0 = 9n_c$ and $a_0 = 166$ in homogeneous foam. Radially is plotted the photon energy γ_γ while in colors we find the logarythm in base ten of the relative photon energy distribution. The angle is define so that $\theta = 0$ is parallel to $x > 0$ and the laser propagation. For this configuration $L_{FOCUS} = \mu$m.

Chapter 8

Conclusions and future perspective

In the present thesis, an extensive parametric study has been carried out with the kinetic, relativistic and quantum *Particle-In-Cell* (PIC) code *Smilei* in order to explore the possibility to use the MultiPetawatt facility *Apollon* with near-critical nanostructured targets for the purpose of high-energy photon generation.

First, an overview on the phenomenon of the *synchrotron-like* radiation emission has been given from a very general point of view (chapter 1). An appealing way to generate such kind of radiation relies on high-energy electrons heated in laser-plasma scenarios, especially if the interaction occurs in the near-critical regime. For this reason, coupling the Apollon laser with nanostructured MLTs is very interesting, bringing together the potential of a state-of-the-art laser facility and an advanced targetry concept (chapter 2). A photon source that is based on this kind of configuration has the interesting advantage of being relatively compact, flexible, and affect by limited radioprotection concerns. Understanding in details the physical features of this configuration is of great interest, but because of its complexity, a complete understanding of its behaviour can only be obtained through numerical simulations. PIC simulations are the most suitable tool for this purpose, being able to take into account the kinetic, relativistic, and quantum effects that are relevant in the considered scenario. Hence we explained the main structure and features of PIC codes, in order to help us understand the criticalities of this kind of numerical simulation (chapter 3).

We used the previous works in the literature on nanostructured foams to help us correctly model the targets, and the actual specifics of the *Apollon* facility to accurately describe the laser parameters.(chapter 4)

We started our work by understanding what physical processes were important in our system, in particular we examined the effect of *tunnel-ionization* and *binary collisions*. It was observed that for the regimes of interest here, *binary collisions* are completely negligible while *tunnel-ionization* has a small ($\sim 1\%$) effect on the results. Modelling *tunnel-ionization* could perhaps improve our description of the system, but the computational costs of its use can be far greater than the actual benefits, so we decided to simulate collisionless fully ionized targets.(chapter 5)

In order to enhance photon emission, huge electromagnetic fields are required, thus the need to find ways to increase the maximum field amplitude arises. At this regard, a crucial point was to better understand the characteristics of the propagation of a *Ultra-High-Intesity* (UHI) laser pulse into a near-critical double-layer targets. Using the combined effect of a proper foam thickness (L_F) and a solid density foil ("mirror")

we observed an increase in the field amplitude (B_Z^{MAX}/a_0) ranging from about 2.5 up to more than 4, which translates roughly in one order of magnitude gain in laser intensity ($I^{MAX}/I_0 \sim 10^1$). (chapter 6)

Finally in chapter 7 we discussed the radiation emission features.

We looked first at the macroscopic quantities such as the total kinetic energy of electrons, and the total energy of the emitted photons. Three distinct "phases" in the course of the interaction were observed, which were called: *ramp*, *burst*, and *afterglow*. We characterized each one of them from a macroscopic, and microscopic point of view. The *ramp* is characterized by a roughly constant radiated power in time, and corresponds to the laser pulse propagating through the near-critical layer of the target. The *burst* happens when the pulse is reflected by with the solid density foil, enhancing the fields amplitude which in return increases the radiated power. The *burst* is also very short in time, its duration has been found to be of the order of half of the Full-Width-Half-Maximum in time of the pulse prior interaction ($\Delta t_{BURST} \sim \tau_p/2 = 10$fs). After the reflection the pulse propagates back through the near-critical layer until it leaves the target, this phase is called *afterglow* and is characterized by a very small radiated power.

It was shown that finding the right balance between *ramp* and *burst* was of the utmost importance in order to increase the fraction of energy converted from laser to photons, while the *afterglow* has a nearly negligible effect on the overall dynamics of the system. For a laser pulse characterized by $a_0 = 68$ ($I_0 \approx 10^{22}$Wcm^{-2}) we obtained that over 7% of the energy from the laser was converted to photons, in the best configuration, and a maximum photon energy of hundreds of MeVs. For higher intensities, namely $a_0 = 166$ ($I_0 \approx 5.9 \times 10^{22}$Wcm^{-2}), the maximum conversion reached was over 22% of the total pulse energy, for a maximum photon energy of the order of the GeV. Those are stunning results considering that these very laser parameters will be achievable experimentally in the next years at the *Apollon* facility. Nevertheless we should again remark that 2D simulations overestimate the results, so eventhough we expect a real experiments to perfom worse than what has been shown here, simulating some configurations in 3D geometry could help us being more precise in estimating a real photon yield and energy.

Looking at the photon spectrum instead, it was shown how the photons emitted during the *burst* were far more energetic than the ones emitted during the *ramp*. Defining a "best" configuration is therefore not obvious: if the goal of a specific experiment is to convert as much energy possible to photons regardless of their energy spectrum, then the "best" configuration is one which can maximize the fraction of energy converted in photons, relying on a good balance between *ramp* and *burst*. On the other hand, if the goal is to obtain high energy photons, then a configuration characterized by a huge *burst* is to consider the "best", regardless of the overall conversion efficiency.

Parameter of great importance which has been shown to be promising in the interpretation of the results is the *normalized number thickness* $\overline{\mu}/n_c = \overline{n}L_F/n_c$. This quantity has hardly ever being used in the literature around the topic of this work, but it helped us characterize the systems, and we expect it to be an important parameter in future studies as well.

The homogeneous targets performed better than their nanostructured counterpart, in both macroscopic energy conversion, and photon maximum energy, even for the same value of average density (n_0). This effect has to be attributed to the dishomogeneity of the latter ones, which leads to a local high ($\sim$solid) density of the nanoparticles.

In conclusion, we investigated by means of 2D PIC simulations a laser-driven photon

source based on the Apollon multi-PW laser system and near-critical double-layer targets. The PIC code Smilei is an effective tool to investigate this physical system. We examined the emission process in detail, considering the role of the different stages of the interaction in the emission itself. The parameters we investigated were vast, and spaced from an average density of the near-critical layer of 3 to 9 times the critical density of the corresponding plasma, with thickness ranging from 3 to 36 μm, and laser intensities of 1×10^{22}Wcm^{-2} ($a_0 = 68$) to 5.9×10^{22}Wcm^{-2} ($a_0 = 166$). For the first time such an extensive parametric study included a systematic discussion of the produced photon energy and angular spectrum.

We found that to optimize the photon production one has to cleverly tailor both the target and laser parameters in order to be able to control the ramp and burst stages. Overall, we find that high-energy photon sources constitute a promising application of ultra-high-intensity (UHI) lasers. The overall numerical campaign, from the preliminary investigations to the final outcome, consisted in hundreds of simulations, for a total computational time of over 1.5 MCPUhours.

This work could set the basis for future developments, here we propose few topics for future studies which would answer some of the questions arised from this work:

- *Modelling of an UHI laser pulse propagation in nanostructured foams.* In particular we would like to better understand the behaviour of a nanostructured NCD plasma irradiated with such intense and short pulses. The information important in the frame of this present work would be: an analytical relation or scaling which is able to predict the position and the magnitude of the maximum amplification of the laser due to the self-focusing effect, how the pulse is shaped and compressed during the propagation, a scaling able to describe the difference brought by a local high electronic density with respect to an homogeneous configuration, and, a relation expressing the dependence of the behaviour of a nanostructured foam on the size of the nanoparticles.

- *Effect of pre-pulses and/or pedestals in the laser temporal profile.* There is no pulsed laser that can be produced with a perfect temporal profile, a pre-pulse or pedestal is always present which leads to the anticipated delivery of laser energy to the target. For UHI pulses even a relatively high contrast (ratio between the pulse peak intensity and the intensity that preceeds it) ($\sim 10^8 \div 10^{10}$) could lead to the modification of the target structure, and therefore also of its properties. Usual time scales of such pedestals are of the order of $10^0 \div 10^1$ps so extensive parametric studies on this topic would be extremely expensive computationally. An organic study on the topic would be a key to bring the simulation world closer to the real experimental conditions.

- *Quantitative characterization of the photon spectra.* In the frame of this study we gave a quantitative description of the photon spectra based on the value of γ_{90} (see section 7.3) which is a simple and arbitrary quantity. A deeper characterization of the energy distributions (energy spectra) and of their higher order momenta could give us more (non-arbitrary) parameters for comparison.

- *Explore more regimes.* Expanding our knowledge on more regimes, studying combinations of nanostructured targets and lasers with different parameters such as intensity, total pulse energy, different polarization, and, longer pulses ($\sim 10^2$fs).

- *3D simulation campaign.* Because of its computational cost, 3D PIC simulations are not suitable for parametric studies, but understanding how the dimensionality of the system changes the results is of the utmost importance in order to try to predict experimental results. Nanostructures are intrinsecally 3D and real targets are nanostructured, not homogeneous. It goes without saying that simulating a more realistic 3D foam-based target would be crucial to accurately predict experimental outcomes.

This work has shown how the combination of advanced nanostructured targetry and the forthcoming Multi-Petawatt facilities could be employed as an effective, and efficient high-energy photon source. One thesis alone could not possibly contain all the knowledge necessary to develop a laser-driven compact γ-source but can be regarded as a starting point for future works on this topic.

List of Figures

List of Tables

Bibliography

[1] RS Holt, MJ Cooper, and DF Jackson. Gamma-ray scattering techniques for non-destructive testing and imaging. *Nuclear Instruments and Methods in Physics Research*, 221(1):98–104, 1984.

[2] ERC project ENSURE Website. `https://www.ensure.polimi.it/`. Accessed: 2019-11-6.

[3] Julien Derouillat, Arnaud Beck, F Pérez, T Vinci, M Chiaramello, A Grassi, M Flé, G Bouchard, I Plotnikov, N Aunai, et al. Smilei: A collaborative, open-source, multi-purpose particle-in-cell code for plasma simulation. *Computer Physics Communications*, 222:351–373, 2018.

[4] Bertrand Martinez. *Radiative and quantum electrodynamic effects in ultra-relativistic laser-matter interaction.* PhD thesis, Université de Bordeaux, Bordeaux, France, 2018.

[5] AI Nikishov and VI Ritus. Quantum processes in the field ofa plane electromagnetic wave and in a constant field. *SOVIET PHYSICS JETP*, 19(5), 1964.

[6] John David Jackson. *Classical electrodynamics.* John Wiley & Sons, 2007.

[7] Fabien Niel. *Classical and quantum description of plasma and radiation in strong fields.* PhD thesis, Sorbonne Université, Paris, France, 2018.

[8] Edward M Purcell and David J Morin. *Electricity and magnetism.* Cambridge University Press, 2013.

[9] Herbert Spohn. The critical manifold of the lorentz-dirac equation. *EPL (Europhysics Letters)*, 50(3):287, 2000.

[10] F Niel, C Riconda, François Amiranoff, R Duclous, and M Grech. From quantum to classical modeling of radiation reaction: A focus on stochasticity effects. *Physical Review E*, 97(4):043209, 2018.

[11] Roland Duclous, John G Kirk, and Anthony R Bell. Monte carlo calculations of pair production in high-intensity laser–plasma interactions. *Plasma Physics and Controlled Fusion*, 53(1):015009, 2010.

[12] TD Arber, Keith Bennett, CS Brady, A Lawrence-Douglas, MG Ramsay, NJ Sircombe, P Gillies, RG Evans, Holger Schmitz, AR Bell, et al. Contemporary particle-in-cell approach to laser-plasma modelling. *Plasma Physics and Controlled Fusion*, 57(11):113001, 2015.

[13] Mathieu Lobet, Emmanuel d'Humières, Mickael Grech, Charles Ruyer, Xavier Davoine, and Laurent Gremillet. Modeling of radiative and quantum electrodynamics effects in pic simulations of ultra-relativistic laser-plasma interaction. In *Journal of Physics: Conference Series*, volume 688, page 012058. IOP Publishing, 2016.

[14] A Gonoskov, S Bastrakov, E Efimenko, A Ilderton, M Marklund, I Meyerov, A Muraviev, A Sergeev, I Surmin, and Erik Wallin. Extended particle-in-cell schemes for physics in ultrastrong laser fields: Review and developments. *Physical review E*, 92(2):023305, 2015.

[15] Europe enters the extreme X-ray era. `https://cerncourier.com/a/europe-enters-the-extreme-x-ray-era/`. Accessed: 2020-03-21.

[16] Paul Gibbon and Eckhart Förster. Short-pulse laser-plasma interactions. *Plasma physics and controlled fusion*, 38(6):769, 1996.

[17] Andrea Macchi. *A superintense laser-plasma interaction theory primer*. Springer Science & Business Media, 2013.

[18] Donna Strickland and Gerard Mourou. Compression of amplified chirped optical pulses. *Optics communications*, 56(3):219–221, 1985.

[19] Gerard A. Mourou, Toshiki Tajima, and Sergei V. Bulanov. Optics in the relativistic regime. *Rev. Mod. Phys.*, 78:309–371, Apr 2006.

[20] Arianna Formenti. Intense laser interaction with nanostructured plasmas: a kinetic numerical investigation. 2016.

[21] D Bauer, P Mulser, and W-H Steeb. Relativistic ponderomotive force, uphill acceleration, and transition to chaos. *Physical review letters*, 75(25):4622, 1995.

[22] Andrea Macchi, Marco Borghesi, and Matteo Passoni. Ion acceleration by superintense laser-plasma interaction. *Reviews of Modern Physics*, 85(2):751, 2013.

[23] L Fedeli, A Formenti, L Cialfi, A Sgattoni, G Cantono, and M Passoni. Structured targets for advanced laser-driven sources. *Plasma Physics and Controlled Fusion*, 60(1):014013, 2017.

[24] Alexander Pukhov. Strong field interaction of laser radiation. *Reports on progress in Physics*, 66(1):47, 2002.

[25] Thomas C. Katsouleas. Accelerator physics: Electrons hang ten on laser wake. *Nature*, 431:515–516, 2004.

[26] Lorenzo Cialfi, Luca Fedeli, and Matteo Passoni. Electron heating in subpicosecond laser interaction with overdense and near-critical plasmas. *Physical Review E*, 94(5):053201, 2016.

[27] Matteo Passoni, C Perego, Andrea Sgattoni, and D Batani. Advances in target normal sheath acceleration theory. *Physics of Plasmas*, 20(6):060701, 2013.

[28] Keiji Nagai, Christopher SA Musgrave, and Wigen Nazarov. A review of low density porous materials used in laser plasma experiments. *Physics of Plasmas*, 25(3):030501, 2018.

[29] Luca Fedeli, Arianna Formenti, Carlo Enrico Bottani, and Matteo Passoni. Parametric investigation of laser interaction with uniform and nanostructured near-critical plasmas. *The European Physical Journal D*, 71(8):202, 2017.

[30] Luca Fedeli, Arianna Formenti, Lorenzo Cialfi, Andrea Pazzaglia, and Matteo Passoni. Ultra-intense laser interaction with nanostructured near-critical plasmas. *Scientific reports*, 8(1):3834, 2018.

[31] A Maffini, A Pazzaglia, D Dellasega, V Russo, and M Passoni. Growth dynamics of pulsed laser deposited nanofoams. *Physical Review Materials*, 3(8):083404, 2019.

[32] Alessandro Zani, David Dellasega, Valeria Russo, and Matteo Passoni. Ultra-low density carbon foams produced by pulsed laser deposition. *Carbon*, 56:358–365, 2013.

[33] Irene Prencipe, A Sgattoni, David Dellasega, Luca Fedeli, Lorenzo Cialfi, Il Woo Choi, I Jong Kim, Karol Adam Janulewicz, KF Kakolee, Hwang Woon Lee, et al. Development of foam-based layered targets for laser-driven ion beam production. *Plasma Physics and Controlled Fusion*, 58(3):034019, 2016.

[34] Robert F Cozzens and Robert B Fox. Infrared laser ablation of polymers. *Polymer Engineering & Science*, 18(11):900–904, 1978.

[35] Alden Curtis, Chase Calvi, James Tinsley, Reed Hollinger, Vural Kaymak, Alexander Pukhov, Shoujun Wang, Alex Rockwood, Yong Wang, Vyacheslav N Shlyaptsev, et al. Micro-scale fusion in dense relativistic nanowire array plasmas. *Nature communications*, 9(1):1–7, 2018.

[36] Thomas Grismayer. *Etude théorique et numérique de l'expansion d'un plasma créé par laser: accélération d'ions à haute énergie.* PhD thesis, 2006.

[37] VT Tikhonchuk. Physics of laser-assisted ion acceleration. *Nuclear Instruments and Methods in Physics Research Section A: Accelerators, Spectrometers, Detectors and Associated Equipment*, 620(1):1–13, 2010.

[38] Hiroyuki Daido, Mamiko Nishiuchi, and Alexander S Pirozhkov. Review of laser-driven ion sources and their applications. *Reports on progress in physics*, 75(5):056401, 2012.

[39] T Schlegel, N Naumova, VT Tikhonchuk, C Labaune, IV Sokolov, and G Mourou. Relativistic laser piston model: Ponderomotive ion acceleration in dense plasmas using ultraintense laser pulses. *Physics of Plasmas*, 16(8):083103, 2009.

[40] S Steinke, P Hilz, M Schnürer, G Priebe, J Bränzel, F Abicht, Daniel Kiefer, C Kreuzer, T Ostermayr, Jörg Schreiber, et al. Stable laser-ion acceleration in the light sail regime. *Physical Review Special Topics-Accelerators and Beams*, 16(1):011303, 2013.

[41] T Zh Esirkepov. Exact charge conservation scheme for particle-in-cell simulation with an arbitrary form-factor. *Computer Physics Communications*, 135(2):144–153, 2001.

[42] Kane Yee. Numerical solution of initial boundary value problems involving maxwell's equations in isotropic media. *IEEE Transactions on antennas and propagation*, 14(3):302–307, 1966.

[43] *Smilei* Documentation. `http://www.maisondelasimulation.fr/smilei/index.html`. Accessed: 2020-03-07.

[44] Jay P Boris. Relativistic plasma simulation-optimization of a hybrid code. In *Proc. Fourth Conf. Num. Sim. Plasmas*, pages 3–67, 1970.

[45] *Smilei* Radiation Reaction modules. `http://www.maisondelasimulation.fr/smilei/radiation_loss.html`. Accessed: 2020-03-10.

[46] CP Ridgers, TG Blackburn, D Del Sorbo, LE Bradley, C Slade-Lowther, CD Baird, SPD Mangles, P McKenna, M Marklund, CD Murphy, et al. Signatures of quantum effects on radiation reaction in laser–electron-beam collisions. *Journal of Plasma Physics*, 83(5), 2017.

[47] F Niel, C Riconda, François Amiranoff, M Lobet, J Derouillat, F Pérez, T Vinci, and M Grech. From quantum to classical modeling of radiation reaction: a focus on the radiation spectrum. *Plasma Physics and Controlled Fusion*, 60(9):094002, 2018.

[48] *Smilei* Ionization modules. `http://www.maisondelasimulation.fr/smilei/ionization.html`. Accessed: 2020-03-08.

[49] R Nuter, L Gremillet, E Lefebvre, A Lévy, T Ceccotti, and P Martin. Field ionization model implemented in particle in cell code and applied to laser-accelerated carbon ions. *Physics of Plasmas*, 18(3):033107, 2011.

[50] F Pérez, L Gremillet, A Decoster, M Drouin, and E Lefebvre. Improved modeling of relativistic collisions and collisional ionization in particle-in-cell codes. *Physics of Plasmas*, 19(8):083104, 2012.

[51] *Smilei* Collision module. `http://www.maisondelasimulation.fr/smilei/collisions.html`. Accessed: 2020-03-08.

[52] Taiwu W Huang, CM Kim, CT Zhou, CM Ryu, K Nakajima, SC Ruan, and CH Nam. Tabletop laser-driven gamma-ray source with nanostructured double-layer target. *Plasma Physics and Controlled Fusion*, 60(11):115006, 2018.

[53] TW Huang, Chul Min Kim, CT Zhou, Myung Hoon Cho, Kazuhisa Nakajima, Chang Mo Ryu, SC Ruan, and Chang Hee Nam. Highly efficient laser-driven compton gamma-ray source. *New Journal of Physics*, 21(1):013008, 2019.

[54] Milton Abramowitz and Irene A Stegun. *Handbook of mathematical functions with formulas, graphs, and mathematical tables*, volume 55. US Government printing office, 1948.

[55] Jin-Jin Liu, Tong-Pu Yu, Yan Yin, Xing-Long Zhu, and Fu-Qiu Shao. All-optical bright γ-ray and dense positron source by laser driven plasmas-filled cone. *Optics express*, 24(14):15978–15986, 2016.

[56] Matteo Passoni and M Lontano. Theory of light-ion acceleration driven by a strong charge separation. *Physical review letters*, 101(11):115001, 2008.

[57] Matteo Passoni, Luca Bertagna, and Alessandro Zani. Target normal sheath acceleration: theory, comparison with experiments and future perspectives. *New Journal of Physics*, 12(4):045012, 2010.

[58] R Rajeev and M Krishnamurthy. Ionisation of nanoclusters at relativistic laser intensities. In *Quantum Collisions and Confinement of Atomic and Molecular Species, and Photons*, pages 180–190. Springer, 2019.

[59] Andrea Sgattoni, Luca Fedeli, Stefano Sinigardi, Alberto Marocchino, Andrea Macchi, Volker Weinberg, and Anupam Karmakar. Optimising piccante-an open source particle-in-cell code for advanced simulations on tier-0 systems. *arXiv preprint arXiv:1503.02464*, 2015.

[60] HY Wang, C Lin, ZM Sheng, B Liu, S Zhao, ZY Guo, YR Lu, XT He, JE Chen, and XQ Yan. Laser shaping of a relativistic intense, short gaussian pulse by a plasma lens. *Physical review letters*, 107(26):265002, 2011.

[61] JH Bin, WJ Ma, HY Wang, MJV Streeter, C Kreuzer, D Kiefer, M Yeung, S Cousens, PS Foster, B Dromey, et al. Ion acceleration using relativistic pulse shaping in near-critical-density plasmas. *Physical review letters*, 115(6):064801, 2015.